BETA DOSE CALCULATION IN HUMAN ARTERIES FOR VARIOUS BRACHYTHERAPY SEED TYPES

A Dissertation

by

SUNG-WOO LEE

Submitted to the Office of Graduate Studies of
Texas A&M University
in partial fulfillment of the requirements for the degree of

DOCTOR OF PHILOSOPHY

May 2003

Major Subject: Nuclear Engineering

BETA DOSE CALCULATION IN HUMAN ARTERIES FOR VARIOUS BRACHYTHERAPY SEED TYPES

A Dissertation

by

SUNG-WOO LEE

Submitted to Texas A&M University
in partial fulfillment of the requirements
for the degree of

DOCTOR OF PHILOSOPHY

Approved as to style and content by:

W. Daniel Reece (Chair of Committee)	Barry M. Berner (Member)
Leslie A. Braby (Member)	John R. Ford (Member)
Michael A. Walker (Member)	William E. Burchill (Head of Department)

May 2003

Major Subject: Nuclear Engineering

ABSTRACT

Beta Dose Calculation in Human Arteries for
Various Brachytherapy Seed Types. (May 2003)

Sung-Woo Lee, B.S., Hanyang University, Seoul, Korea;
M. S., Hanyang University, Seoul, Korea;
M. S., Texas A&M University, College Station, Texas
Chair of Advisory Committee: Dr. W. Daniel Reece

This dissertation explores beta dose profile of microspheres packed in arteries, various source geometries of ^{142}Pr that can be used for therapeutic purpose, and dose backscatter factors for selected beta sources.

A novel treatment method by injecting microspheres into feeding arteries of arteriovenous malformation (AVM) is under pre-clinical investigation. To optimize radiation dose to the clinically important area, i.e. arterial wall, preliminary dosimetric studies were needed. Monte Carlo calculations were performed for several geometries simulating arteries filled with microspheres packed by random packing methods. Arterial radii used in the simulation varied from 50 μm to 3 mm; microsphere radii varied from 10 μm to 0.7 mm. Dose varied significantly as a function of microsphere size, for constant arterial sizes. For the same sizes of arteries, significant dose increase was observed because of inter-artery exposure for large arteries (> 0.1 cm rad.) filled with large microspheres (> 0.03 cm rad.). Dose increase between small arteries (< 0.03 cm rad.) was less significant.

The dose profiles of prototype ^{142}Pr beta brachytherapy sources were calculated using MCNP 4C Monte Carlo code as well as dose point kernel (DPK) for selected cases. Dose profiles were similar to beta sources currently used indicating that ^{142}Pr can substitute for current sources for certain cases and the DPK was closely matched with MCNP result.

Backscattering of electrons is a prominent secondary effect in beta dosimetry. The backscattering is closely correlated with factors such as geometry of source and scattering material, and composition of scattering material. The backscattering factors were calculated for selected beta sources that are currently used as well as potentially useful sources for therapeutic purpose. The factors were calculated as a function of distance from the interface between water and scatterers. These factors were fit by a simple function for future incorporation into a DPK code. Backscattering effect was significant for short distance from the surface of interface between water and scattering material.

ACKNOWLEDGMENTS

I would like to thank Dr. W. Daniel Reece for his kindness and patience in guiding me to the completion of this dissertation, and throughout my pursuit of a M.S. in health physics and Ph.D. in nuclear engineering at Texas A&M University; thousands of thanks would not repay his instruction and support during these past years. I would also like to thank Drs. Barry M. Berner, Leslie A. Braby, John R. Ford and Michael A. Walker for their reviews, discussions and comments on this dissertation. The courses taught by Drs. Braby and Ford, particularly, were essential to the formulation of this dissertation and were especially enjoyable. I appreciate Dr. James R. Lindner serving as a GCR. Special thanks go to Ms. Vanessa Reece for reviewing preliminary manuscripts and assisting with my English grammar.

During the long six-and-a-half years we have been in College Station, my wife Yeon Ju has been my best supporter and friend; without her patience I could not have accomplished so much. I would like to share my happiness with my beloved son Isaiah - he has always been the joy of my life and always will be. I would also like to extend thanks to my brothers, sister, mother, father, parents-in-law and grandmother for their prayer endless support.

Thanks also go to the saints of the Korean Mission Church of Texas A&M and to Pastor Chong Kim and his family for their sincere spiritual support and prayer. I am grateful to Pastor Kim for training and teaching me what I should be as a real Christian. Most of all, it is natural that my sincere gratitude should go to Jesus Christ, who died on the cross and is resurrected for me.

TABLE OF CONTENTS

LIST OF FIGURES

Page

LIST OF TABLES

CHAPTER I

INTRODUCTION

Radiation therapy began in the early twentieth century and has now become the one of the major cancer treatments. In order to reduce radiation dose to normal tissue, internal radiation therapy (brachytherapy) is sometimes preferred over external radiation beam therapy. However, applications of beta-emitting radioisotopes for therapy purposes were not studied extensively until late 1980's. Recently, the use of beta sources in brachytherapy is expanding because it has several advantages over typical gamma sources for certain cases.

First, beta sources offer advantages over higher-energy photon emitters in terms of ease of radiation shielding within the patient and radiation protection of medical personnel. Second, the beta sources are preferred for treatment of some arterial diseases because the short electron range is suitable for thin arterial walls, and can spare healthy tissues around the target wall. For example, there is hope that restenosis can be prevented while sparing surrounding tissues by the placing of a beta emitting brachytherapy wire or stent in the coronary artery concurrent with or after the angioplasty process (Fox 2002). Ophthalmic diseases can also be treated by application of beta isotopes because of the short beta particle range. Beta brachytherapy also can be applied to radiation synovectomy. In this procedure, fluid

---

This dissertation follows the format of *Physics in Medicine and Biology.*

removed from the joint is replaced by a radionuclide held in a liquid suspension that destroys the diseased tissue through irradiation (Johnson *et al.* 1993). In another application, non-resectable hepatic tumors are being treated with beta particle emitting microspheres (Zavgorodni 1996, Campbell *et al.* 2000). Specifically, during this procedure very tiny spherical radioactive materials (microspheres: diameter ranges are in tens to hundreds of μm's) are injected into a hepatic tumor artery through a catheter system to treat the disease site. This beta brachytherapy technique can significantly decrease the radiation doses to normal tissue without decreasing radiation dose to tumor cells.

Arteriovenous malformation (AVM), especially cryptic AVM, can cause highly variable cerebral neurological defects. Transient visual loss and ischemic attacks cause concern with regard to impending stroke or rupture of the AVM, indicating that after onset of symptoms, the AVM should be treated before it causes further damage. However, it is sometimes too difficult or dangerous to treat the AVM with conventional surgical procedures because of size or location of the nidus. Fortunately, alternate methods exist to treat AVM radiosurgically after identifying nidus location by computerized tomography (CT) or magnetic resonance image (MRI) for dose planning.

Brachytherapy provides an opportunity to reduce the dose to surrounding tissue during AVM treatment. A novel AVM treatment method developed by Reece and Mawad (2001), is undergoing animal testing using injections of beta microspheres into the upper pole of the kidney to radiobiologically oblate small volumes within the kidney. Radiation dose levels for this technique are lower than the typical brachytherapy procedures for treating tumors. Conventional cylindrical wire or stent-type brachytherapy sources, currently used with angioplasty for treatment to prevent restenosis, may not be suitable for treating AVM because the artery shape (concavo-convex) and diameter of blood vessels in the brain are somewhat different from cardiovascular arteries. In the new technique, angiography is used to facilitate injection of a radioactive material in an artery just upstream of the malformation so it will close the pathway. The radioactive spheres, carried in an embolic agent, would result in permanent closure of the blood vessels. This occurs because endothelial cell growth is enhanced by relatively low doses of beta radiation that damage arterial walls radiobiologically as well as mechanically, rather than suppressed as in intra-arterial brachytherapy. Specifically, hyperplasia of endothelial cell of the vessel wall irradiated with beta emitters would close and block the blood stream. The occluded nidus will not reopen and the AVM can be successfully treated.

For this new treatment method, as outlined above, microspheres containing ^{142}Pr (microsphere diameter is approximately 50 μm) were used. Animal pre-clinical testing, performed with pig's kidney, is under way to test for clinical applicability. Little dosimetry, however, has been performed using Monte Carlo methods or dose point kernel methods.

Some dosimetry has been done for other beta emitting microspheres but no careful study of packed microspheres has been done. Existing microsphere dosimetry literature is qualitative at best. A dosimetry study investigated ^{90}Y-labeled microspheres for treating non-resectable hepatic tumors (Campbell *et al.* 2000, 2001).

They used a beta dose point kernel (DPK) method derived from Simpkin *et al.*'s point kernel data (1990) obtained by EGS4 Monte Carlo code, and calculated the dose as if from a point source, ignoring the mesh points lying within a microsphere. In real situations, there could be significant perturbation effects from self-shielding, electron backscatter, etc. Secondary radiation generation, including bremsstrahlung, can occur among the microspheres. This is because there is significant heterogeneity of microspheres observed from resected organs of test animals' kidneys (Mawad 2001) and human livers (Campbell *et al.* 2000). From Campbell's data, the injected microspheres tend to deposit in clusters rather than uniformly spaced single spheres. They report that the greatest distance between clusters was between 400 μm and 800 μm. Just from this data, there could be significant dose perturbation that was ignored in their studies. For example, the fact that ^{142}Pr itself is a high Z material and has high density, so cluster formation of microspheres may have significant perturbation effect, was not considered by Campbell *et al.* (2000, 2001) which used ^{90}Y-labeld microspheres. In this project, dose absorption in different sphere formations for a given tissue volume was studied, using a simple geometry that simulate the artery as a cylinder packed with microspheres. From a clinical point of view, the most critical dose points in the arterial wall are just a few mm across because hyperplasia is the mechanism for closing the artery.

^{142}Pr has never before been used as a brachytherapy source, making dose characterization necessary not only for the AVM treatment but also for other potential applications. Therefore, dose characterization as a function of various source geometries is one of the objectives of this dissertation. Geometries considered include point, cylindrical wire, cylindrical shell, disk, and spherical shapes. These geometries cover almost all the current types of brachytherapy sources. For cylindrical geometry, including a cylindrical shell geometry that mimics a stent, dose as a function of axial distance was compared with previous studies. Dose rate as a function of a distance was compared with that reported in several studies for similar types of radioisotopes such as ^{32}P (Prestwich *et al.* 1995) or ^{90}Sr/^{90}Y. Dose rate as a function of the diameter of a spherical source is complicated by self-absorption within the source; this effect is also explored.

In this study, both DPK and Monte Carlo methods were used to cross check results for ^{142}Pr. The Monte Carlo code, MCNP 4C (Briesmeister 2000), developed by Los Alamos National Laboratory, was used for complicated geometries, such as those involving a large number of microspheres. The DPK method was used to calculate doses for relatively simple geometries, and the results were compared with the MCNP calculations. For electron simulation, MCNP can simulate physical interactions such as collision stopping power, multiple scattering, energy straggling, bremsstrahlung production, and knock-on electrons, all of which are difficult to estimate for complex geometries using a DPK method. For the DPK method, a code fashioned after VARSKIN MOD2 (Durham 1992) was used. This code was initially developed for radiation protection purposes specifically for hot particle dosimetry in nuclear power plants. The code uses Berger's point kernel data (1971) for its calculations, and SADDE MOD2 (Reece *et al.* 1989) as incorporated in the VARSKIN package, was used for the dose calculation of beta emitting sources that have continuous beta energy spectra.

Backscatter factors, one of the most important secondary effects in beta dosimetry, were calculated as a function of depth from the interface between the water and selected source matrix materials, calcified plaques, and contrast agents. Previously, backscatter factors for beta particles have varied depending on the experimental setup and detector resolution for calculation, and were generally performed for monoenergetic electron beams, which make direct application of these factors to beta sources difficult. The calculated values in this research can be readily incorporated into DPK methods using an analytical fit approach. This model can also aid in choosing a source matrix or mixing materials for beta brachytherapy sources. Backscatter factor calculations were carried out using MCNP 4C for beta sources currently in use as brachytherapy seeds (^{32}P and ^{90}Sr/^{90}Y), as well as other sources with potentially useful sources (^{45}Ca, ^{142}Pr and ^{185}W).

Briefly, this study is a careful study of a wide range of geometries, sizes, and receptor artery sizes in brachytherapy in brain arteries. Effects of geometry, inter-shielding, bremsstrahlung, and backscatter are presented here to help pave the way for further use of microspheres for therapeutic applications.

CHAPTER II

THEORY

II-1. Restenosis

The formation of plaque, a process called atherosclerosis, gradually reduces artery lumen and results in a change in blood flow and oxygen delivery to cells. Collagen and elastin are produced and accumulate in intima, leading to focal thickening where platelets and cholesterol soon begin to adhere to the endothelium. As this process continues, lipids stacked up in the intima form yellow fatty streaks, leading to the formation of fibrous plaque. Eventually, a complex lesion develops as the core of the fibrous atherosclerotic plaque necroses, calcifies, and hemorrhages. This induces a reduction in blood flow, platelet aggregation, and ultimately the formation of thrombosis with consequent myocardial ischemia and infarction. Restenosis after an angioplasty follows a similar course; angioplasty leads to a fracture of the atherosclerotic plaque, and over weeks to months the neointima becomes less cellular and healing site begins to resemble a fibrous plaque. In about 40% of the angioplasty patients the neointimal hyperplasia is excessive and results in clinically symptomatic restenosis within three to six months (Nath *et al.* 1999a).

II-2. Arteriovenous malformation (AVM) and its treatment

AVM is a leading cause of intracranial bleeding and hemorrhagic stroke in humans, particularly young adults. Most intracranial AVMs involve only pial vessels, but some involve both pial and dural vessels. The majority of AVMs are of congenital origin, but those that involve the meningeal arteries or vertebral arteries that drain into the dural sinuses may be acquired. Those AVMs that are only a few millimeters in size cannot be identified by neuroimaging and are referred to as cryptic. Conversely, AVMs may be so large that occupy an entire cerebral hemisphere. Although AVMs are usually present from birth, they are often asymptomatic for years. However, 70% of AVMs produce symptoms in the second and third decades of life, and most are reviewed supratentorial. Recurring headaches that are always on the same side are a frequent symptom, and may mimic migraines. Deformities of the blood vessels of the brain can have a very high tendency to rupture, causing severe neurological damage, coma, or death. An angiography picture and a schematic illustration of an AVM are displayed in figures II-1 and II-2.

Several methods of treating these vascular lesions have been developed, but there is no ideal treatment available. Current treatment options include surgical resection, stereotactic radiosurgery using multiple external radiation beams focused on the target or a new method of embolization through injection of foreign material into the arterial tree in an attempt to close the abnormal blood vessels. Sometimes, combinations of these methods are used to enhance the result. None of these treatments are ideal, but there are promising results in the literature indicating that the combination of embolization of the AVM followed by stereotactic radiation therapy is effective in curing these malformations.

Figure II-1. Angiographic picture of typical AVM

Figure II-2. Illustration of an AVM nidus. The small double arrows indicate the feeding arteries which penetrate into the nidus; the open arrow indicates the terminal feeder. Arrowheads show the nidus opacification via pial anastomosis and the black arrow indicates the artery passing through. In strategic embolization of an AVM, the marginal part of the nidus is obliterated through such penetrating feeding arteries, the terminal feeder is obliterated at the entrance of the nidus and the majority of the nidus is kept opacified via the pial anastomosis; from Nagashima *et al.* 2000.

One major consideration in radiosurgery of AVMs is their size. The size of the AVM is not the deciding factor in the decision to use a LINAC or stereotactic radiosugery, but usually patients whose AVMs less than 25 cm^3 are candidates for treatment with a linear accelerator (Nagashima *et al.* 2000).

Specific endovascular techniques vary according to the anatomy of the lesion. Recent improvements in microguidewire and microcatheter technology have made it possible to treat previously unreachable and untreatable AVMs. Using a radioactive embolic material spares more healthy tissues in the brain compared to external beam therapy. The embolization helps to obliterate the AVM, as well as providing radiation therapy to the vascular bed where the embolic agent is delivered (Mawad 2001, see figure II-3). In this study, ^{142}Pr was identified as an ideal radioactive embolic agent for treating AVM and possibly hypervascular tumors i.e., those types of cancer that have a rich blood supply feeding the tumor cells.

II-3. Current beta brachytherapy sources and methods

As stated in the previous chapter, the history of beta brachytherapy is very short compared with conventional gamma brachytherapy; practical application in human arterial trials began only in the mid 1990s. Typically, beta sources are placed in the artery by percutaneous transluminal coronary angioplasty (PTCA). A small catheter is passed into the coronary using radiographic guidance, which is then used to expand a small balloon to the desired diameter. A beta source is then placed in the space thus treated. There are several seed types used in this procedure, such as solid cylinder/wire such that the source is impregnated or sealed in the wire, liquids in the

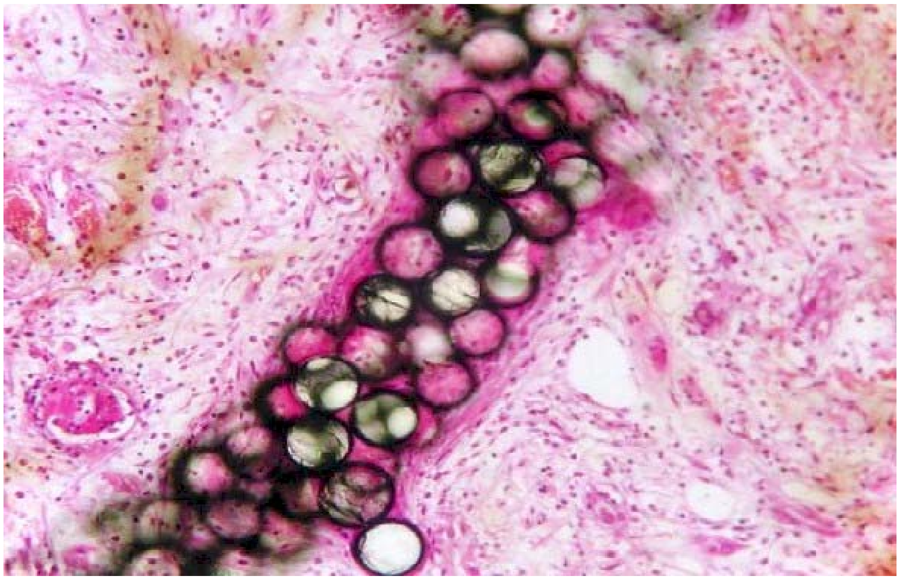

(a) Microsphere emboli and cortical atrophy in a medium sized artery

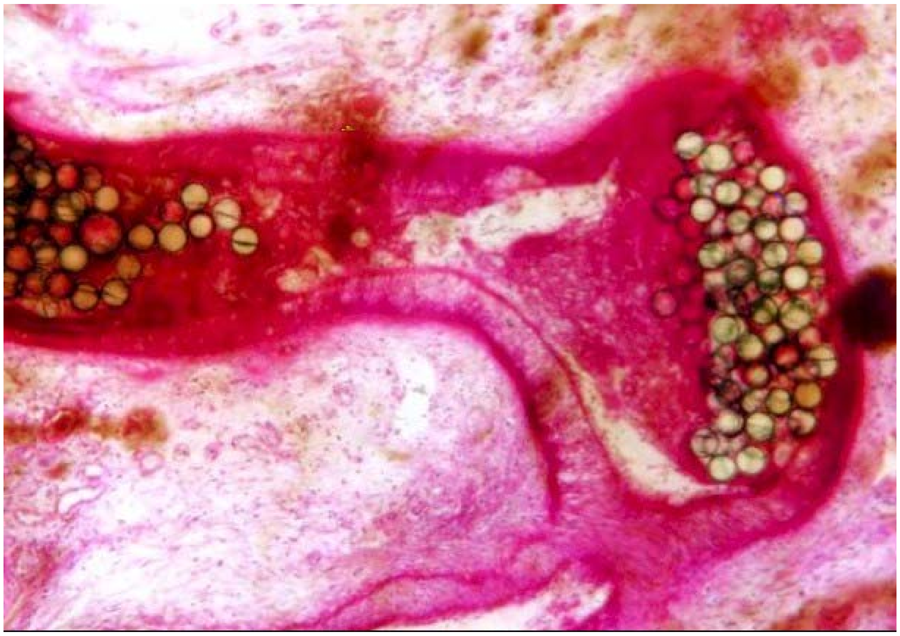

(b) Thrombosis associated with microsphere emboli in a medium sized artery

Figure II-3. Embolization animal study (kidney of pig) by Mawad angiography balloon, and stent type. For ophthalmic disease, three types of ophthalmic applicators are being used (Soares *et al.* 2001): A planar source with the radioisotope placed on the top of the planar structure, a disk type source, and a concave source.

Solid wire sources have limitations in that their size and stiffness sometimes prevents their entry into the artery (Fox 2002). In addition, without the support of a centering device, uniform irradiation to the arterial wall cannot be guaranteed. Because of this, radioisotopic liquids are often used instead, as the source is then automatically centered in the arterial lumen. However, liquid radioisotopes are not without their own problems; accidental rupture of the balloon must be avoided as these materials are bone-seeking radionuclides. Usually, the inserted isotopes are ^{32}P and ^{90}Sr and/or ^{90}Y; however, ^{188}Re has recently gained in popularity because of its short half-life and the fact that it can be obtained by generator milking from long-lived parent (^{188}W: 69 days half-life). This radioisotope is excellent for therapy as it is not bone seeking and is rapidly excreted from the patient in a breech-type accident.

Initially, stents were devised to reduce the elastic recoil of the artery in angioplasty treatment. However, its development initiated new treatment methods when it was realized that if the stents were made of radioactive material, further intervention in the artery for a separate irradiation procedure would not necessary. A noted disadvantage of this technique, however, is that the dose to the arterial wall near the stent surface may be extremely large. Additionally, because of the structural shape of the stent, dose oscillation occurs along the arterial surface. This may have a significant negative impact on the treatment due to complete destruction of tissue.

This subsequently loosens the stent and can lead to thrombus. This kind of effect contributes to restenosis despite the general fact that restenosis in the region of the stent is markedly inhibited if successful placement of stent is achieved (Nath *et al.* 1999a). In intravascular brachytherapy, beta-ray sources are typically used for their short range; however, the lesion area must be limited to between 0.1 and 0.3 cm thickness for treatment to be effective. A better characterization of dosimetry in this range will aid in the development of optimum clinical devices and methods.

Because of the difficulties in precise experimental setup, many studies have used Monte Carlo or DPK calculations as a primary method. These two methods have opposing advantages and disadvantages. Monte Carlo calculations are generally reliable for complicated source-to-target geometry and simulate particle tracks realistically, but are very time-consuming in computation. DPK calculations are much faster in computation, but the associated computer coding work can be complicated if the geometry is complex. Although the major disadvantage of the Monte Carlo calculations (i.e. time-consuming computations) has recently become less of an obstacle as fast computers are now easy to obtain without excessive financial sacrifice, in most clinical situations medical staffs still prefer DPK method because of the speed of calculation allows for exploring different treatment geometries, for example. As Monte Carlo and DPK calculation methods are the main tools used to predict availability of beta ray sources, they were used to simulate the dose rates of point and sphere sources comparison with other beta-ray sources in this study.

II-4. Monte Carlo codes

There are several Monte Carlo codes used in medical physics to establish dose protocol for external beams and isotropic brachytherapy sources. The most widely used codes are EGS4 and MCNP. Both codes have had their transport physics algorithms updated over the years by successive researchers. The most recent version of the EGS4 code is EGSnrc (Karakow *et al.* 2000) that was released by NRCC (National Research Council of Canada). The latest version of MCNP 4C, was released in 2000. The electron physics in MCNP is similar to that of the ITS (Integrated Tiger Series).

Electron transport in MCNP is based on the ETRAN series, originally developed at the National Bureau of Standards (now the National Institute of Standards and Technology) by Berger and Seltzer (1968). ETRAN has been used in the calculation of therapeutic beam dosimetries, usually for electrons (Andreo 1991). The ETRAN model provides sophisticated electron transport simulation, but does not treat any geometry other than infinite media or plane parallel slabs of different materials. In order to overcome this disadvantage, the ITS code consisting of TIGER, CYLTRAN and ACCEPT as developed by Halbleib (1988) was used. These codes allow for transportation of electrons and photons down to 1 keV in plane-parallel slabs, cylindrical geometry or any combination of these geometries.

II-4-1. Electron transport in MCNP

Charged particle Monte Carlo codes, especially electron Monte Carlo codes, rely on a variety of analytic and semi-analytic multiple scattering theories. Formulae based on these theories use the fundamental cross sections and the statistical nature of the transport process to predict probability distributions for significant quantities, such as energy loss and angular deflection. Major theories used in MCNP are Bethe-Bloch theory for mean energy loss, the Goudsmit-Saunderson theory for angular deflections, the Landau theory of energy fluctuations, and the Blunck-Leisegang enhancement of the Landau theory. These theories rely on a variety of approximations that restrict their applicability, meaning that individually they cannot solve the entire transport problem (Hughes 1997).

One of the main differences between EGS4 (EGSnrc) and MCNP is the methods by which they address secondary electrons (Jeraj *et al.* 1999); MCNP uses a Class I algorithm while EGS4 series uses a Class II algorithm. Class I algorithms group all the interactions and use a predetermined set of path lengths. Random sampling is performed at the end of the each step so that the energy is statistically conserved. On the other hand, in Class II algorithms the energy of the primary electron is affected by the secondary electrons. However, the Class II algorithm used in MCNP 4B for radiative loss has been modified to overcome the underestimation common to the Landau theory. For more specifics about the physics used in the EGS4 series of Monte Carlo codes the reader is referred elsewhere (Nelson *et al.* 1985).

II-4-2. Electron steps in MCNP

In MCNP, the condensed random walk for an electron is considered in terms of a sequence of path lengths and monotonically decreasing energy. The energy and path lengths are expressed as

$$E_{n-1} - E_n = -\int_{s_{n-1}}^{s_s} \frac{dE}{ds} ds \,, \tag{2-1}$$

where E_{n-1} and E_n represent each energy grid, s_n and s_{n-1} represent path lengths, and $-dE/ds$ is the total stopping power in energy per unit length (Briesmeister 2000 and Hughs 1997).

The energy loss per unit path length due to collisions that is less than a fraction, η, of the electron kinetic energy E is from the Berger's formulation:

$$\left(\frac{dE}{ds}\right)_{\eta} = \frac{\rho N_A Z_{av} C}{M_A}\left[\ln\left(\frac{\tau^2(\tau+2)}{2(I/m_e c^2)^2}\right) + F^{\pm}(\tau,\eta) - \delta\right], \tag{2-2}$$

where, I is the mean excitation potential, N_A is Avogadro's constant, ρ is the density, M_A is molar mass and Z_{av} is the average atomic number of the material electrons that have negative charge and δ is the density effect correction factor, and specifically

$$F^{\pm}(\tau,\eta) = 1 - \beta^2 + \frac{\tau^2}{(\tau+1)^2}\frac{\eta^2}{2} + \frac{2\tau+1}{(\tau+1)^2}\ln(1-\eta) + \ln[4\eta(1-\eta)] + \frac{1}{1-\eta}, \tag{2-3}$$

and coefficient C is expressed as

$$C = \frac{2\pi m_e c^2 r_e^2}{\beta^2}, \tag{2-4}$$

where r_e is the classic electron radius. In eq. (2-3), τ is electron kinetic energy and β equals the electron speed as a fraction of the speed of light c. The relation between τ and β is:

$$\beta = \sqrt{1 - \left(\frac{1}{\tau+1}\right)^2} \,. \tag{2-5}$$

and specifically,

$$Z_{av} = \frac{\sum_i \omega_i Z_i / A_i}{\sum_i \omega_i / A_i}, \tag{2-6}$$

where Z_i are the atomic numbers, ω_i are the weight fractions, and A_i are the atomic weights of the different elements in the material. From eq. (2-1), ETRAN based codes customarily choose the sequence of path lengths s_n such that, for constant k,

$$E_n = kE_{n-1}. \tag{2-7}$$

In this equation, k equals to $2^{-1/8}$, which accounts for 8.3% of energy loss per step. The representation of electron trajectory as the result of many small steps will be more accurate if the angular deflections are small. MCNP can divide the electron steps into smaller substeps. A major step of path length s is divided into m substeps (s/m). The m depends on average atomic number Z. Appropriate values for m have been determined empirically, and range from $m = 2$ for $Z < 6$ to $m = 15$ for $Z > 91$. MCNP allows m to be increased for a given material for use in specific cases, such as a very small region of detectors used to collect electron dose.

II-4-3. Electron energy straggling

Electron energy loss is stochastic process because the microscopic interactions by any specific particle take place randomly. Therefore, even for a monoenergetic beam, a spread of energies occurs as the particles pass through a thick absorbing medium. This phenomenon is called energy straggling and varies with the absorption depth along the particle path (Knoll 1999). As distance increases, the distribution widens. Then, near the end of the electron range, the distribution narrows again due to the reduction of mean particle energy. Therefore, energy loss cannot be expressed as simple average of $\overline{\Delta}$. It is the probability distribution *f(s, Δ)d*Δ that Landau expressed as

$$f(s,\Delta)d\Delta = \phi(\lambda)d\lambda, \tag{2-8}$$

where Δ is energy loss, *s* is the step length and $\phi(\lambda)$ is a universal function of single scaled variable.

II-4-4. Angular deflection by Gouldsmit-Saunderson theory

The ETRAN series of codes, including MCNP, uses the Gouldsmit-Saunderson theory for abnormally large angle deflections. However, this distribution theory can be applied to much smaller path lengths and all scattering angles. The angular deflection of the electron is sampled according to the distribution

$$F(s,\mu) = \sum_{j=0}^{\infty}\left(j+\frac{1}{2}\right)\exp(-sG_j)P_j(\mu), \tag{2-9}$$

where *s* is a substep in g/cm^2, μ $(= \cos\theta)$ is angular deflection at each substep, $P_j(\mu)$ is jth Legendre polynomial, and G_j is calculated from

$$G_j = 2\pi N\int_{-1}^{1}\frac{d\sigma}{d\Omega}[1-P_j(\mu)]d\mu, \tag{2-10}$$

where *N* is number of atoms. The loss of electron energy along its track can be taken into account in the continuous slowing down approximation by substituting

$$G_j \rightarrow \int_{T_1}^{T_0} G_j(T)\frac{dT}{S(T)/\rho}, \tag{2-11}$$

where T_0 is the initial electron energy, T_1 is the energy reached after a path length s, and $S(T)/\rho$ is mass stopping power in MeV·cm^2/g.

II-4-5. Bremsstrahlung in MCNP

Sampling of bremsstrahlung photons is addressed at each electron substep. Tables determine the probability of bremsstrahlung production and new photon energy is sampled from the bremsstrahlung energy distribution tables. Deflection of the photons can also be sampled from tabular data. The direction of the electron is not affected by the generation of a photon, because it is controlled by multiple scattering theory.

II-4-6. Knock-on electron treatment in MCNP

Treatment of knock-on electron follows the MØller cross section,

$$\frac{d\sigma}{d\varepsilon}=\frac{C}{E}\left\{\frac{1}{\varepsilon^2}+\frac{1}{(1-\varepsilon)^2}+\left(\frac{\tau}{\tau+1}\right)^2-\frac{2\tau+1}{(\tau+1)^2}\frac{1}{\varepsilon(1-\varepsilon)}\right\}, \tag{2-12}$$

where ε represents energy transfers as fractions of the electron kinetic energy E and τ is the electron kinetic energy in electron rest mass units. Once energy has been sampled, the angle between the primary direction and the direction of the newly generated secondary particle is determined by consideration of the momentum. The deflection is used for the subsequent transport of the secondary electron. Sampling of the secondary particles does not alter either the energy or the direction of the primary electron.

II-4-7. Different electron energy indexing algorithm in MCNP

The use of different electron energy indexing algorithms in MCNP 4C significantly affect the calculated dose (Shaart *et al*. 2002, Jeraj *et al.* 1999, Love *et al.* 1998). The default option uses MCNP-style or MCNP-inherent style algorithms; this feature can be enabled by using a DBCN card in the MCNP input. This approach is called the bin-centered algorithm. ITS-style algorithms can also be used, and follow the methods of ITS 3.0 (the latest version of ITS code), called the nearest boundary algorithm. The MCNP-inherent algorithm uses cross section data from the energy group in which the electron begins, while ITS-style algorithms use the data closest to the boundary of the electron at the beginning of the step. MCNP-(inherent) style algorithms result in higher dose collection than ITS-style, because MCNP-inherent style causes electrons to correspond to scattering power data at higher energies (Jeraj *et al.* 1999). This result is verified later in this study during backscattering factor calculation. According to Shaart *et al.* (2002), however, ITS 3.0 algorithms are recommended if one desires higher accuracy; the difference between these two indexing methods is displayed in figure II-4.

II-5. Dose Point Kernel (DPK) method

In order to ascertain the validity of DPK method, the beta and gamma dose from ^{142}Pr were calculated using modified VARSKIN (representative DPK code for beta dose calculation). The VARSKIN code is widely used in health physics to calculate skin dose from hot particles attached to the skin or clothes of workers in nuclear power plants. Since this code considers the source to be located between the

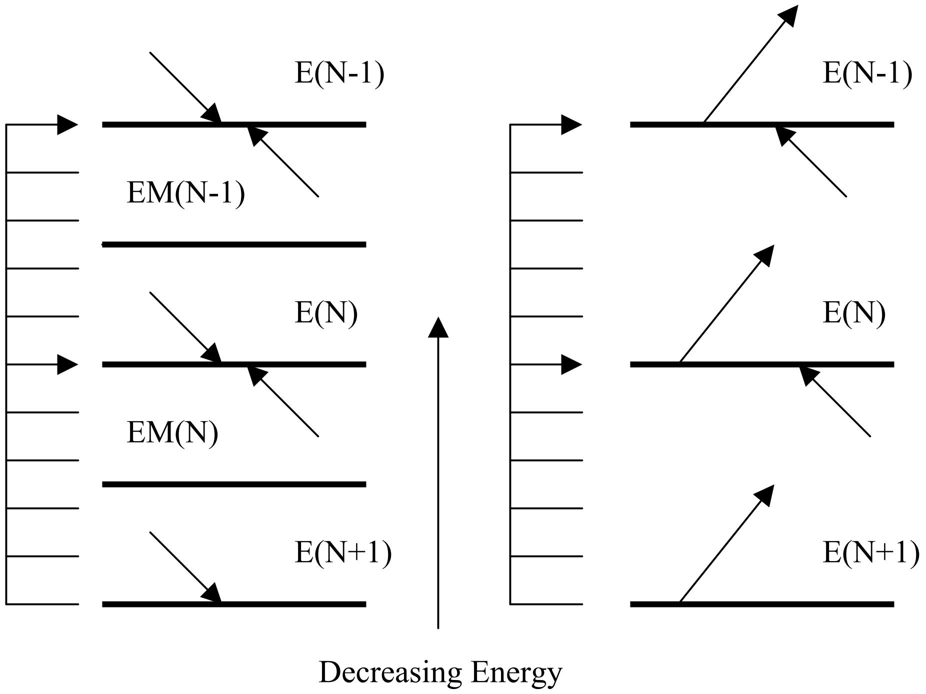

Nearest-group-boundary treatment
(ITS emulation)
Collects nearest energy bin data

Bin-centered treatment
(MCNP default)
Collects the energy data that energy started

Figure II-4. Energy group selection in MCNP 4C code water-equivalent skin and air, modification of the code was needed before it could be used to calculate point and sphere sources in water. The DPK code was originally based on VARSKIN MOD2 (Durham 1992) and modified for geometry input. The VARSKIN code is based on Berger's point kernel data (Berger 1971). The kernel is mathematically expressed as

$$B(r) = \frac{kE_{\beta} Y F_{\beta}\left(\frac{r_1}{X_{90}}\right)}{4\pi\rho r^2 X_{90}}, \tag{2-13}$$

where,

r = a variable representing the distance between a source point and a dose point,

k = a unit point conversion factor,

E_{β} = the average beta energy for the radioisotope,

Y = the beta yield per disintegration,

$F_{\beta}(r_1/X_{90})$ = the scaled absorbed dose distribution as a function of the modified path length and the X_{90} (distance which 90 % of the beta energy deposited from a point source) distance,

r_1 = the modified path length between the source point and dose point, and

ρ = the density of the irradiated medium.

Beta energy used in the MCNP calculation was in the form of 100 discrete energies, obtained from Seltzer (2001), that were generated by LOGft program. The DPK calculation used 150 discrete energies generated by SADDE MOD2. The SADDE code (Reece *at al.* 1989) was developed to provide scaled absorbed dose distribution data for any beta-emitting isotope for use in VARSKIN. Specifically, average beta energy can be obtained from the following expression of beta spectrum integration,

$$E_{\beta} = \frac{\int_0^{E_{\max}} ES(E)dE}{\int_0^{E_{\max}} S(E)dE}. \tag{2-14}$$

This DPK method uses Newton-Cotes eight-panel quadrature routines to interpolate a point between dose point r_I and r_{I+1}.

In this study, dose delivered by the point source and sphere source was calculated using the DPK method. For the sphere source, the dose integral is written as

$$\dot{D}(d) = \int_0^{2\pi}\int_0^{R}\int_0^{Z} B(r,d,\theta,z) r dr dz d\theta, \tag{2-15}$$

where S_v is the volumetric source strength. The results of the modified code were compared to MCNP results as a function of source diameter. In practice, a density-scaling method was used for beta ray tracking in the source area. For example, the sphere source used in this study was 3 g/cm^3, and the radiation tracking distance can be obtained by

$$d = \sum_i \varsigma_i d_i, \tag{2-16}$$

where ς_i and d_i represent scaling factors and path lengths for each medium, respectively.

Gamma dose rates were calculated together using the specific gamma ray constant or exposure constant Γ, and defined as

$$\dot{X} = \Gamma \frac{C}{r^2}, \tag{2-17}$$

which numerically expresses exposure rate per unit activity at unit distance, and is generally presented as $R \cdot m^2 / Ci \cdot hr$, where C represents the activity of a source and r represents the distance from that source. The exposure rate was due solely to gamma rays, and excludes the affect of X-rays generated through internal conversion or bremsstrahlung X-rays. If these secondary X-rays were included, the exposure rate would increase by up to 2%, which is not significant with regard to total dose rate. Consequently, the dose rate from gamma rays traveling in an attenuating medium with attenuation coefficient μ, at a distance r from source strength S_v is

$$D_\gamma(r) = \Gamma \frac{S_v}{r^2} e^{-ur}. \tag{2-18}$$

If the gamma ray passes through several media with different densities, then the dose rate is calculated using the same equation as above, but the attenuation term is summed and expressed as

$$D_\gamma(r) = \Gamma \frac{S_v}{r_i^2} \sum_{i=1} e^{-u_i r_i}, \tag{2-19}$$

where r_i is the distance traveled by gamma ray in medium i and μ_i is the attenuation coefficient of each medium i.

II-6. ^{142}Pr source

^{142}Pr emissions are about 99.98% beta rays (E_{max} = 2.16 MeV), 3.7% gamma rays (1.575 MeV), and very small portion X-rays and electron capture energies per disintegration. Since the half-life of this radioisotope is only about 19.12 hours, careful time management is essential for clinical application. The gamma energy used in this calculation is listed in table II-1, and average gamma and X-ray energies were used. Calculated energy including only significant contribution to total gamma dose, was 58.13 keV. All data were obtained from http://t2.lanl.gov; only the gamma-ray portion under consideration is presented in the table for this calculation. The beta spectrum input was obtained from Seltzer (2001), NIST, and the data was normalized and incorporated into MCNP input. The shape of the beta spectrum is shown in figure II-5.

The calculation of beta spectrum is expressed briefly in eq. (2-14), and SADDE MOD 2 code was used for spectrum generation for DPK input as well as MCNP input. The SADDE MOD2 used subroutine BETA, originally developed by Kansas University (Reece *et al.* 1989). The algorithm used in the calculation is as follows.

First, the value of Fermi function $f(Z,W_0)$, must be determined based on the maximum energy of beta particle, E_{max}, and the atomic number, Z, of the decay product. This value of $f(Z,W_0)$ is then multiplied by the half-life of the daughter to obtain the value ft. The ft which depends only on Z, t and E_{max}, can be used to determine the degree of forbiddenness. The ft values vary to 10 and 10^{18}, therefore the $log_{10}(ft)$ is used to predict the degree of forbiddenness. If an isotope has several decay modes, the half-life of the particular decay can be calculated by using the overall half-life divided by the probability of the particular path. The degree of forbiddenness is obtained by angular momentum, the parity change, and the $log(ft)$ value.

Using these input data, BETA calculates a normalized beta spectrum, *n(E)*, which is expressed as follows:

$$\int_0^{E_{\max}} n(E)dE = 1. \tag{2-20}$$

The calculated spectrum is divided into 150 energy bins and then interpolated into 1500 values using a spline interpolation. The average energy of composite spectrum is calculated using the following:

$$E_{avg} = \int_0^{E_{\max}} COMP(E)EdE, \tag{2-21}$$

where, *COMP* is an array storage. With this calculation method, subroutine SADD calculates average energy and absorbed dose function, $\phi_\beta(x)$. The generated spectrum data is then incorporated into MCNP input and compared with the DPK calculation. The results are given in Chapter III.

Table II-1. Gamma energy for ^{142}Pr used in this calculation

Gamma Yield	MeV	Gamma Yield × MeV
2.21E-05	6.420E-01	0.000381528
6.24E-05	3.472E-02	5.82591E-05
3.41E-05	3.428E-02	3.14336E-05
2.36E-05	3.930E-02	2.49404E-05
1.76E-05	4.840E-03	2.29064E-06
2.28E-04	5.088E-01	0.003119475
3.68E-02	1.576	5.79968E-02
0.0371878 (Total)		0.0581 (Total)

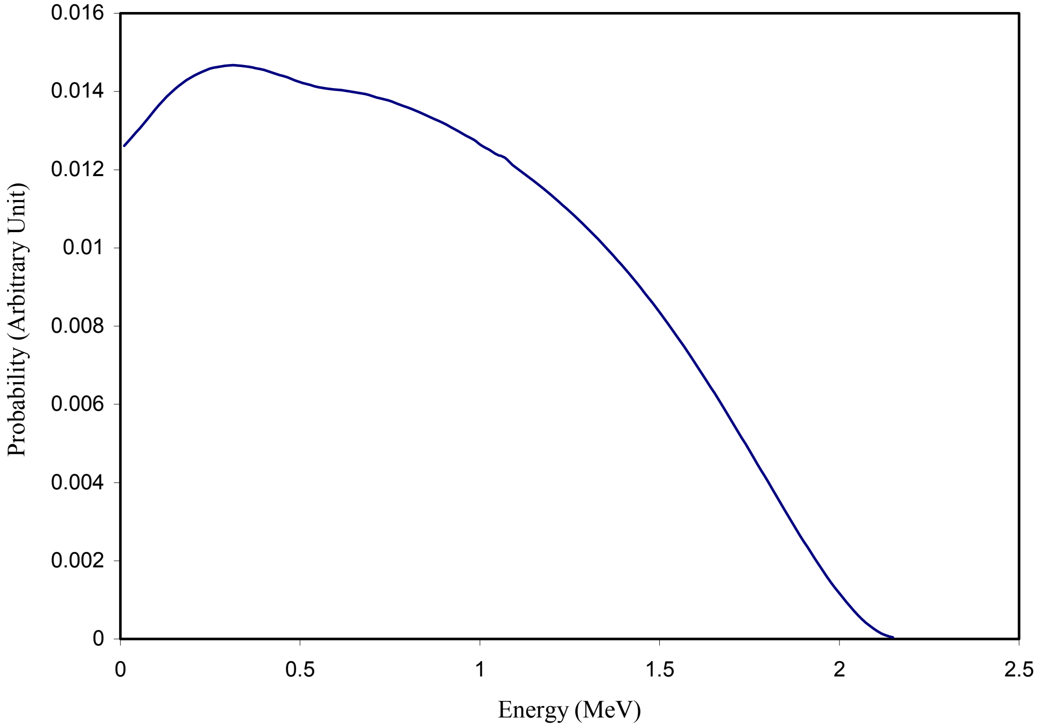

Figure II-5. Normalized beta spectrum probability of ^{142}Pr

CHAPTER III

MICROSPHERES IN BRAIN ARTERIES

III-1. Microspheres in AVM feeding arteries

Deposition patterns of the microspheres used in this study for AVM treatment in human brain are not well known because injection of microspheres has only been performed in animal tests using pig's kidneys (see figure II-3) that are hopefully physiologically similar to arterial branch of human brain. The deposition of the microspheres depends on the diameter of artery, blood flow rate, branching of arterial paths and their angles and any addition of embolic agent. In addition, current CT resolution, typically as small as 1 mm (Yeung *et al.* 1996), is not great enough to describe the curvature between the microsphere and tissue. However, this study explores a wide variety of sphere densities and artery sizes. Consequently, prediction through the calculation of deposited microspheres in the artery maybe more practical than direct experimentation. In this study, the brain artery was modeled as a simple cylinder rather than a bifurcated arterial branches, and the dose rate was observed in various source-to-detector geometries in the assumption that the cylinder is packed with microspheres in a variety of packing densities.

III-2. Random close packing of spheres in a cylinder

The dose rate to arterial walls by microspheres is strongly affected by the packing ratio of the microspheres. Naturally, compact packing of microspheres in a given volume would give the highest dose rate to the wall. At present, Kepler's theory that hexagonal close packing is known to be the densest packing method according to the published articles (Nolan *et al.* 1992, Torquato *et al.* 2000). By this theory, packing ratio reached around 74% and this would be the highest packing ratio that can ever be achieved.

However, it is impossible to achieve hexagonal close packing in this study. Particularly, hexagonal close packing would not happen in microsphere packing in arteries because packing of microspheres would take place randomly. Therefore, the random packing model was used in this study, and this method has been used for various applications. The applications include understanding the structure of living cells, liquids, granular media, glasses, and amorphous solids, etc. (Torquato *et al.* 2000). To predict actual packing, a Monte Carlo method which realistically simulates experiment has been used. Results of this calculation rarely exceed a 64% packing ratio in any container (Nolan *et al.* 1992, Jodrey *et al.* 1985, Torquato *et al.* 2000).

In this study, S3D® (Siams Ltd. website manual) was used to obtain input in the format to be used in MCNP calculations. This program can assign the dimensions and shapes to be packed with spheres, including box, helix and cylinder options. S3D® users can choose a single diameter of spheres to pack or choose spheres with various size distributions. Since the size of the microspheres used in this study can vary up to ± 7%, this factor was used to generate random packing (i.e., different sizes of spheres were simulated).

The diameter of the cylinders mimicking an artery varied from 0.01 cm to 0.6 cm, and the diameter of the microspheres varied from 10 μm to 0.14 cm. The S3D®

also has graphic function to render the result of packing; as shown in figure III-1. The simulation used in this algorithm is such that the spheres were generated by size distribution and dropped into the cylinder either from the center of the cylinder or from randomly chosen positions in side of the cylinder wall; in this study, the randomly chosen position option was selected. The physical impact of the dropped sphere was not considered. As the sphere touched other spheres, the bottom of the cylinder or the cylinder wall, it stuck to those obstacles and slid over the surface in the direction of the potential energy. When the sphere arrived at a point of 3 intersections of surfaces (three spheres, 2 spheres and 1 plane, etc.) or a surface perpendicular to the direction of its fall, the falling movement of sphere was stopped. The S3D®, packing algorithms are as follows.

First, determine radius of the sphere and initial position of drop. In this step, users can choose the position of drop around the desired dimension those can either center or each side of the corner of dimension. Second, vertical fall is initiated until the sphere contacts something. Third, the current set of restrictions is analyzed to find whether the position in the packing space is stable. If not, choose the new direction of movement of the sphere center. Relocation in any direction must satisfy the restrictions and form the minimal allowable angle (less than π/2) with the direction of the free fall of sphere. If there is no direction to move and all angles less than π/2, stop and choose the next sphere for packing. Fourth, determine the next movement direction of the sphere center. It can either be a direct line or an arc segment. Fifth, calculate current location of the sphere with respect to potential intersections with other spheres or the cylinder wall. All points inside another sphere or beyond the wall

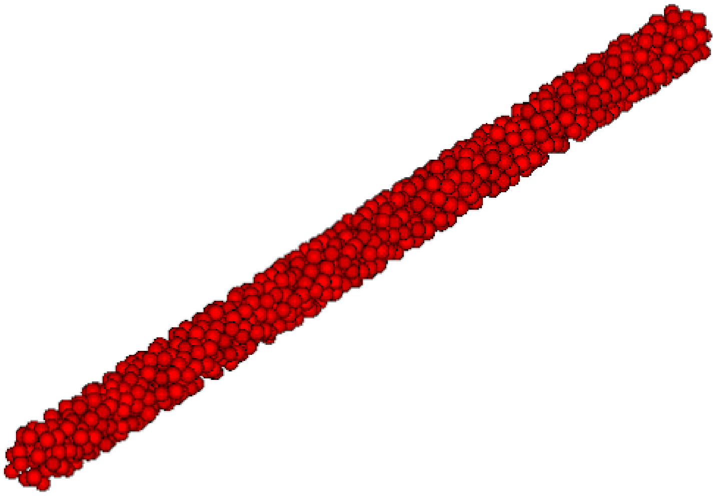

(a) 995 microspheres (dia.: 0.01 cm) packed in a 0.04 cm diameter artery
(note: not to scale)

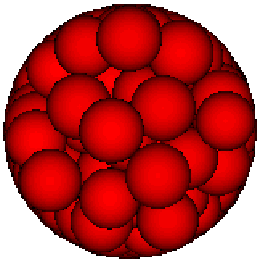

(b) Cross sectional view of the packing

Figure III-1. Random packing of microspheres in a cylinder (Graphics generated using S3D® computer program) are rejected for the center of the packed sphere. If finished, return to second step for further packing of microspheres.

From the S3D® program, center points of the spheres were obtained and the packing ratio was calculated using EXCEL®. The packing ratio was assessed by comparing the sum of the volume of microspheres to the cylinder volume; it was found to range between 48% and 52%. In the real situation, the most densely packed microspheres presumably would not exceed this ratio as the density is lessened by blood flow and vessel movement.

III-3. Geometry used for multiple spheres

The potential arrangements of microspheres within the arterial walls are various and very hard to characterize. As mentioned in previous chapter, the simple geometry was used in this preliminary study, and this approach reasonable because the primary purpose of radioactive microsphere injection is embolization. The highest dose that can be achieved with the smallest activity is by random close packing of microspheres in the artery. Potential reduction of unnecessary radiation to the arterial wall by attaching microspheres to the arterial wall using acryl cyanate glue is still under investigation.

In this study, radii of microspheres from 0.001 cm to 0.07 cm were simulated to account for natural variation, and the arterial radii chosen for the calculation were from 0.005 cm to 0.3 cm. A 0.01 mm radius is the smallest size that the manufacturer can achieve within their quality control standard, and a microsphere with 53 μm diameter (26.5 μm radius) was actually injected into the kidney of pigs used in the

Reece and Mawad study (2001). The 53 μm diameter microspheres closed the arteries well while saving healthy cells in the kidney (Mawad 2001).

To study the effects of various arterial and microsphere sizes, concentric cylindrical ring-type detectors were placed. The distance from the arterial wall was varied from 0.01 cm to 0.4 cm (see figure III-2. (a)). This detector geometry was compared with plane-type geometry (see figure III-2. (b)). This chapter focuses on brain arteries where the critical target is no more than 2.5 mm from the inner wall of the artery, while typical arterial diameter is 3 mm in coronary arteries. As Fox (2001) mentioned, the longest distance of interest point from the source would be only about 4 mm. The height of the cylindrical ring varied between 0.2 mm and 0.04 mm depending on the height of arterial cylinder. The thickness of cylindrical shell was 2 μm up to 0.1 cm distance from the surface of the artery, and 20 μm thick beyond that distance. The number of spheres packed in the cylinder was varied between 120 and 995 spheres. The maximum number of spheres was limited to 995 because the cell description of MCNP only allows less than 1000 words per cell. In the case of calculating the dose rate between the two cylinders or if there was a need to increase the height of cylinder, the cell transformation function embedded in the MCNP cell card was used to duplicate the sphere-packed cylinder. Inter-shielding or dose enhancement effects between arteries filled with microspheres were also considered in this study. The geometry used in the calculation was two identical arteries parallel each other with the detector located between them. For this calculation, a thin plane detector was chosen such that wide side of the detector faced towards the artery. The

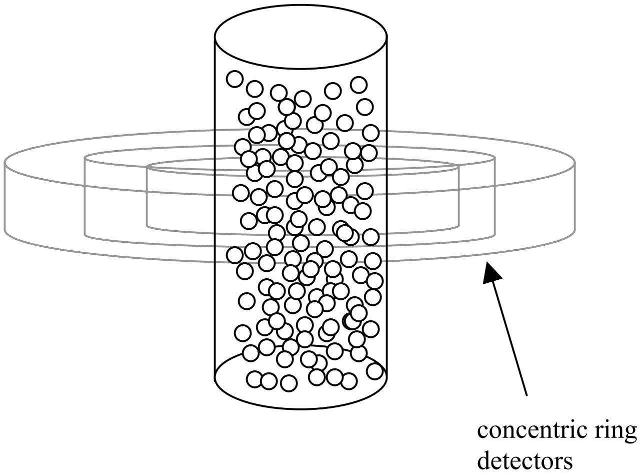

(a) Concentric ring detectors

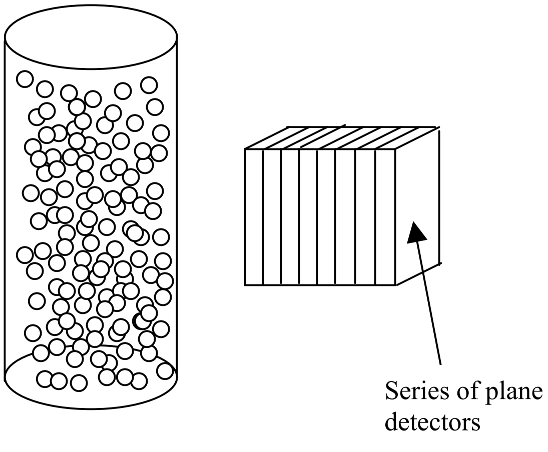

(b) Series of thin plane detectors that broad side towards the arterial wall

Figure III-2. Source to detector geometry used for single artery thickness of the detector was identical to that of cylindrical detector that was used for calculation of single artery. The detector thickness was chosen to be 0.02 mm for all distances. The width of each detector was 0.4 mm, and height of the detector varied from 0.4 mm up to 4 mm. A schematic of the stacked detector volumes is shown in figure III-3.

III-4. Results

III-4-1. Single artery filled with microspheres

Monte Carlo calculations were performed for combinations of microspheres and arteries with various radii. The smallest microsphere diameter was chosen to be 20 µm. The largest diameter considered in this study was 700 µm. For arteries, 100 µm to 6 mm diameters were chosen. Diameter ratios (artery to microsphere) were usually between factor of around 2 (e.g. 3 mm diameter artery to 1.4 mm diameter microsphere) to 10 (6 mm diameter artery to 0.6 mm diameter microsphere). Higher artery to microsphere ratios (i.e. smaller microspheres in a large blood vessel) were not considered because they would show almost the same dose characteristics as a solid cylindrical source. In order to make the comparison among various source geometries comparable, the same detector size was used. For this, a thin plane type detector was used rather than a concentric ring type detector. However, in the case of a 0.6 mm artery and 53 µm microsphere (all diameters), the height of the cylinder was only about 0.55 mm because of the limitation of number of the MCNP cell description. Therefore, stacking up of several cylinders was needed to compare with other arterial

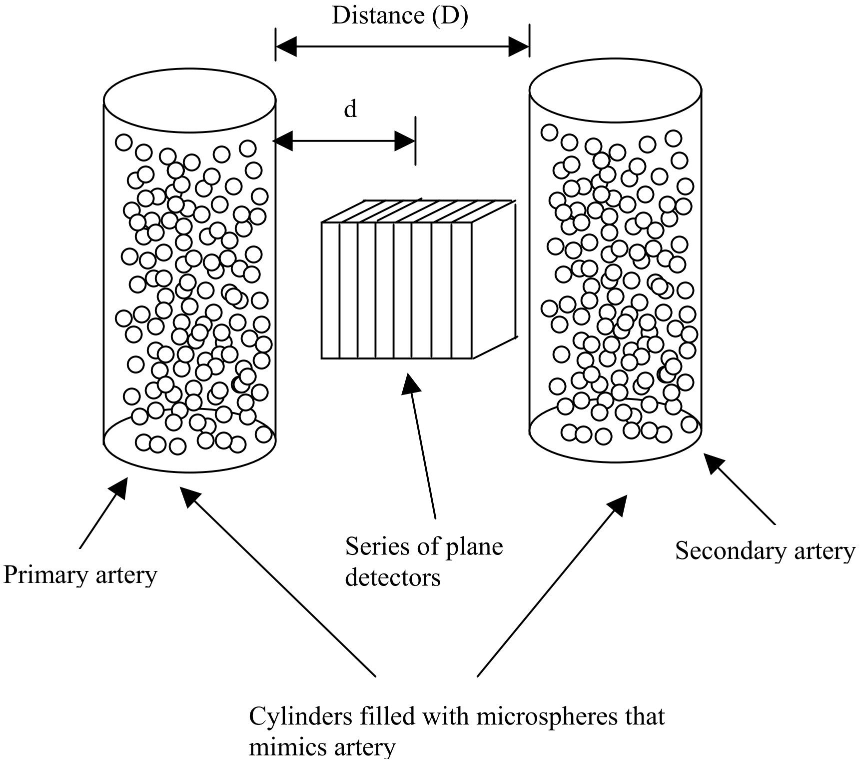

(a) Packing in the figure does not express random close packing but is for visualization only (D: distance between arterial walls, d: distance between primary arterial wall and detector)

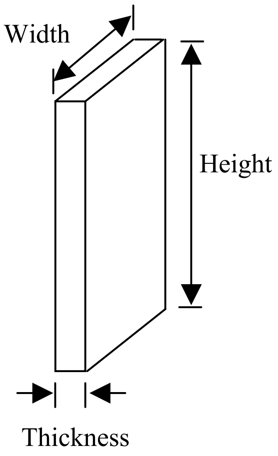

(b) Nomenclature of detector

Figure III-3. Source to detector geometry used for perturbation effect between the two arteries sizes. Furthermore, usual detector volume of 0.4 mm wide × 0.8 mm high × 0.02 mm thick could not be used. Instead, a 0.4 mm wide × 0.4 mm high × 0.02 mm thick detector was used. As shown in figure III-4, the smaller the microsphere and arterial size, the higher the dose rate observed at the closest detector location. When the smallest artery and the smallest microsphere were considered, the dose rate was more than 1000 times higher than those of 3 mm and 6 mm artery sizes (all in diameters) filled with any size of microspheres for a given unit activity.

The total dose to the arterial wall, D_{tot}, during the entire life of the microsphere, making the assumption that the microspheres were static and would stay in the same arrangement could be calculated as follows:

$$D_{tot} = \int_0^{\infty} \dot{D}(t)dt\,, \qquad (3\text{-}1)$$

where

$$\dot{D} = D_0 e^{-\lambda t}\,, \qquad (3\text{-}2)$$

where D_0 is the initial dose rate and λ and t are decay constant and elapsed time, respectively. For AVM treatment, lesser dose is needed, therefore, a weaker source is used in order to induce hyperplasia of arterial wall rather than prevent it. To achieve this goal, required cumulative doses are known to be less than 10 to 15 Gy. To predict dose rate for any given situation such as clusters or embolic matrix, the maximum final target dose can be set to 15 Gy. Then using the results obtained in this study, the initial source activity to achieve optimum treatment result can be calculated. Using this approach, for example, a 100 μm diameter artery filled with 20 μm diameter

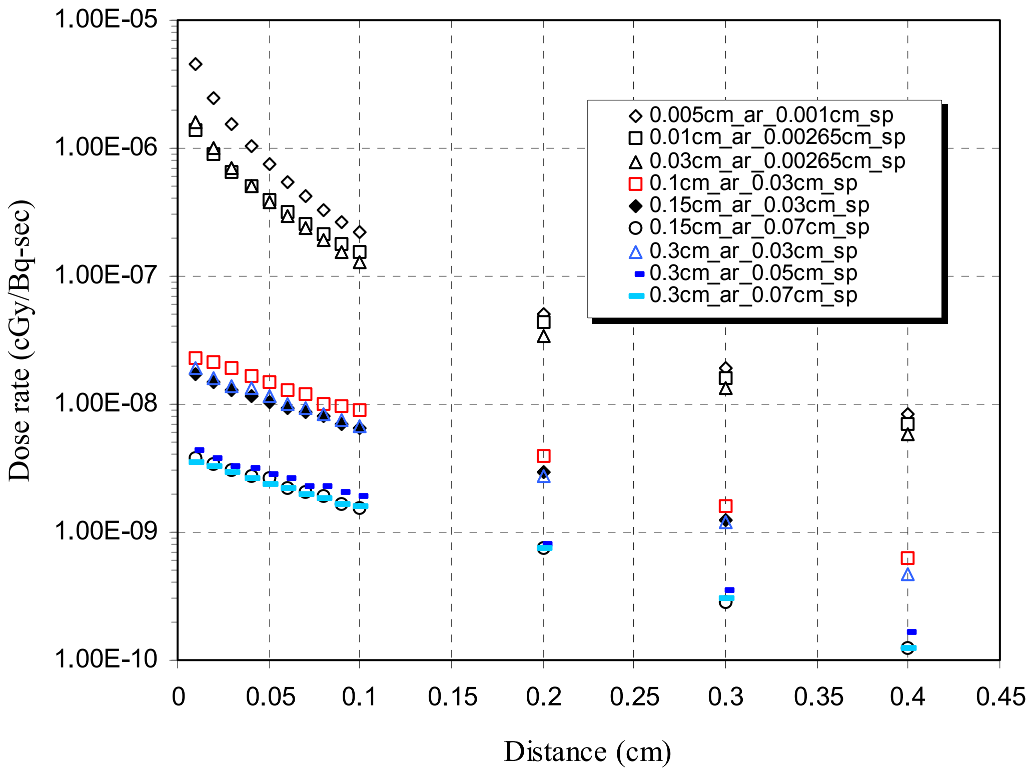

Figure III-4. Dose rate to the arterial wall as a function of microsphere and arterial size (Note: As shown in the caption box, 0.005cm_ar_0.001cm_sp represents 0.005 cm radius artery filled with 0.001 cm radius microspheres. Following figures are listed as the same manner) microsphere needs only about 3.3 Bq/microsphere to deliver 15 Gy at a depth of 0.1 mm in the arterial wall. To obtain the same accumulated dose, in a case at the other extreme such as 3 mm diameter artery filled with 1.4 mm diameter microspheres, the activity must be increased to about 33000 Bq/microsphere or about 10000 times greater than the former case. Furthermore, there could be significant dose variations observed for the latter case because large vacant areas can exist between the packed spheres. While figure III-4 just illustrates the dose rate to the wall as a function of microsphere and arterial sizes, figure III-5 describes not only by variation of microsphere and arterial sizes, but also as a function of unit volume of microspheres. This figure is useful in terms of what volume of microspheres should be injected for delivering desired dose rate to arterial wall. For example, a 2 mm (diameter) artery filled with 0.6 mm (diameter) microsphere (0.1cm_ar_0.03cm_sp) just delivers less than 60% of the dose of 100 μm diameter artery filled with 20 μm diameter microsphere (0.005cm_ar_0.001cm_sp) at 0.2 cm from artery wall.

III-4-2. Two arteries filled with microspheres

In most practical cases, the feeding arteries to the AVM exist alongside other feeding arteries rather than in isolation. It is unclear how nearby arteries affect each other in clinical situations. Therefore, it is necessary to take into account enhancement effect of other nearby arteries filled with microspheres. The sizes of the feeding arteries were assumed not to differ significantly from adjacent to the primary artery. This section, therefore, concentrates on the effect of the same size of arteries affected by a nearby artery filled with the same size of microspheres. The geometry of the

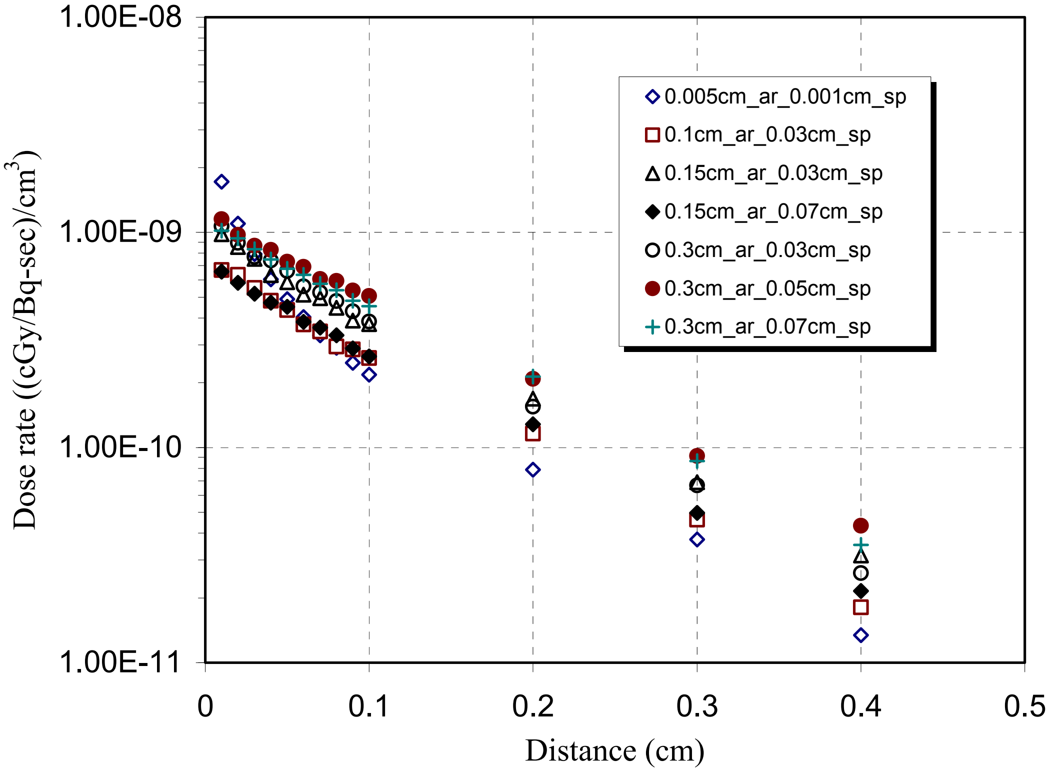

Figure III-5. Dose rate as a function of microsphere and arterial size, and source volume (Note: As shown in the caption box, 0.005cm_ar_0.001cm_sp represents 0.005 cm radius artery filled with 0.001 cm radius microspheres) detector to the source is previously depicted in figure III-3. In order to observe the differences in dose delivery to the arterial wall and peripheral area, various arterial and microsphere sizes were simulated. The smallest arterial size considered was 100 μm, packed with 20 μm (both are diameters) microspheres. The largest artery considered was 3 mm, packed with 1.4 mm microspheres. Distance (D, see figure III-3. (a)) between each cylinder (artery) varied between 1 mm and 5 mm. The results indicated that dose enhancement is significant for the closest arterial wall (0.1 mm, d) to 0.5 mm distance, d, from the surface of the primary artery in the case of larger arteries filled with larger microspheres (see figure III-6 (a) to (d)). In these cases, generally large arteries (2 mm to 3 mm diameter) with larger microspheres were more affected by the other artery for closer distance to it than the case of small arteries (0.1 mm to 0.6 mm diameter) with smaller microspheres. For example, at the closest point to the secondary artery (see figure III-6 (a), d = 0.1 mm and D = 1 mm), dose enhancement by the other artery was more than 48 to 60% for larger artery group (2 mm to 3 mm diameter), but only just over 10% for the small arteries (0.1 mm to 0.6 mm) group. The difference between the two groups diminished as the distance, d, increases and (beyond the middle of the dose point between the two arteries, e.g. see figure III-6 (f) where D = 1 mm and d = 0.6 mm), no differences were observed for artery or microsphere size.

Another significant effect is that where distance D is 3 mm, the discrepancy between the two groups was not observed. It may be that electron backscatter between the two arteries is prominent at this distance. The electron backscattering factor will be discussed later in Chapter IV.

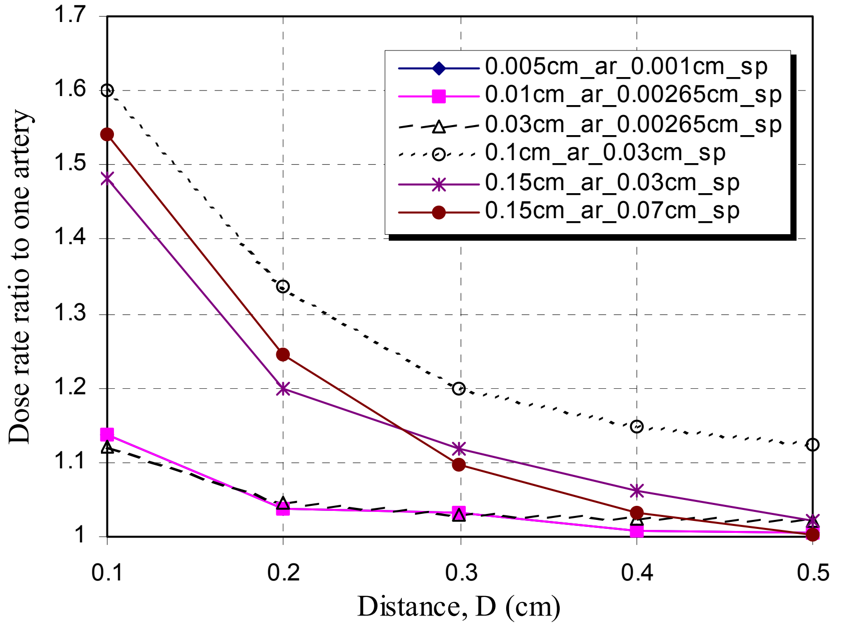

(a) Dose rate at 0.01 cm distance, d, from the primary arterial wall

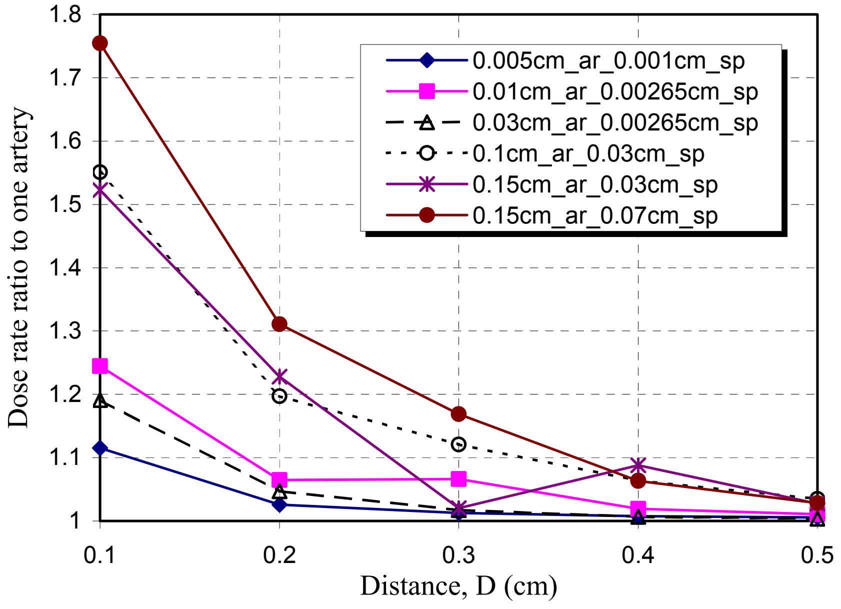

(b) Dose rate at 0.02 cm distance, d, from the primary arterial wall

Figure III-6. Dose rate ratio of two arteries filled with microspheres to one artery filled with microspheres as a function of distance from the primary artery (Note: Size and packing formation of two arteries are the same)

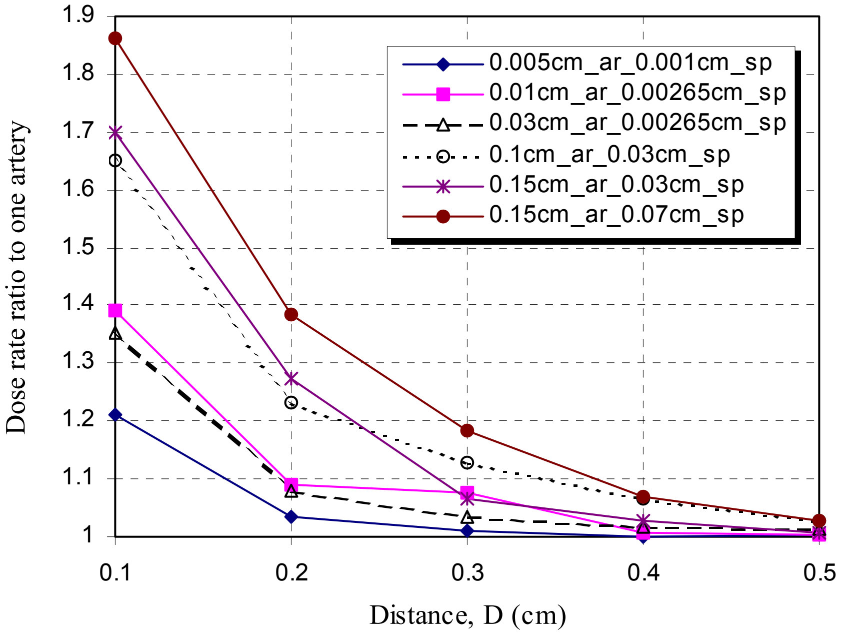

(c) Dose rate at 0.03 cm distance, d, from the primary arterial wall

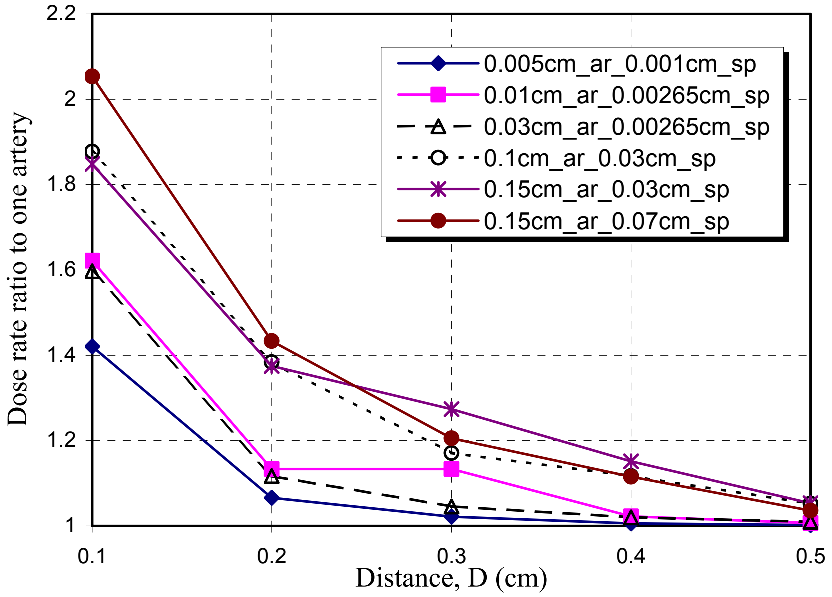

(d) Dose rate at 0.04 cm distance, d, from the primary arterial wall

Figure III-6. Continued

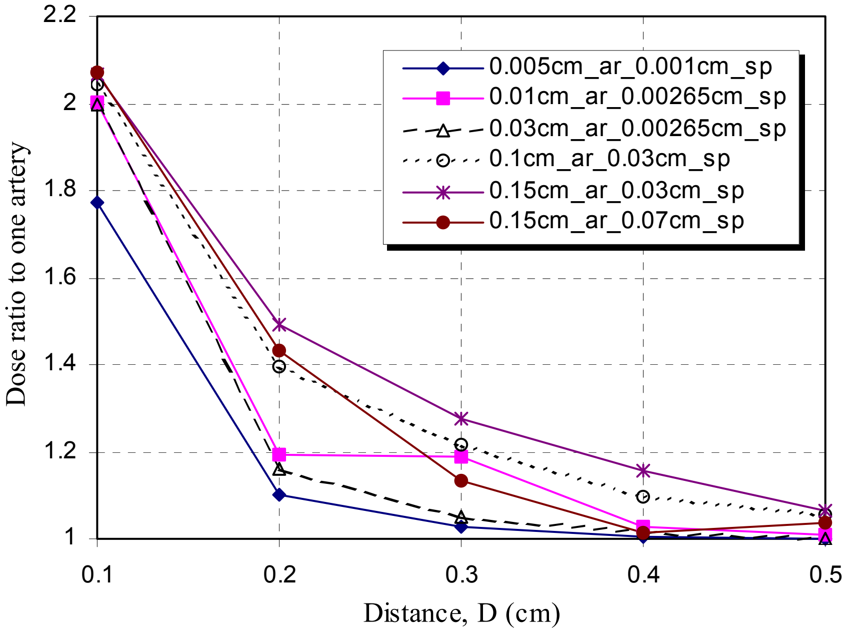

(e) Dose rate at 0.05 cm distance, d, from the primary arterial wall

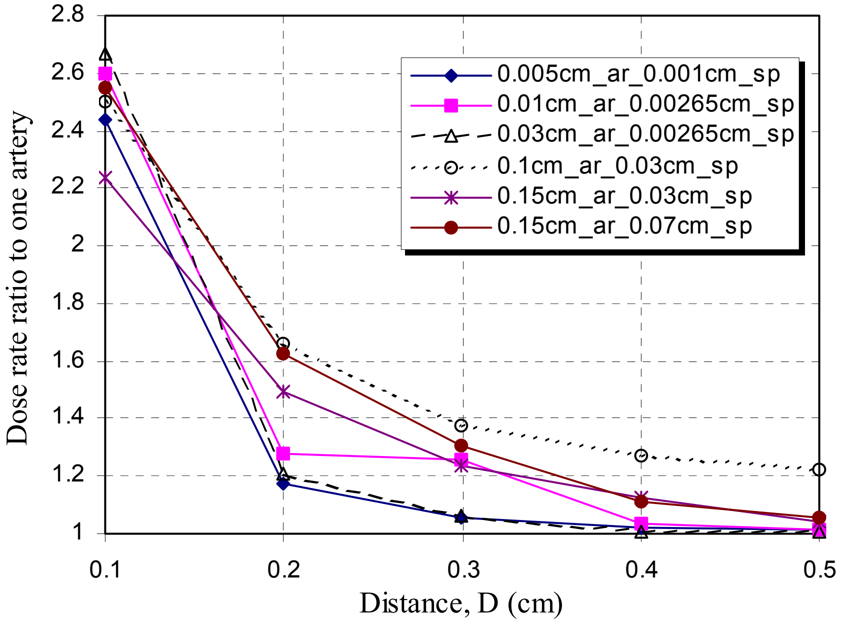

(f) Dose rate at 0.06 cm distance, d, from the primary arterial wall

Figure III-6. Continued

III-4-3. Dose rate ratio of microsphere-filled artery to solid source-filled artery

Dose rate is affected greatly by the volume of the source, because ^{142}Pr itself is a high Z material (the density of the microsphere is about 3 g/cm^3), and the short beta particle range in the source material. If the arterial size is relatively large, and the sphere size is also large compared to the beta range, vacant space in the arterial volume would be relatively larger than that in a small artery with smaller microspheres. All these factors affect dosimetry to arterial wall and make it difficult to predict. However, it is obvious that vacant space in the larger artery can potentially lower the dose rate because of less occupancy of source volume, while the relatively less absence of vacant space in small arteries filled with smaller microspheres producing higher dose rates. This effect can be observed by comparison between the artery filled with microspheres and an artery filled with uniformly distributed source material. As expected, dose rate was increased for smaller microsphere packed small arteries and decreased for the other case when these were compared with solid source filled arteries.

As shown in figure III-7, for the smallest artery (100 μm diameter) filled with smallest microsphere (20 μm diameter, 0.005cm_ar_0.001cm_sp), there was no significant difference between microsphere-packed cylinder and solid uniform source-packed source. Discrepancies between the solid source artery and microsphere-filled artery were less than 11% up to 4 mm distant from the surface, and most of the discrepancies were less than 5%. However, for medium size arteries (0.2 mm and 0.6 mm), dose enhancement was 13-25% for points near the surface. This may due to the fact that the escape of beta particles without interacting with high Z source media is

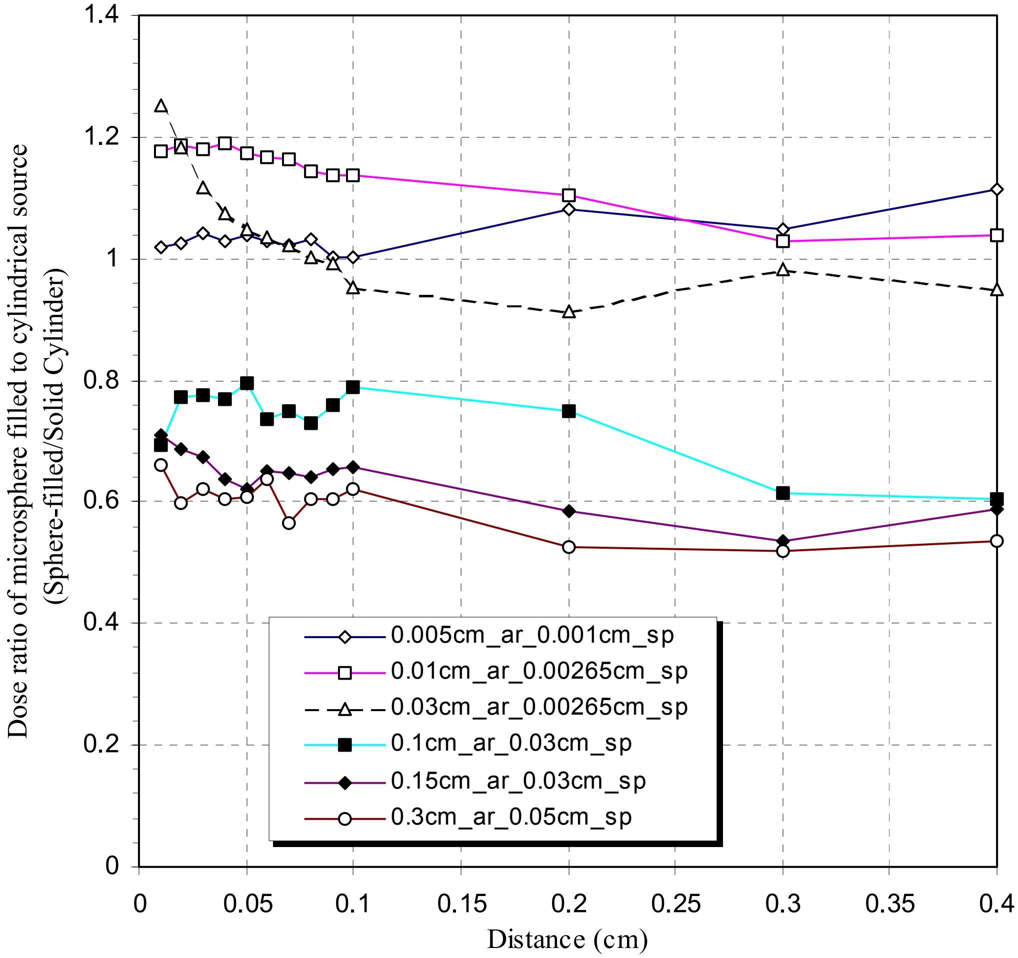

Figure III-7. Dose rate ratio between arteries filled with microsphere vs. artery filled with uniform source more probable for small arteries. Further away from the artery (around 0.8 mm to 1 mm from the surface), the dose rate for solid artery was almost the same or slightly higher than that of microsphere-filled artery. This small increase may be due to bremsstrahlung. Since there is no vacant area (filled with water) in the solid cylinder, bremsstrahlung X-rays would be generated more than in microsphere-filled arteries. For larger arteries (1 mm to 3 mm) filled with larger microspheres, dose rate was decreased compared with solid arteries, as expected.

III-4-4. Effects of cylinder height

All the cylinders calculated in this chapter were around 10 mm height for comparison purpose. For arteries filled with small microspheres, the height of the cylinder is smaller than in other cases, because of constraints in MCNP input discussed earlier. Therefore, 100 μm artery filled with 20 μm diameter microspheres, whose original height is only 0.11 mm and for a 0.6 mm artery filled with 53 μm microspheres, the original height of cylinder was only 0.0523 mm.

Calculations were performed for three times taller cylinders than the original cylinder, and the results were compared. In order to compare differences between original and taller cylinder, the paste capability in MCNP was used. Three identical cylinders were stacked and detector located in the middle of cylinder axis from the cylinder surface. For the first case (50 μm radius artery filled with 10 μm radius microsphere), discrepancy between small and 3 times taller arteries was within 15% up to 0.03 cm from the surface. However, discrepancies were increased up to 60% up to 0.4 cm distance. Certainly, higher the height, the greater dose rate was observed.

For 0.03 cm radius artery filled with 53 μm diameter microspheres, the dose rate differed by 44% at only 0.1 mm distance from the arterial surface. This discrepancy increased to more than 65% at 0.2 cm distant and beyond. However, in order to compare other arteries, the height of these arteries increased up to around 10 mm. In these cases, it was found that differences of dose rate were saturated beyond around 8 mm height. This height is close to electron range of ^{142}Pr (around 0.88 cm). Therefore, the dose rate comparison would not deviate severely from this study even though the calculation was performed for shorter cylinders just less than 1 cm. As shown in the angiographic picture (see figure II-1), the AVM arteries are severely warped in some regions, thus questions about specific effect of variation in height still remain for future study.

III-4-5. Effect of detector geometry: concentric ring vs. plane type

As shown in figure III-2, two types of detectors were used to assess doses from arteries. The comparison between the cylindrical ring and plane type detector is shown in figure III-8; discrepancies between the two detectors were less than 10% at distances up to 0.2 cm from the surface, but greatly increased thereafter. For a 0.15 cm artery with 0.03 cm microspheres the difference was more significant than in smaller arteries, and this is due to discrepancies in detector volume. As detector moves away from the cylinder, the volume of the concentric ring is gets larger, and this effect is more prominent for larger cylinders than small ones. However, beyond 2 mm from arterial wall, dose rate is significantly affected by detector geometry. However, as mentioned, these distances may not be important clinically to induce

.

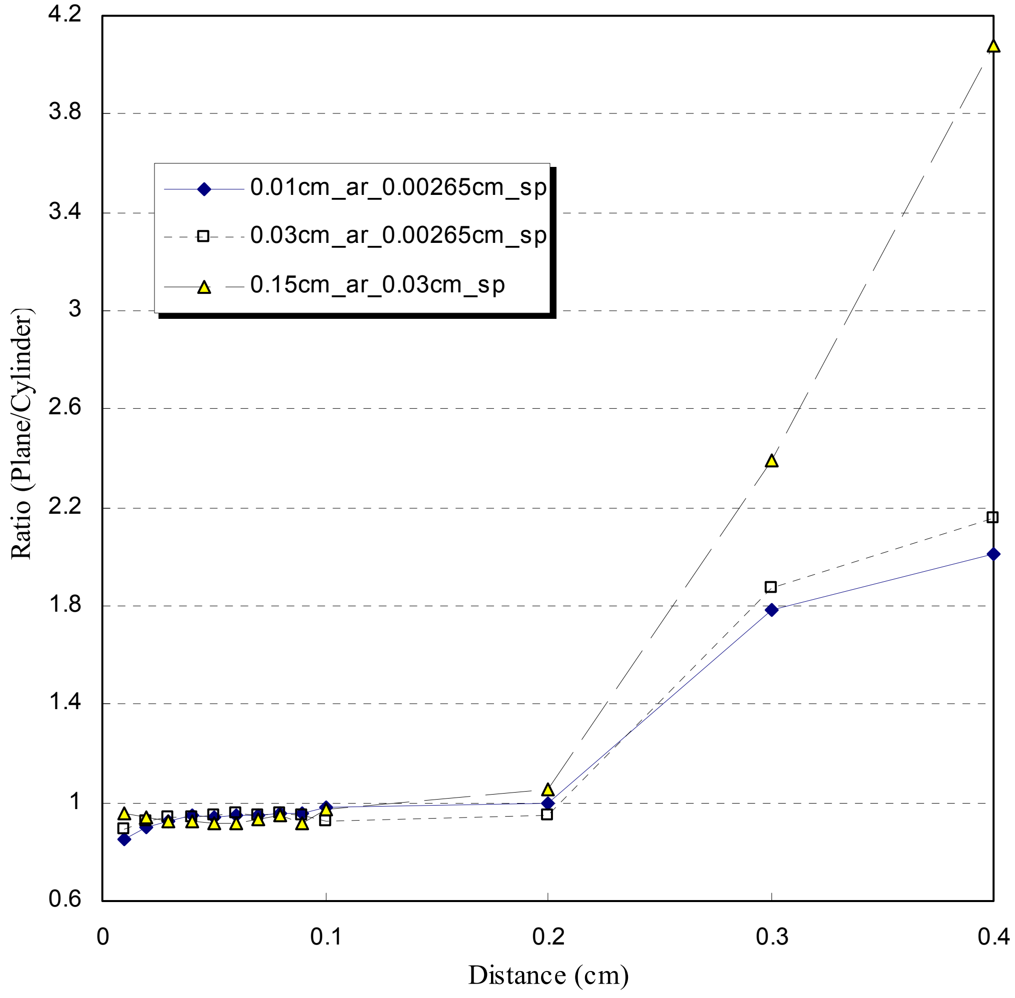

Figure III-8. Dose rate ratio between plane cubic detectors vs. concentric ring detectors hyperplasia of arterial wall. Therefore large discrepancies beyond 2 mm from artery by using different detector would be meaningless for clinical application.

III-4-6. Dose contribution by gamma energy emission from source

As stated in previous Chapter II, ^{142}Pr emits not only beta particles but also gamma rays. However, the gamma energy contribution to dose as a fraction of total dose was less than 1/1000. Most of the dose was from beta particles for small arteries with small microspheres for clinically significant distance away from the arterial wall (up to 4 mm). The gamma contribution was less for larger arteries with large microspheres. In order to obtain reasonable gamma energy contribution data by MCNP calculation, more than 0.1 billion or even order of billions of particle histories would be needed. Therefore, it would not introduce significant error even if the gamma contribution of ^{142}Pr is ignored.

III-5. Conclusions and discussions

Dose rates around cylinders randomly packed with microspheres was calculated using MCNP. The AVM feeding arteries were simplified as a cylinder packed with microspheres. With this geometry, various dose rate effects as a function of microsphere and arterial size were observed. The dose rate was affected by packing formation, diameter sizes of artery and microsphere, distance between neighboring artery, and length of artery.

Small arteries filled with relatively small microspheres have higher dose rates around arterial wall than arteries filled with relatively large microspheres. If the ratio of diameter of artery to microsphere diameter is about a factor of 10 (e.g., 0.3 cm artery with 0.03 cm microsphere), dose rate is significantly higher than the same sizes of arteries are filled with larger sizes of microspheres.

Specifically, packing formation greatly affected the large artery (0.1 to 0.3 cm radii) with large microsphere size probably because of the vacant spaces between microspheres. In addition, there were large variations in dose distribution along the arterial wall for large arteries with large microspheres. To overcome dose rate variation by this effect, several calculations were done and averaged, particularly for large arteries with large microspheres, for reasonable comparison with other arteries. On the contrary, small arteries with small microspheres (50 μm radius artery filled with 10 μm radius microspheres) was affected less by packing formation. For this case, it is practical to assume the cylinder as simple cylindrical or line source. This effect is closely related to beta particle range and the combinations between sphere and arterial sizes because microsphere itself is a high Z material.

Dose rate ratios between the same sized cylinder filled with microspheres and solid cylindrical source occupying the whole cylinder were compared. The result was interesting because of strong dependence on the arterial size. As arterial size increased, the dose rate of solid source was higher than that of cylinder filled with microspheres.

Height of simulated cylinder was varied but was usually longer than 1 cm except in certain cases where small arteries were filled with very small microspheres and when medium size arteries were filled with small size microspheres. If the height is about 1 cm, which is longer than the electron particle range of ^{142}Pr, a few discrepancies exist. However, by using duplication function embedded in MCNP, the same size of cylinders were stacked and calculated again. For longer cylinder height, the first case (100 μm diameter artery filled with 20 μm diameter microsphere, height is 0.11 mm) was not affected significantly, but a second case (0.6 mm diameter artery filled with 53 μm microsphere, height is 0.0523 mm) was affected because of the very short length of the cylinder. This study was performed for short artery sections, and a more specific study of dose as a function of cylinder height remains for the future.

Significant differences were observed as a function of a shape of detector. For cylindrical ring detectors, showed lower dose rates than that of plane cubic detector. However, the effect was significant only beyond 2 mm from the surface where clinical implication is less important. In addition, the plane detectors used in this study were used for comparison purposes only, so discrepancies from this effect could be minimal.

CHAPTER IV

DOSE CALCULATION OF ^{142}Pr IN WATER FOR VARIOUS BRACHYTHERAPY SEED TYPES

IV-1. Introduction

There are widely used sources such as ^{32}P, ^{90}Sr/^{90}Y with established dosimetry; however, exploring other beta emitting isotopes is still attractive because some useful beta emitters may exist that can overcome several problems associated with current sources available for brachytherapy use. These problems include lower beta energy, high costs, and chemical toxicity to human body, among others. In this chapter, ^{142}Pr, a beta-emitting radioisotope, which has potential applications in intra-arterial and ophthalmic diseases was studied for various source geometries.

Point, solid cylinder, cylindrical stent, disk, and sphere geometries cover the range of current applications. In traditional interstitial brachytherapy, which typically utilizes a gamma source with a dose rate specified at 1 cm from the source as a reference position for longer distance, the effects of low-energy photons such as secondary X-rays and electrons were sometimes being ignored, but beta and gamma doses around single microsphere were investigated using MCNP as well as DPK. Results of MCNP and DPK were compared and differences between these two methods were found, particularly near the end of the range of the beta particles.

In this chapter, two beta spectrum generation methods, SADDE and LOGft, were used and differences in dose profiles depending on the input spectrum were observed too.

IV-2. Source and detector geometries

The geometries considered in this study are point, solid cylinder (wire), stent (cylindrical shell), disk, and sphere. These geometries bound all the major seed types that are commonly used for therapeutic purposes.

The point source was a dimensionless point located at the center of a sphere of water. In the Monte Carlo calculations, the detectors were spherical concentric water shells 0.002 cm thick, with their midpoints located between 0.01 cm and 1 cm.

For the wire source, an area 2 cm in length and 0.3 cm in diameter was simulated in a large water phantom (diameter=30 cm) for comparison with the stent type source. The wire was assumed to be composed solely of praseodymium (Z=59). The radiation from the source was deposited in concentric rings 1 cm height and 0.002 cm thick in the axial direction of the source.

The stent type source could be compared with published results (Prestwich 1996), and has source geometry identical to the wire except that the source region is a 2.5×10^{-5} cm thick cylindrical shell. The detectors were located in a similar manner as with the wire source. The cylinder material was composed of water, because the source material is very thin and the composition of the interior of the cylindrical shell depended on the properties of the angioplasty material.

The simulated ophthalmic applicator was a disk source 1 cm in diameter. The disk was located on the center of a plane in a large spherical phantom (diameter = 30 cm), and the thickness was essentially zero. The detectors were small cylinders oriented with the circular face toward the disk, and these were aligned along the central axis of the disk. The height and diameter of the cylinder were 0.006 cm and 0.6 cm, respectively.

Spherical sources were considered in this study because this form is useful for hepatic tumor and arteriovenous malformation (AVM) treatment. In order to mimic to a realistic application, the physical parameters of the microspheres used in the animal tests were used as a benchmarking source. Dose rate calculation was performed as a function of sphere diameter. Contents of microspheres are: 10.5$^{a}/_{o}$ praseodymium, 62.3$^{a}/_{o}$ oxygen, 10.5$^{a}/_{o}$ aluminum, and 15.8$^{a}/_{o}$ silicon, and the density of this material is approximately 3 g/cm^3. The radii of the microspheres varied from 25 μm to 0.15 cm, and the dose profiles for selected diameters were calculated. The calculation was performed using MCNP as well as a DPK method. Source to detector geometry was essentially that of a point source, and the source sphere was located at the center of a concentric spherical water shell (detector).

IV-3. Monte Carlo calculation

This study used MCNP (Briesmeister 2000) to perform the Monte Carlo calculation. Although the code has the ability to transport neutron, electron and gamma particles independently or in a couple or a triplet, this must be initiated by one of the particles. Because ^{142}Pr emits electron and gamma particles simultaneously, separate calculations were needed and the sum of them taken as the total dose rate. For electron transport, all secondary particle effects (including bremsstrahlung) were simulated together by coupled electron-photon transport. *F8 tally was used to express absorbed dose in energy (MeV), and it was divided by the mass, and then multiplied by appropriate conversion factor to get dose. The ITS 3.0-style energy indexing algorithm was selected over the inherent MCNP-style algorithm through an option in the DBCN card, because the ITS 3.0-style algorithm gives results closer to those achieved through experimentation.

In order to reduce result error to within 10%, differing numbers of histories were chosen depending on the detector size and according to the source geometry. Generally, 10 million particles were initiated for electron transport and 100 million particles were chosen for gamma transport.

IV-4. Comparison of MCNP fit results with DPK results

The MCNP results were fitted with the function presented by Prestwich *et al.* (1995). The function was fitted for dose around a ^{32}P stent, but its application to sphere source was reasonably accurate up to 0.5 cm from the sphere surface. The dose distribution is expressed as

$$D(x) = a_1 F_1(x) + a_2 F_2(x)\,, \qquad (4\text{-}1)$$

where D represents dose rates in mGy/MBq-h. Specifically,

$$F_1(x) = e^{-\lambda x} / x^{1/3}\,, \qquad (4\text{-}2)$$

where x is the distance from the sphere surface. This term accounts for smaller distances from the surface where dose is higher, and the second term is for larger distances where relative dose rate is lower. The second term is expressed as

$$F_2(x) = e^{-\mu x} / (1 + e^{(x - x_0)/\alpha}). \qquad (4\text{-}3)$$

According to Prestwich *et al.* (1995), the six parameters (a_1, λ, a_2, μ and α) are inversely proportional to volume of a source, but this effect was only observed for larger diameters of microspheres (0.1 cm to 0.3 cm) in this study.

IV-5. Results and discussions

IV-5-1. Dose rate for the point source

Dose rates for the point ^{142}Pr source were calculated using DPK as well as MCNP Monte Carlo method. Beta emission spectra data were incorporated into MCNP input; spectral data generated by both LOGft and SADDE MOD2 were compared. As shown in figure IV-1, discrepancies were observed at the end of the electron path. LOGft-generated beta input showed higher dose rates than the SADDE-generated input for all distances except for distances very close to the detector point (~ 0.04 cm). DPK calculation based on the SADDE-generated beta spectrum showed results similar to the MCNP calculation. However, it showed larger discrepancies at the end of the beta particle range (~ 0.88 cm range: $1.8 \times X_{90}$). Compared to MCNP calculations, DPK method underestimated the dose rate except at short distances (~ 0.04 cm). This effect may be caused by energy straggling due to secondary particle effect that is not satisfactorily incorporated into point kernel data. It is encouraging that results obtained using the same spectrum data (SADDE MOD2) for both MCNP and DPK calculations matched well, with less than 20% difference in dose rate for up to 0.6 cm distance. However, these results indicate that using different spectrum generation codes may introduce large differences in dose rate at greater distances.

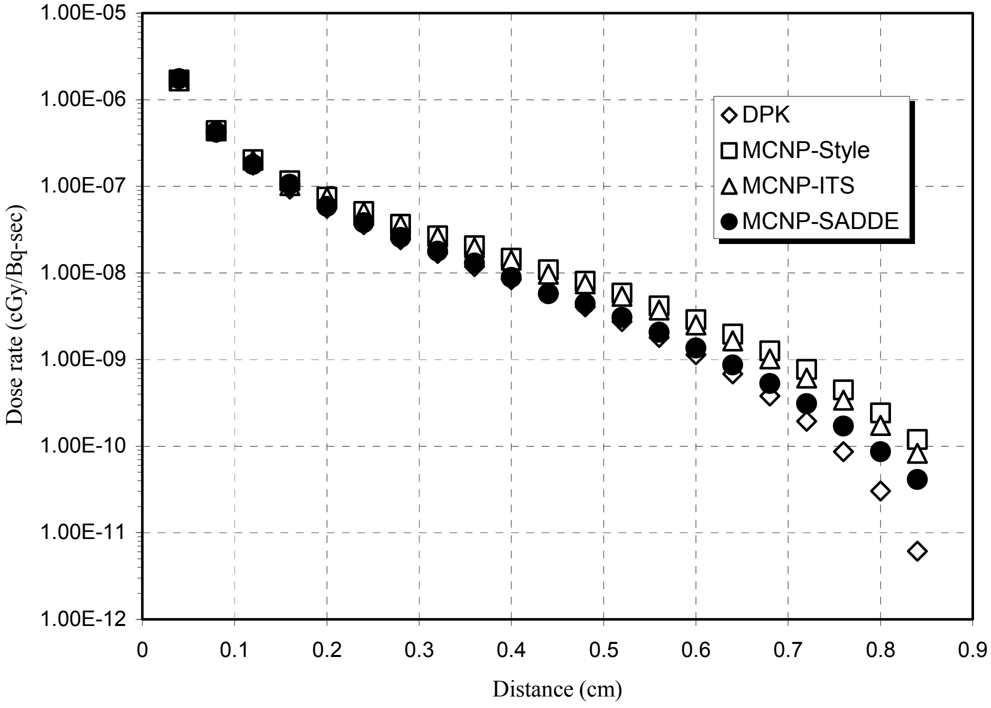

Figure IV-1. Dose rate of ^{142}Pr point source as a function of different spectrum generation code and calculation method (Note: MCNP-ITS and MCNP-Style represent LOGft generated beta spectrum and use of ITS 3.0 and MCNP style algorithm, respectively. MCNP-SADDE used SADDE MOD2 generated beta spectrum and used ITS 3.0 algorithm. ITS 3.0 algorithm was used hereafter mentioned otherwise)

IV-5-2. Dose rate for stent and solid wire sources

To investigate the applicability of ^{142}Pr for use in a stent, dose rates were calculated as a factor of axial distance from the surface of the source. Dose rate decreased rapidly as the distance increased, and contribution by the 3.7% gamma energy portion dominated at 0.81 cm and beyond from the source surface (figure IV-2). Because of gamma energy contribution, the dose rate did not significantly decrease in the extremity of the range. Figure IV-3 shows that in the wire geometry, the dose rate fall-off was much quicker than in that of the stent. Comparison of dose decrease with ^{32}P stent is shown in figure IV-4. At a distance of 0.65 cm from the source surface, dose rates were 0.15% (wire) and 0.137% (stent) of those at 0.01 cm from the surface. However, the effect of self-absorption of the beta ray in solid medium was significant in the vicinity of the source surface area; therefore dose rate for the wire was much lower than for the stent. At a distance of 0.01 cm from the source surface, the dose rate from the stent was more than 5.8 times higher than that of the solid wire source.

Although a stent may induce restenosis in some cases (Nath *et al.* 1999), the stent type is better suited to irradiation of unwanted healthy tissues than the solid wire type because of higher dose rate in short distance and rapid dose fall-off at longer distances. Therefore, design improvement of the stent source and clinical application technique would yield higher dose rate to the arterial wall with smaller activity. Prestwich (1995), using the same ^{32}P geometry, calculated a dose rate 0.05 cm from the source surface of about 540 mGy/MBq-hr. In this study, the dose rate of ^{142}Pr was estimated to be around 440 mGy/MBq-hr at the same distance.

This is 0.83 times smaller than that of ^{32}P calculated, but dose rate decrease as

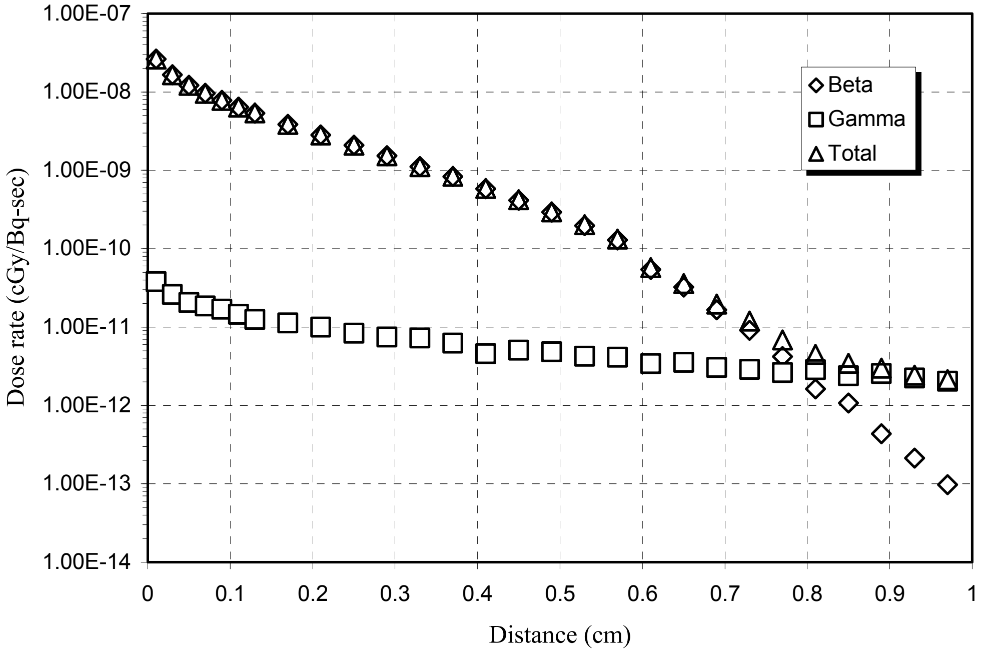

Figure IV-2. Dose rate of ^{142}Pr stent as a function of distance

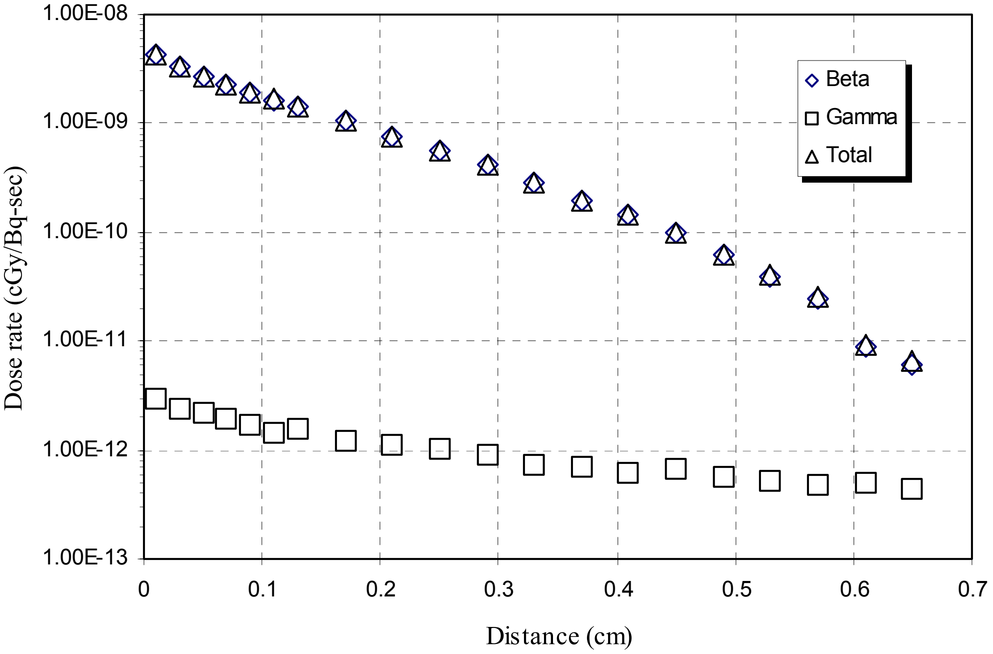

Figure IV-3. Dose rate of ^{142}Pr wire (solid cylinder) as a function of distance

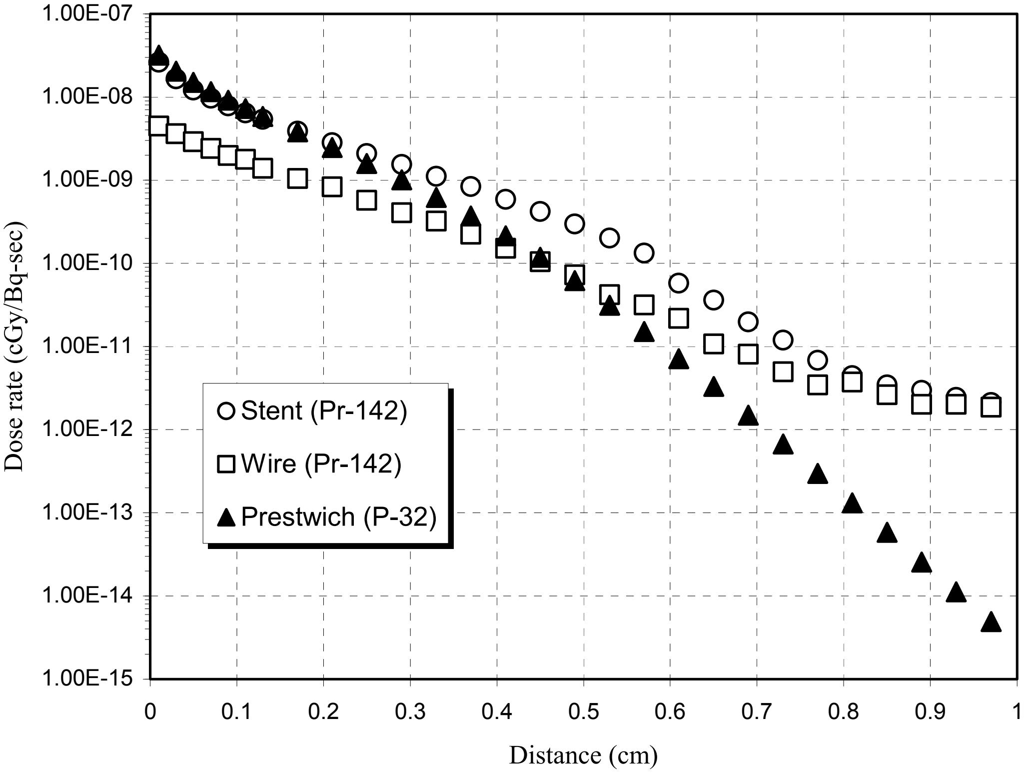

Figure IV-4. Dose distribution of ^{142}Pr stent and wire sources, and ^{32}P source that was analytically obtained data from Prestwich (1996) a function of distance was not significant because mid-range electron energy (~ 1MeV) of ^{142}Pr spectrum contributes to dose profile at greater distances. Although gamma contribution from ^{142}Pr in the 0.4 to 0.7 cm range was not a primary factor of the total dose rate, a significant amount of gamma energy was observed in the tail of the straggling range. However these dose rates are not significant when considering the distances in question in a clinical situation.

Direct comparison of these two radioisotopes can be misleading because detector size and assembly conditions differed slightly. Another possible reason for the slightly smaller value of ^{142}Pr when calculated by MCNP is that a DPK calculation usually overestimates dose at very short distances from the source. This effect may not have had much impact on the DPK method in this study, but if Prestwich used a similar algorithm, it may have contributed to the overestimation. Even from these calculations, however, ^{142}Pr guaranteed a dose rates per activity equal to that of ^{32}P in the points within the target area of clinical interest. Furthermore, because praseodymium is not known to be a bone-seeker such as phosphorus or strontium, shielding elements, which can affect dose characteristics, may not be necessary as for ^{32}P or ^{90}Sr/^{90}Y. Also praseodymium can easily be mixed with other inorganic materials in high concentration to form chemically stable glass-like material, and this is another physical advantage of using ^{142}Pr source rather than using ^{32}P and ^{90}Sr/^{90}Y for brachytherapy purpose.

IV-5-3. Dose rate for a disk source

Characteristics of ^{142}Pr as an ophthalmic applicator were simulated by a simple disk source (figure IV-5). The result was compared with Cross *et al.*'s (2001) results. In their results, ^{106}Ru/^{106}Rh and ^{90}Sr/^{90}Y are comparable to ^{142}Pr because of their geometrical similarities. Concave ophthalmic applicators were excluded from the comparison because the differences in geometry lead to a meaningless comparison; Cross *et al.* (2001) found up to 30% difference between the experimental and theoretical calculation results for the same concave type applicator.

Although the diameters of the ophthalmic applicator used in this study and that of Cross *et al.* (2001) differed, similar beta particle ranges made the difference between ^{142}Pr and ^{90}Sr/^{90}Y negligible. For this comparison, the ^{90}Sr/^{90}Y disk applicator was NEN 0258 made by New England Nuclear. The activity is dispersed through material 1 mm thick and 0.86 mm in diameter. It is mounted on a thick stainless-steal backing and covered by a 0.1 mm stainless window. As shown in figure IV-6, dose rate was normalized (dose rate at distance 0.1 cm from the source normalized to 1) and the data obtained from Cross *et al.* (2001) were plotted together with results of this study for comparison purposes. Relative dose decrease for ^{106}Ru/^{106}Rh, however, was not as significant as other two isotopes due to its higher beta energy (E_{max} = 3.54 MeV). Active diameter of this source is 20.5 mm and is mounted on a silver backing, about 0.9 mm thick, and covered by a 0.1 mm thick silver window (manufacturer: BEBIG Trade Inc.).

Due to similar maximum beta energies, the ^{90}Sr/^{90}Y (E_{max} = 2.28 MeV) disk source showed dose fall off patterns similar to that of ^{142}Pr (E_{max} = 2.16 MeV).

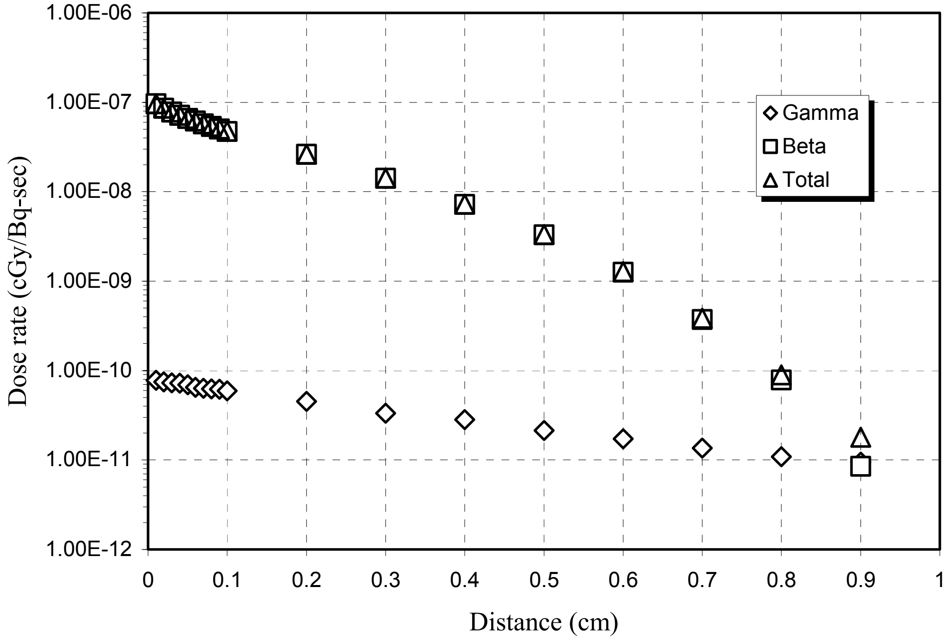

Figure IV-5. Dose rate of ^{142}Pr disk source

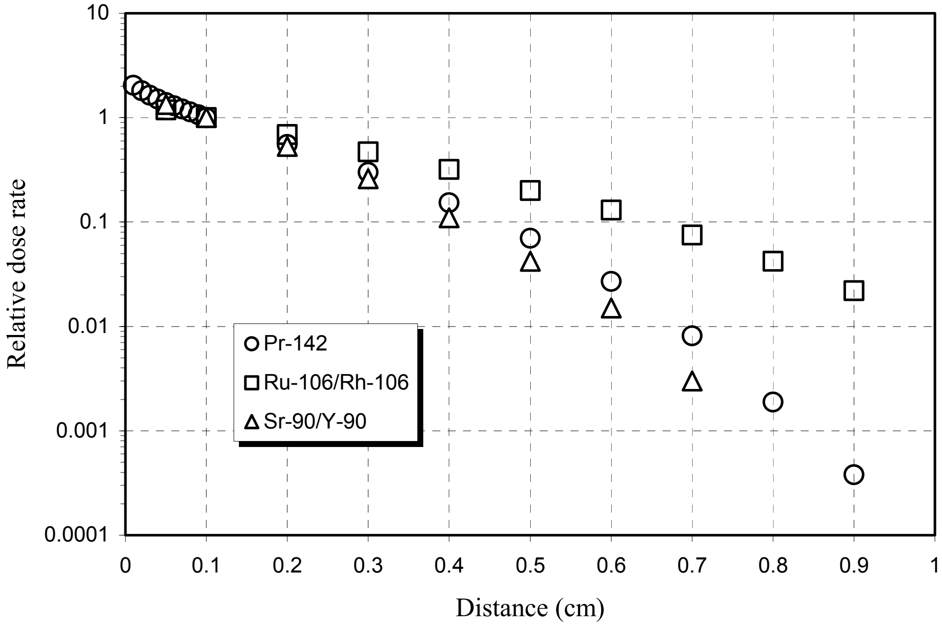

Figure IV-6. Relative dose rates of ^{142}Pr, ^{106}Ru/^{106}Rh and ^{90}Sr/^{90}Y disk sources (Cross *et al.* 2001). Dose rate normalized to 0.1 cm distance from the source surface. (Note: Diameters are 2.05 cm and 0.86 cm for ^{106}Ru/^{106}Rh and ^{90}Sr/^{90}Y, respectively)

For example, relative dose rates for ^{142}Pr and ^{90}Sr/^{90}Y were 1.4 and 1.34 at 0.05 cm, respectively, when the reference point (the point where relative value equals one) was 0.1 cm.

As described in section IV-2, the geometry of ^{142}Pr was simplified to a dimensionless thickness while the ^{90}Sr/^{90}Y sources used in the Cross (2001) were encapsulated in thin silver. In a real-world application in which a source-backing material is present, the relative dose rate of ^{142}Pr could be different from this result because of the shielding effect and backscatter. However, the results indicate that the efficacy of ^{142}Pr as an ophthalmic applicator is promising compared to sources currently being used.

IV-5-4. Dose rate for sphere sources as a function of radius

Spherical geometries of radioactive material have been investigated for radiation protection concerns for exposures from a hot particle. Another potential area of interest in spherical source geometry is radioimmunotherapy applications. For radioimmunotherapy, dose has been calculated in a uniformly distributed source sphere as absorbed fractions (Siegel *et al.* 1994). However, in most hot particle cases, the spherical radioactive source is considered to be located on the interface between the air and skin tissue, or sometimes between the air and the surface of the clothing. Therefore minor modifications of VARSKIN MOD2 were necessary to address an internal source in a body (sphere source submerged in water).

The results are plotted together as a function of various microsphere in figure IV-7. As shown in figure IV-8, the larger the diameter of the microsphere, the lower the dose rate obtained, because of self-absorption in the source matrix. The dose reduction ratio, however, was not as rapid as the volume increase ratio, but it was significant for relatively small size changes. For example, a 0.03 cm radius microsphere is 1728 times larger than the 25 μm radius microsphere that was used for animal studies (this radius is in the acceptable range in quality control, 0.00265 cm ± 7%), but the dose rate was reduced by less than half.

Dose rates achieved through DPK and MCNP were compared. As shown in figure IV-9, (a) through (f), dose rate was plotted against distance around spheres from 50 μm to 0.3 cm in diameter. From these calculations, DPK method generally showed higher dose rates than that of the MCNP for short distances from the spheres, but the MCNP showed higher values than that of the DPK at greater distances.

IV-5-5. DPK and MCNP results fitted to a nonlinear function for microspheres as a function of diameter

MCNP result was fitted to a nonlinear function using eq. (4-1) with the ORIGIN® spreadsheet program, and it was compared with the results from DPK analysis. Calculated parameters were tabulated in table IV-1. There are no correlations among the parameters among the spheres were irrelevant, as Prestwich *et al.* (1995) and Prestwich (1996) suggested, but DPK results agreed well for small distances.

As shown in table IV-2, DPK results corresponded well with MCNP analysis (within 67%) for distances up to 0.64 cm. For shorter distances, including the clinically critical area (~ 0.28 cm), discrepancies between DPK and MCNP were

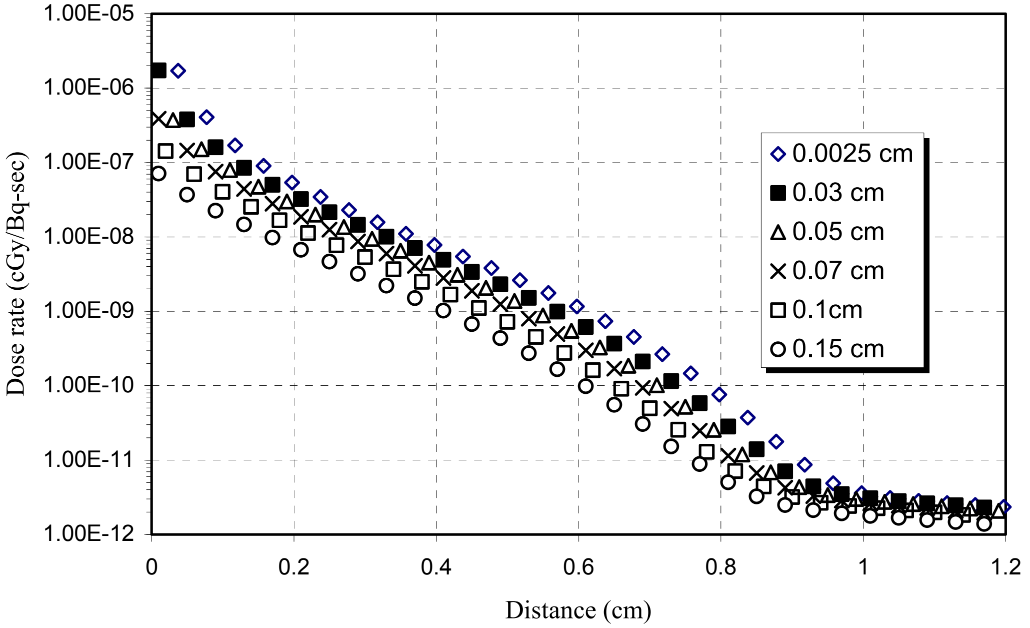

Figure IV-7. Dose rate as a function of microsphere radius

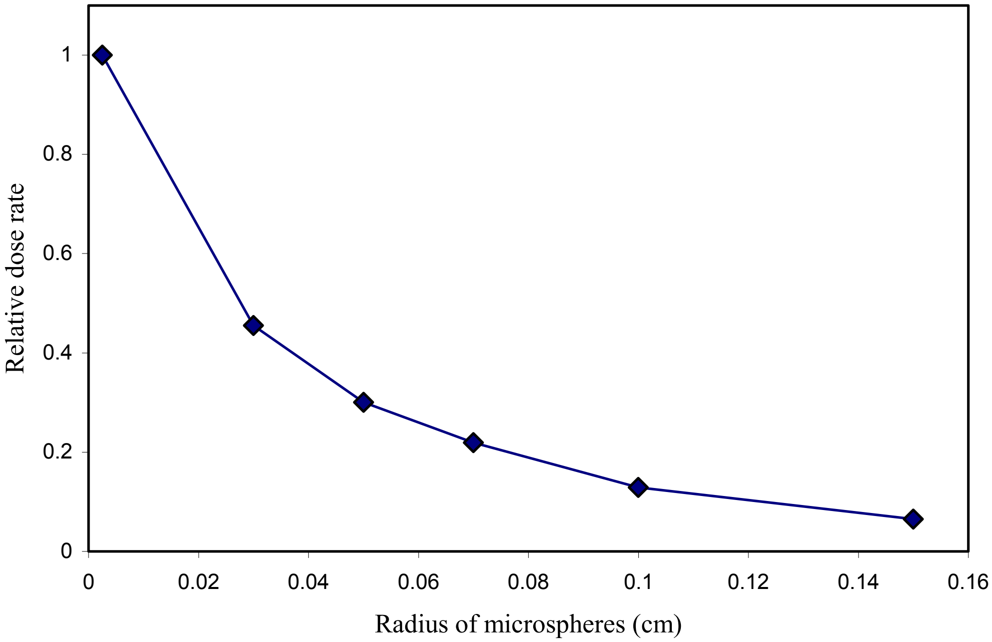

Figure IV-8. Dose rate as a function of microsphere radius. Dose rate was normalized to 0.0025 cm radius microsphere and 0.1 cm distance from the source surface (normalized to 1). Other results from various radii are relative value of 0.0025 cm microsphere

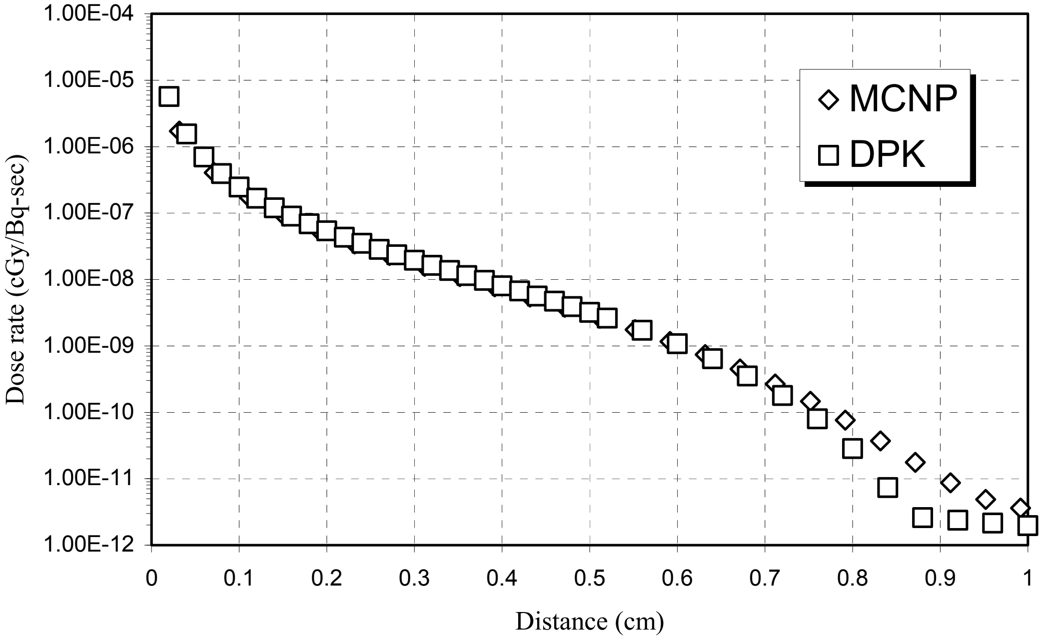

(a) 0.0025 cm radius sphere

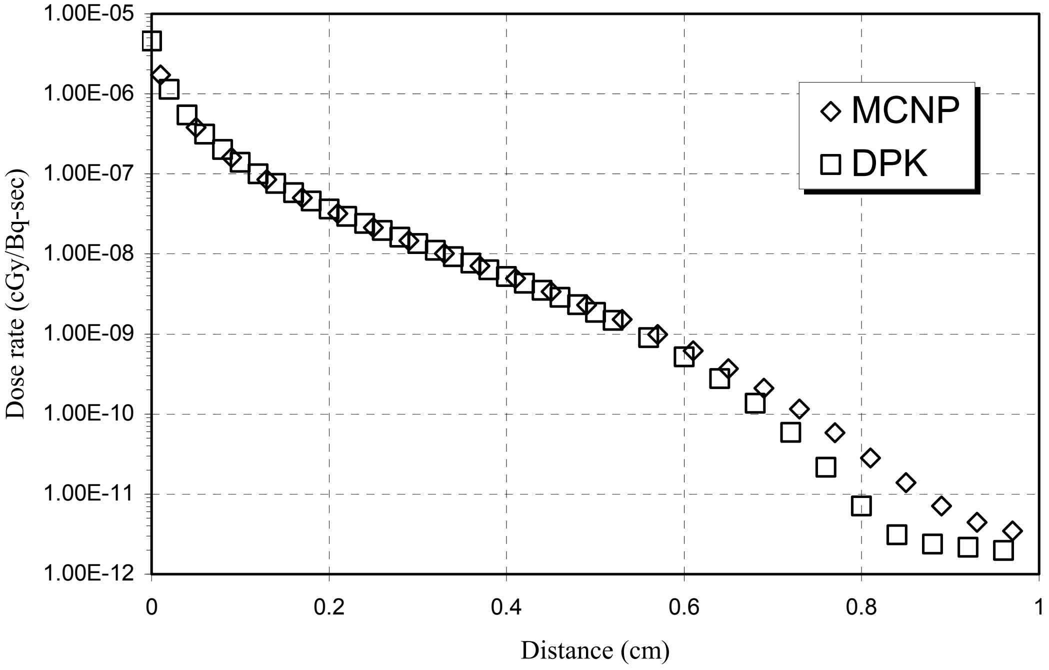

(b) 0.03 cm radius sphere

Figure IV-9. Comparison of dose rate between DPK and MCNP calculation as a function of microsphere radius

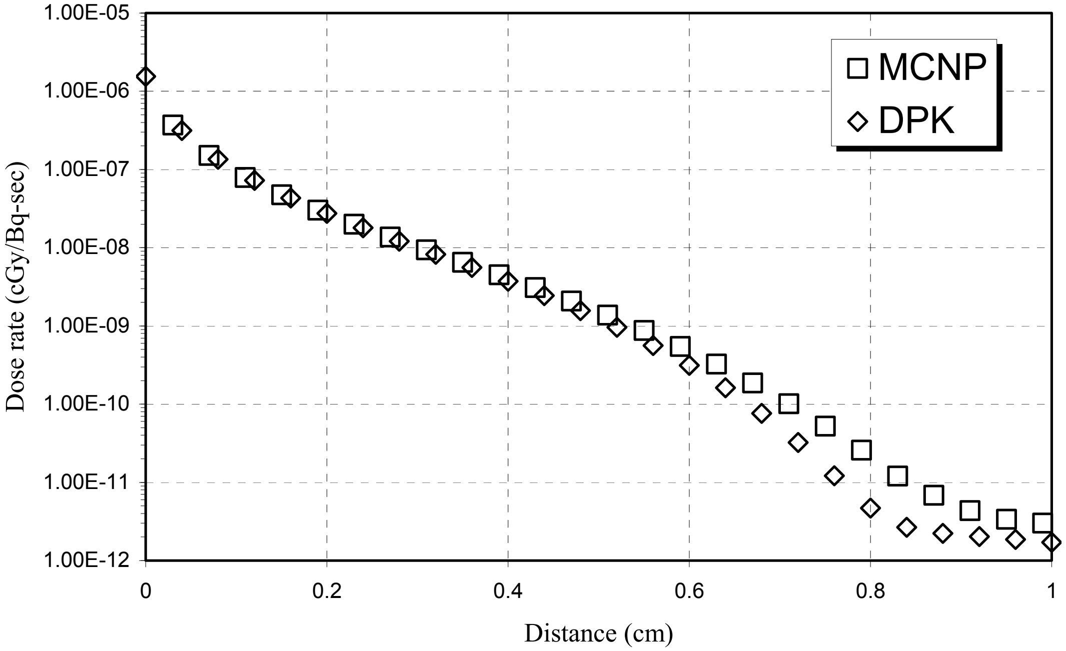

(c) 0.05 cm radius sphere

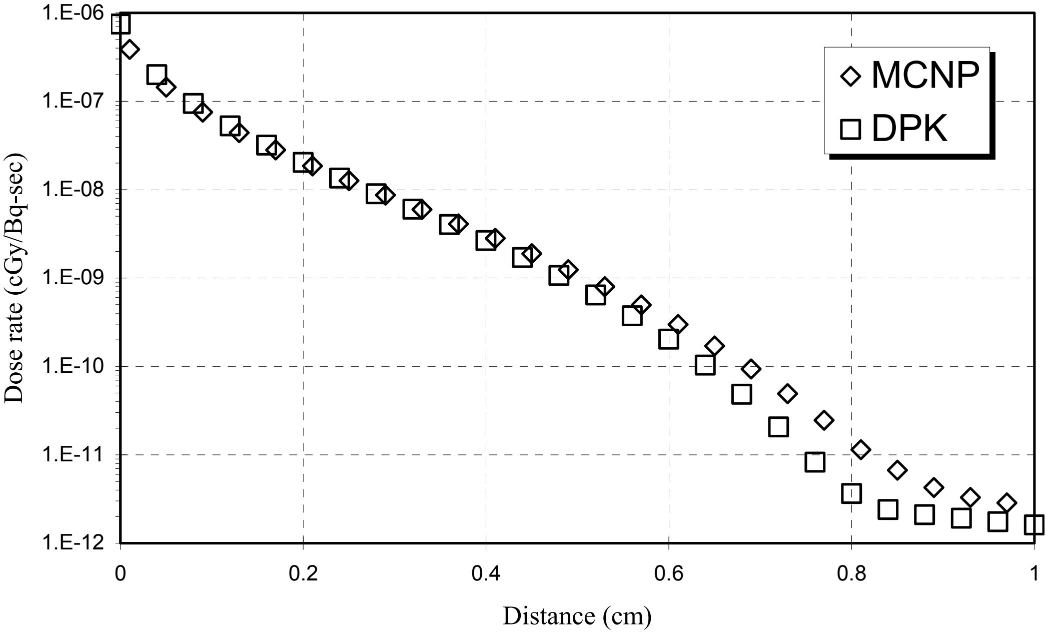

(d) 0.07 cm radius sphere

Figure IV-9. Continued

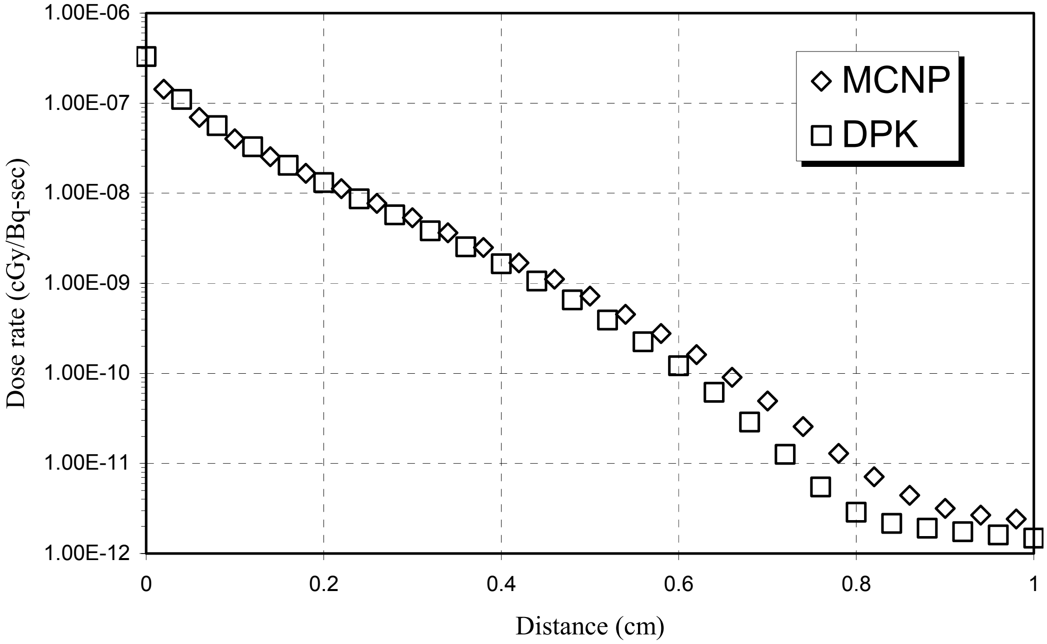

(e) 1.0 cm

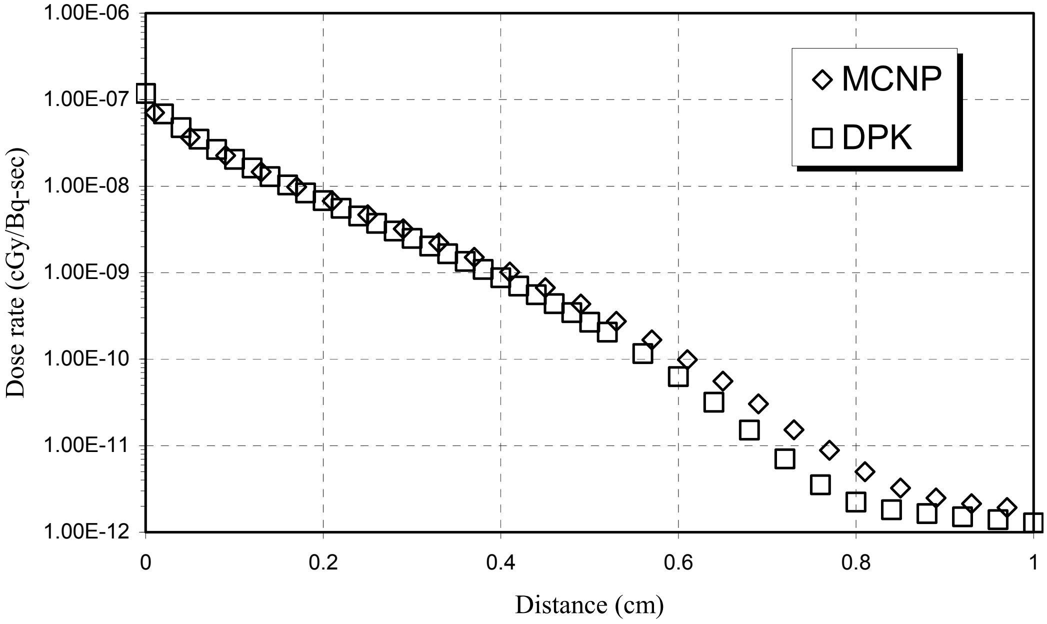

(f) 1.5 cm

Figure IV-9. Continued

Table IV-1. Calculation parameters used for non-linear fit.
(Diameter is for microspheres)

Diameter (cm)	a_1	λ	a_2	μ	x_0	α
0.005	85.27034	10.04676	64203.45	50.65289	-1.74369	0.58652
0.06	160.693	36.44154	229.3349	10.82913	1.09E+18	2.74E+22
0.1	60.17832	25.85934	58.41765	9.23102	0.66914	0.05256
0.14	28.40219	18.3659	31.88018	8.27584	0.59277	0.06356
0.2	12.34774	17.04632	22.53743	8.36187	0.58443	0.07485
0.3	2.80239	18.25005	16.08921	9.27542	0.62432	0.0417

Table IV-2. Ratio of DPK and MCNP calculations for microspheres as a function of diameter

Distance (cm)	Ratio (DPK/MCNP), just below are diameter of microspheres in cm					
	0.005	0.06	0.1	0.14	0.2	0.3
0.04	1.0079	1.0645	1.1236	1.1473	1.1492	1.1365
0.08	1.0303	1.0636	1.0695	1.0701	1.0762	1.0390
0.12	1.0528	1.0248	1.0085	1.0387	1.0276	0.9830
0.16	0.9997	0.9930	0.9895	1.0207	0.9939	0.9452
0.20	0.9878	0.9862	1.0111	1.0003	0.9658	0.9252
0.24	1.0191	1.0077	1.0679	0.9861	0.9350	0.9087
0.28	1.0826	1.0557	1.1458	0.9555	0.9058	0.8931
0.32	1.1731	1.1170	1.2403	0.9263	0.8707	0.8711
0.36	1.2776	1.178	1.3462	0.8843	0.8322	0.8412
0.40	1.3924	1.2056	1.4370	0.8387	0.7922	0.7937
0.44	1.5043	1.2975	1.5074	0.7787	0.7631	0.7402
0.48	1.5983	1.3180	1.5411	0.7397	0.7126	0.6780
0.52	1.6672	1.2949	1.5141	0.7044	0.6814	0.6148
0.56	1.6602	1.2149	1.4204	0.6871	0.6689	0.5685
0.60	1.5949	1.0807	1.2571	0.6947	0.6464	0.5699
0.64	1.4430	0.8926	1.0384	0.7223	0.6360	0.6600

generally around 10%. These results indicate that using analytical fit of MCNP results for a quick estimation will not significantly skew the results for pre-clinical application. Discrepancies between the fitted and MCNP calculated data were especially small for larger sphere diameters.

According to the calculation results, DPK overestimated the dose rate near the source, but over longer distances MCNP overestimated the dose more than DPK calculation, respectively. This is perhaps due to bremsstrahlung X-rays from source media that were not properly incorporated into the DPK calculation. This effect has been documented elsewhere (Cho 1997). Also, using different beta spectrum generation methods (in this case, SADDE MOD2 was used in DPK while LOGft used in MCNP), may affect the discrepancy between these two methods. Table IV-2 lists data only up to 0.64 cm distant from the source surface, because beyond that range the total accumulated dose is comparable with the radiation dose from natural background, and also exceeds X_{90} distance (~ 0.49 cm). Since the activity of a microsphere for therapeutic use in a hepatic tumor is in the order of only tens of Bq (around 50 Bq for Campbell *et al.* 2001), data from beyond this distance is not significant. For AVM treatment, lower activity levels are needed to induce hyperplasia of arterial walls (thus clogging unwanted arteries), so data from distances over 0.6 cm can be disregarded for this therapeutic application as well.

IV-6. Conclusions

Dosimetric characteristics of ^{142}Pr were estimated using MCNP and DPK calculations for dose rates around the source as a function of central axial distance.

For the point source, the dose rate as a function of distance in the water was calculated using different dose calculation methods with the different spectrum generation codes LOGft and SADDE MOD2. The LOGft-generated beta input showed higher dose rates than the SADDE-generated input for all the distances except those very close to the detector point (~ 0.04 cm). However, results from calculations using SADDE MOD2, DPK and MCNP agreed to within 20%.

The dose profile of ^{142}Pr stent was similar to that of ^{32}P (calculated through analytical fit by Prestwich in a previous study), particularly with regard to the end-point beta energies, although the dose fall off of ^{142}Pr was just a little greater than that of ^{32}P (the end-point beta energy (E_{max} = 2.16 MeV) is high enough for therapeutic uses). These results indicate that ^{142}Pr could serve as an alternative beta brachytherapy source that could meet short half-life and cell proliferation rate requirements. It also has potential uses as an ophthalmic applicator, as its dose profile is comparable to that of ^{90}Sr/^{90}Y, the ophthalmic applicators currently in use.

^{142}Pr can easily be obtained by irradiation in a low-fluence reactor in a relatively short time, because of its high thermal neutron cross section (11.4 barn) that is significantly higher than a typical beta source such as ^{32}P (0.18 barn). In addition, ^{142}Pr is not a bone-seeker such as ^{90}Sr/^{90}Y.

Furthermore, praseodymium can be mixed as a glass type with other inorganic materials to achieve a high ratio (up to around 80$^{w}/_{o}$) that eases the difficulties of source fabrication. This high enrichment capability facilitates clinical applications such as radioactive microspheres for the treatment of hepatic tumors and AVM treatment.

CHAPTER V

DOSE BACKSCATTER FACTOR CALCULATION FOR SELECTED BETA SOURCES

V-1. Introduction

Brachytherapy methods are being used more frequently to treat arterial diseases and in recent applications of radioisotopes to treat tumors. Specifically, use of beta emitters in the treatment of arterial disease is now preferred over gamma emitters both because it reduces the dose to the medical staff and because the short range of beta particles results in the less radiation exposure to peripheral healthy tissue around the thin arterial wall. The radioisotopes ^{32}P and ^{90}Sr/^{90}Y have been extensively studied for these applications. However, other isotopes may hold promise for future applications in intravascular brachytherapy. Of these, the beta emitters ^{45}Ca, ^{142}Pr, and ^{185}W were selected for backscatter calculations in this study because the high beta yield makes the gamma contribution to dose negligible.

However, few of these isotopes can be injected directly into the tumor site. For example, ^{32}P and ^{90}Sr/^{90}Y are generally used in solution in a thin-walled container for angioplasty and ^{142}Pr must be mixed or encased with other materials because the element decomposes on contact with blood. Likewise, support materials are needed for a liquid source used in angioplasty and this can affect the dosimetry. If the support materials or the encased source materials have high atomic number (Z) compared with tissue, there could be significant electron backscattering effects in the vicinity of the tissue/source boundary. While not always detrimental (some researchers have attempted to use this effect in external electron therapy to increase the dose to tumor cells (Das *et al.* 1995)), for precise dose planning this backscattering effect must be taken into account. To study the effects of electron backscatter in beta brachytherapy, a variety of possible support or source matrix materials with Z numbers from 8 to 78 were chosen for each radioisotope.

Besides the effect of source fabrication materials, calcified plaque in the arterial wall can perturb dose, and contrast agents (used for imaging purposes during the source injection) were also considered as backscatter materials. Because contrast agents contain a considerable percentage of iodine (Z=53, see table V-1.), these materials are expected to contribute to the backscatter effect. Contrast agents are typically present for only a small part of a procedure; occasionally however, they are used to inflate angioplasty balloons, and are therefore present during the entire procedure. In these cases they can be a significant factor in dose perturbation (Li 2001).

There have been many studies on beta-particle backscatter, and Z-dependent formulae predicting backscatter effects differ from author to author (Sharma *et al.* 1980, Baily 1980, Chibani 2001, Pandey *et al.* 1989, Nunes *et al.* 1993a, Bafandeh 1992). Cho (1997) observed that the data indicating that electron backscattering is dependent on the energy of the primary electron is inconsistent due to different experimental settings and the limited spatial resolution of the detectors. Although the backscatter factor can vary for different source geometries, the values obtained for a point source, analytically fit, can be generally applied to the DPK method used in

Table V-1. Composition of calcified plaque and contrast agents (Nath *et al.* 2001)

Elements	*Calcified plaque*	*Hypaque*	*Omnipaque*
(Atomic No.)	Composition (%)		
H (1)	3.10	7.42	6.90
C (6)	31.26	7.88	14.96
N (7)	0.99	1.67	2.76
O (8)	37.57	58.92	50.49
Na (11)	-	1.38	-
Cl (17)	0.05	-	-
Ca (20)	27.03	-	-
I (53)	-	22.73	24.89

Chapter IV for the more complex geometries through iteration of integration for volume sources. The beta backscatter factor, one of the most prominent secondary effects, should be properly incorporated into DPK precise dose planning where the interface exists between large Z number media.

Electron backscattering of ^{32}P and ^{90}Sr/^{90}Y beta emitters has been extensively studied through both calculation and experiment, but except these radioisotopes, the backscattering study usually addressed only mono-energetic beams and various difficulties that can occur in the lower energies of the beta spectrum during experiments. The values obtained for mono-energetic beams are difficult to apply to beta emitters because of differences in the spectrum of energies emitted.

To use mono-energetic data, one must obtain the beta energy spectra of the source; in this study SADDE MOD2 (Reece *et al.* 1989) code was used to obtain this data. Through the SADDE MOD2, the beta spectra was computed and divided into 150 discrete energy bins, and these bins were normalized to unity and incorporated into the MCNP input. Using MCNP, the dose backscatter factor was calculated for a point source on the interface between two different media. This enhanced dose was compared to the dose in a homogeneous media (e.g., water) and the backscatter factor calculated.

V-2. Materials and methods

Backscatter factors for the beta emitters were calculated using MCNP 4C Monte Carlo code (Briesmeister 2000). The MCNP is a general-purpose particle transport code that can simulates three major particles, i.e. neutrons, gammas and electrons. For electron transport, bremsstrahlung production and knock-on electrons can be incorporated to the final result. In order to make the results fit within the desired error range (< 10 %), one million histories were used per MCNP run. However, due to lower average energy of ^{45}Ca and ^{185}W (see table V-2), 3 or 5 million histories were necessary depending on the error range. The beta emitter was assumed to be a dimensionless point source emitting its characteristic beta energy spectrum. The spectrum was generated using 150 discrete energy bins through SADDE MOD2. Input to the SADDE code included: the decay mode, the atomic number of the transition product nucleus, the atomic mass of the decaying isotope, the endpoint energy of the specific decay path, and the degree to which the transition is forbidden. The spectra of ^{90}Sr and ^{90}Y were combined because they are in secular equilibrium and the combination of these two isotopes is sometimes preferred for practical reasons, including the high activity of ^{90}Y and the long half-life of ^{90}Sr (Fox 2002). All the following calculations utilize their combined spectra.

The geometry used in this backscatter factor calculation was taken from Cho and Reece (1999), which was initially adapted from Nunes *et al.* (1993a, 1993b). The difference between Cho and Reece's work and this study is that they used the EGS4 Monte Carlo code, and their calculations were for monoenergetic point sources and a ^{32}P point source. Although they calculated factors for five electron energies (0.1, 0.5, 1.0, 2.0 and 3.0 MeV) to cover typical beta spectra, and they proposed interpolation fit to predict backscatter factors for different materials, questions still remain about direct application of these data to beta brachytherapy seeds, which have a broad range of spectra and a unique shape. Therefore, using individual spectral data provides more

Table V-2. Radioisotopes used in this study.[a]

Radioisotope	*Emission*	*Maximum energy (keV)*	*Average energy (keV)*	*Half-life*
^{32}P	Beta	1710	695	14.28 days
^{90}Sr	beta, low yield gamma	546	196	28.5 years
^{90}Y	beta, low yield gamma	2282	934	2.671 days
^{45}Ca	Beta	256	77	163.8 days
^{142}Pr	beta, low yield gamma	2160	810	19.12 hours
^{185}W	Beta	433	127	75.1 days

[a]. All data from http://t2.lanl.gov and rounded to significant digits.

accurate results when calculating backscatter factors for a brachytherapy seed. The simulated geometries as well as geometries used in the definition of backscatter factor are shown in figure V-1. (a). The dose backscatter factor is given by

$$B(r) = \left\{ \frac{D_s(r)}{D_w(r)} - 1 \right\} \times 100 \qquad (5\text{-}1)$$

where B is dose backscatter factor in percentage and r is the distance from the interface. D_s and D_w represent backscatter dose enhancement or decrement (usually enhancement) by the scatterer, with and without scattering effects, respectively. From this definition, the dose backscatter factor is calculated using the ratio of doses between the two media.

When simulating radiation transport using MCNP, the dose collecting detectors were constructed as a series of cylinders with the dimensions shown in figure V-1. (b). The backscatter materials were assigned to the lower volume as a scatterer and the detectors were located in the water media at various distances from the interface. The backscatter materials were chosen depending on each source's characteristics, and their Z numbers varied from 8 to 78. Contrast agents used as scatterers in this study were Hypaque and Omnipaque. The density of Hypaque is 1.32 g/cm^3, and Omnipaque's density is 1.406 g/cm^3. Calcified plaque on the arterial wall can also be considered a scatterer; the density of this material was assumed to be 1.84 g/cm^3. All these data were obtained from Nath *et al.* (1999a), and composition of these materials is listed in table V-1. Nath *et al.* (2001) calculated the photon perturbation effect as well as the shielding effect for selected photons (^{125}I, ^{192}Ir and ^{103}Pd) and beta emitters (^{90}Y, ^{32}P and ^{188}Re).

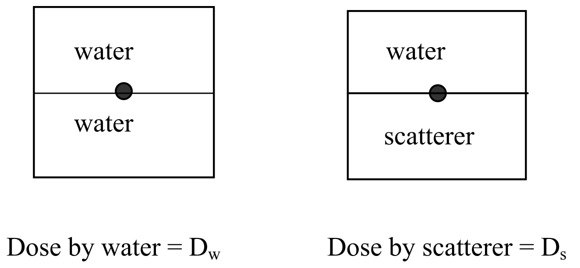

(a) Schematic for the definition of the dose backscatter factor

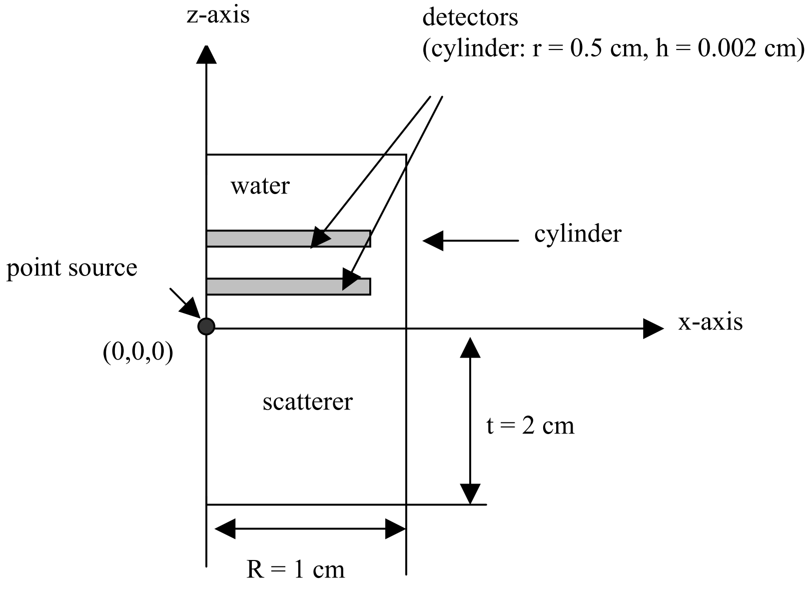

(b) MCNP input geometry for dose backscatter factor (half the geometry along z-axis shown here, not to scale)

Figure V-1. Schematic drawings of backscatter factor calculation setup

For the ^{142}Pr source, the elements aluminum, silicon, oxygen, praseodymium were used. The composition ratio of the Pr source material was 10.5$^{a}/_{o}$ praseodymium, 63.2$^{a}/_{o}$ oxygen, 10.5$^{a}/_{o}$ aluminum, and 15.8$^{a}/_{o}$ silicon. The density of this material was assumed to be 3 g/cm^3. These source-matrix materials are currently under investigation for use in the application of ^{142}Pr. The backscattering effect for the ^{142}Pr source material (Pr, O, Al and Si; scatterer) interacting with calcified plaque (absorber) was calculated. The same calculations were made for the source material (scatterer) used with Hypaque (absorber), and the source material (scatterer) was also used with Omnipaque (absorber).

The beta spectra used in the calculations were obtained using SADDE MOD2 as described above, and the end point energies of the sources used are listed in table V-2. However, some discrepancy exists between the average energy listed in the table V-2 and the actual average used in the calculation. This discrepancy arises because of the use of energy bins for MCNP input. However, the discrepancies between listed and used values do not exceed 30 keV in any case.

V-3. Results

V-3-1. Trend of backscattering effect

As expected, the backscatter effect was more significant in the immediate vicinity of the interface between the two media (see figures V-2~V-12). All the plotted data shown in the figures has an error less than 10%, as calculated by the embedded statistical check in MCNP code. For most of the beta emitters, maximum backscatter factors were observed at 0.1 cm or less from the interface. Bafandeh (1992) stated that the saturation of the backscatter effect occurs at about 1/5 of the maximum range of the particles in the material. Generally, the higher the Z number of scatterer, the higher the backscatter factor observed.

The dose backscatter factor for ^{32}P in the platinum medium (Z=78) reached more than 48% around 0.09 cm and dropped thereafter as shown in figure V-2. At the other extreme, the maximum backscattering factor was less than 3.4% at 0.051 cm for ^{32}P in the oxygen medium (Z=8). The result for the aluminum scatterer closely matched with Cho and Reece (1999) calculated with EGS4; the comparison of these results will be discussed in a later section (V-3-3). With regard to contrast agents, significant backscatter factors (more than 30%) were observed for both Hypaque and Omnipaque (see figure V-3). This suggests that contrast agents will affect dose because of the iodine content. Calcified plaque generated a 10% to 12% backscatter factor at distance between 0.007 cm and 0.1 cm. In order to confirm these results into a more realistic clinical situation, contrast agents and calcified plaque 0.1 cm thick were used as scatterers in identical geometry assemblies. In this situation the scattering surface was sandwiched between 4 cm high water cylinders. This geometry is essentially the same as the geometry depicted in figure V-1, except for the thickness of the scattering agent. The results of these trials will be compared with the results generated by normal geometry (as in figure V-1) in section V-3-4. However, these results assume that the contrast agents filled 100% of composition of the blood vessel; in clinical situation, the layer of contrast agent would be thinner.

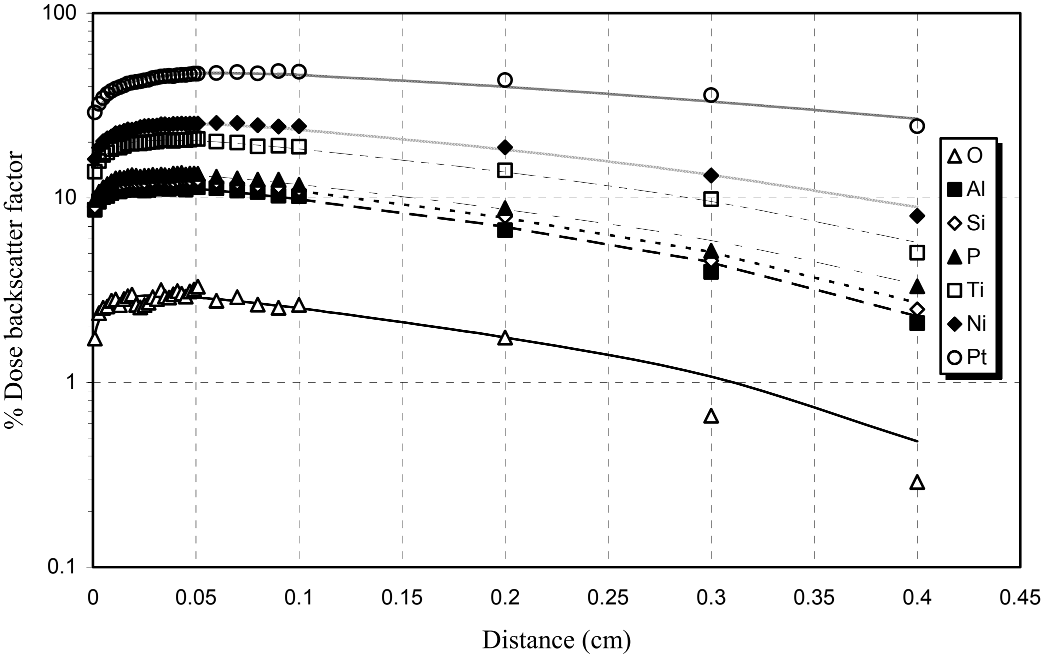

Figure V-2. Dose backscatter profile of ^{32}P for different scatterer (analytical fits shown as lines hereafter)

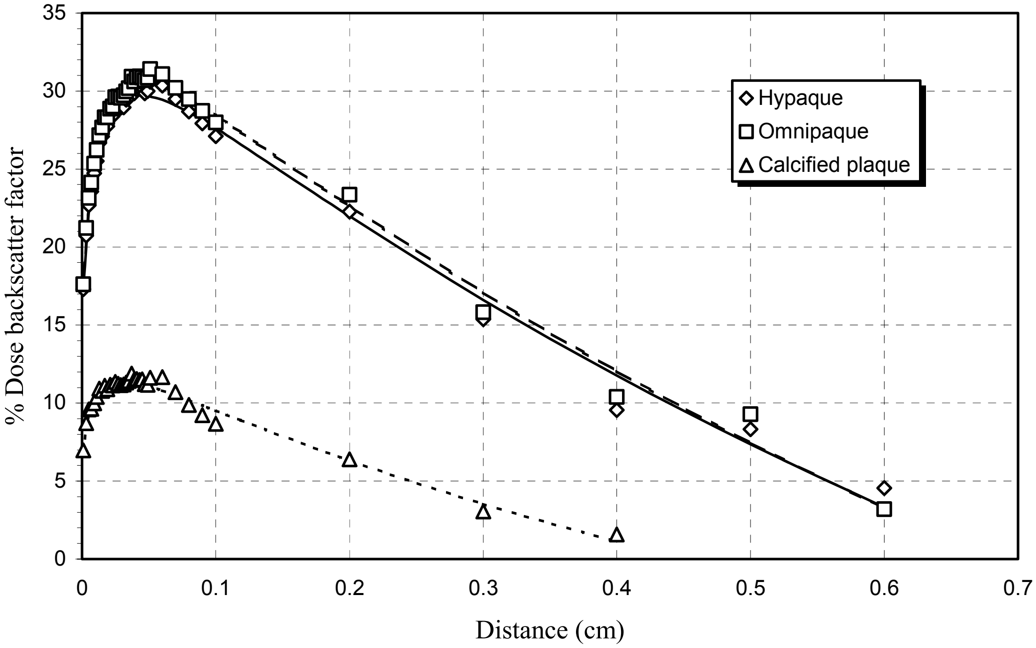

Figure V-3. Dose backscatter profile of ^{32}P for calcified plaque and contrast agents

As shown in figures V-4 and V-5, backscatter profile of ^{90}Sr/^{90}Y was very similar to that of ^{32}P, due to their similar average energies.

It was more difficult to characterize the backscatter profile of ^{45}Ca (average energy 77 keV) compared with other, higher, beta energy sources. As shown in figure V-6, backscatter profiles for high Z materials are much more like other high-energy beta emitters than the profiles from low-Z materials such as oxygen. Although more particle histories (3 million or 5 million) were used for these calculations, only data up to 0.045 cm was obtainable because of the weak penetrating power of ^{45}Ca beta particles (see figures V-6 and V-7). Inspection of figure V-6 shows larger fluctuations in the backscatter for low Z scatterers beginning around 0.025 cm. Similar fluctuations are visible in calcified plaque, which is also composed of low Z material. This phenomenon has been observed and documented by Nunes *et al.* (1993b). In their studies they observed unusually large backscatter between 300 to 400 mg/cm^2 in Mylar scatterer for a ^{32}P source, but could not achieve any clear proof of this phenomenon.

In order to observe whether differences in the detector thickness influenced this result because of the short CSDA (continuous slowing down approximation) range of low energy beta emitters, 1 μm thick detectors and 10 million histories were used instead of 0.002 cm thick detectors and 3 million histories. In another change, ITS 3.0 algorithm was used instead of the inherent MCNP algorithm. As stated in section II-4-7, the MCNP inherent energy uses cross section data from where the group of the electrons started, and ITS's algorithm uses data from the closest energy group. This makes the MCNP inherent algorithm result somewhat higher than that of ITS. Despite

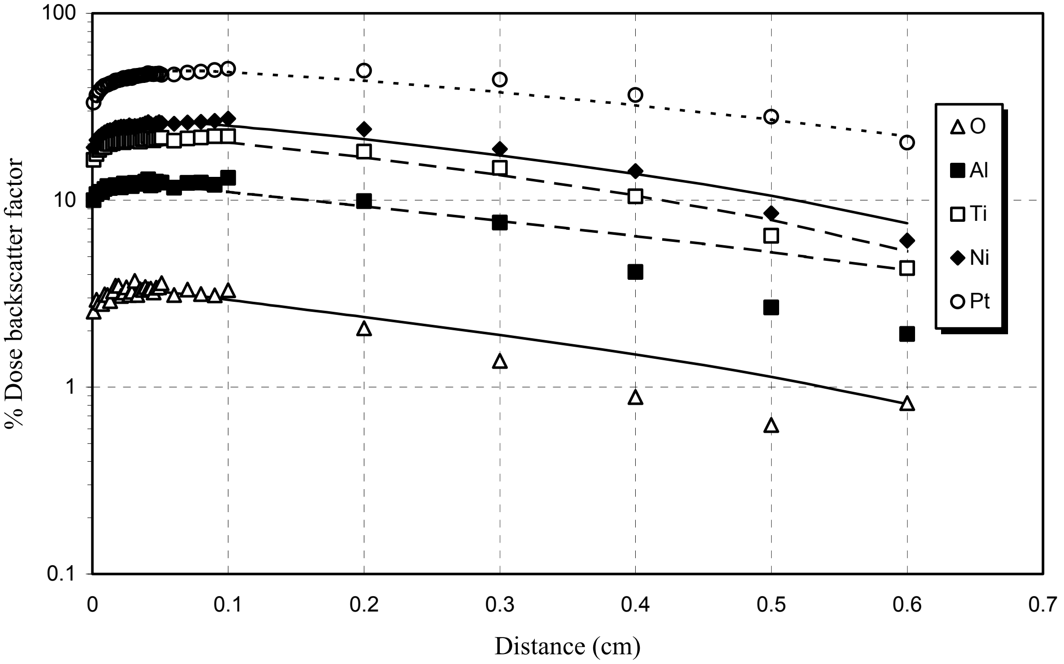

Figure V-4. Dose backscatter profile of ^{90}Sr/^{90}Y for different scatterers

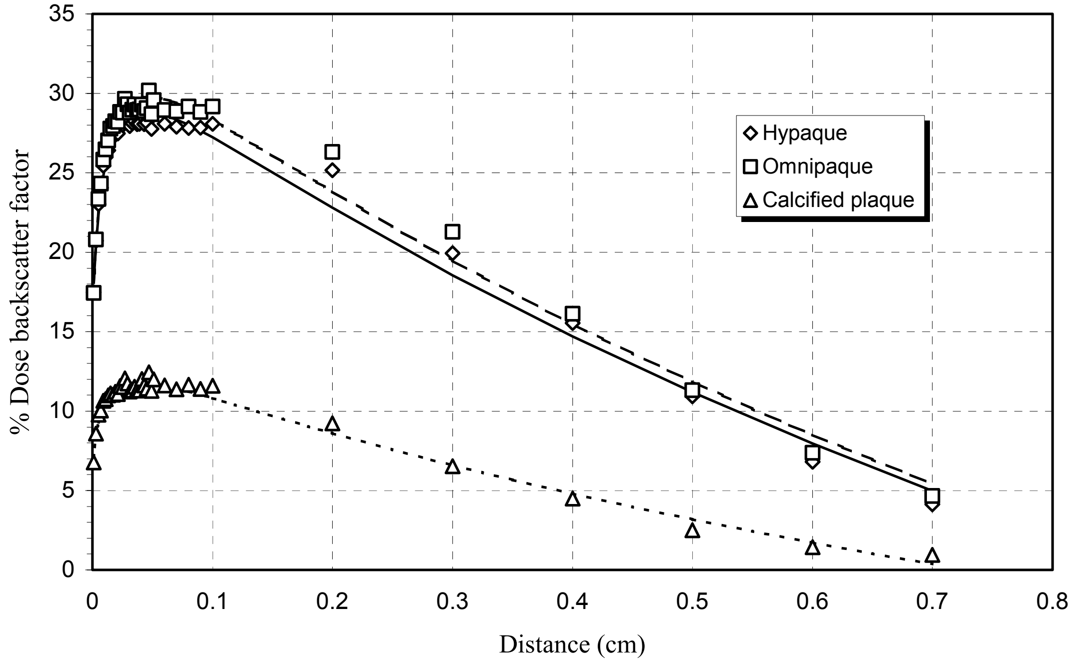

Figure V-5. Dose backscatter profile of ^{90}Sr/^{90}Y for calcified plaque and contrast agents

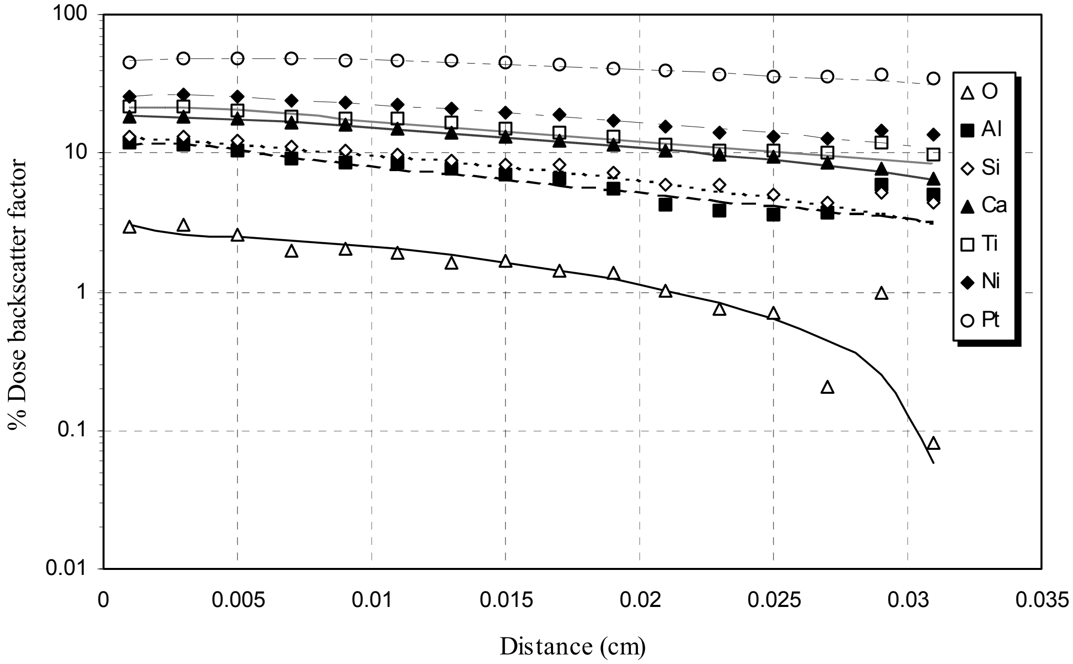

Figure V-6. Dose backscatter profile of ^{45}Ca for different scatterers

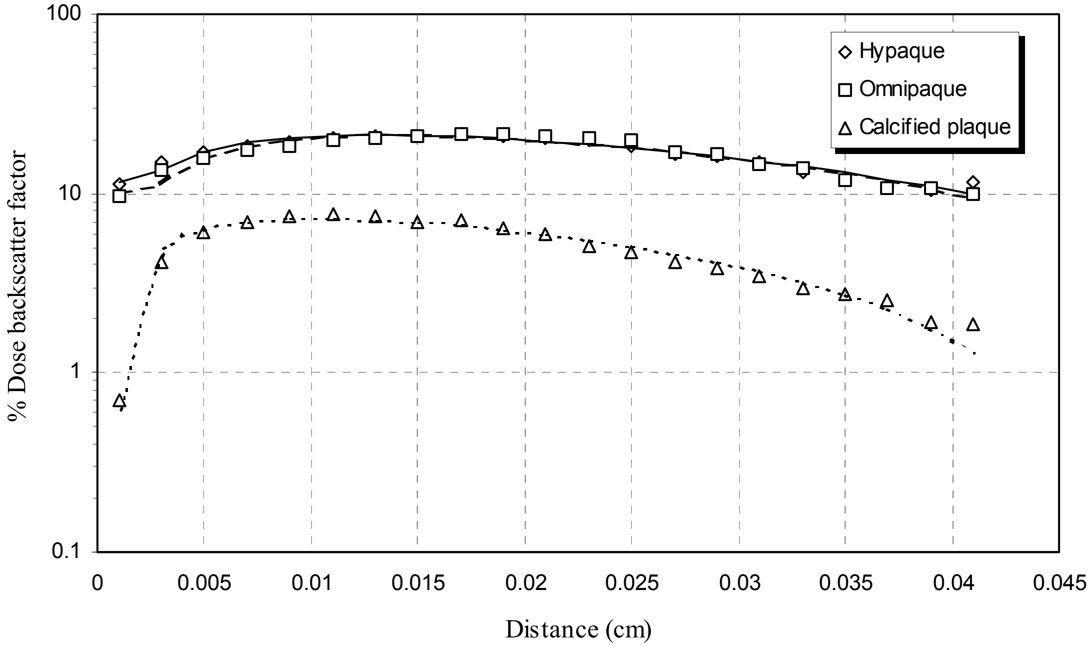

Figure V-7. Dose backscatter profile of ^{45}Ca for calcified plaque and contrast agents the using much smaller detector and different algorithm, fluctuation of dose backscatter factor increased in the tail area of the plot, as shown in figure V-8. These results indicate that the abrupt increase and decrease is not dependent on detector thickness. It also suggests that one should be cautious in the calculation and experimental determination of backscatter factors for low energy beta emitter in low Z scatterers. Perhaps this effect may due to the statistical fluctuation of MCNP which is prominent at lower beta energy. Since no conclusions can be drawn at present, further study is recommended. However, this fluctuation may not be an important phenomenon in clinical situations because the fluctuation range is near the end of, and even beyond, the X_{90} distance of ^{45}Ca (0.0216 cm in water).

Therefore, dose backscatter beyond this range is composed of secondary particles whose energies are much lower than the primary beta energy. The highest backscattering occurred around 0.003 to 0.005 cm much nearer to the source than any other isotopes because of the short beta range of ^{45}Ca.

For ^{142}Pr, only the four elements previously mentioned above and their compound material were used as a scatterer. The result of water to scattering materials composing ^{142}Pr seed is shown in figure V-9. The compound materials of microsphere for AVM treatment used in the animal tests were O, Al, Si and Pr. In the figure, contribution by each of the material and the effect of mixed material of these elements is also shown. As expected, the higher the atomic numbers in the scatterer, the higher the dose backscatter factor obtained. Although the compound material was composed of only $10.5^{a}/_{o}$ of praseodymium, it showed higher dose backscatter profile than the praseodymium alone. Several other high Z materials were chosen and tested under

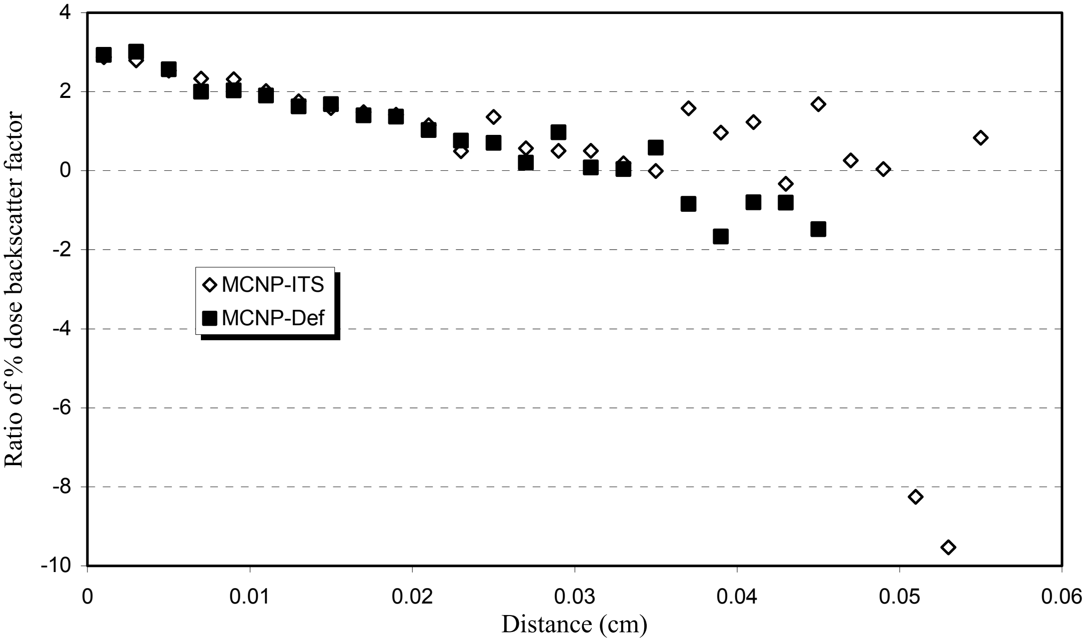

Figure V-8. Effect of the detector size and use of different data choosing algorithm (Note: MCNP-Def: 0.002 cm thickness and MCNP inherent energy grouping algorithm, MCNP-ITS: 1 μm thickness detector and ITS 3.0 algorithm)

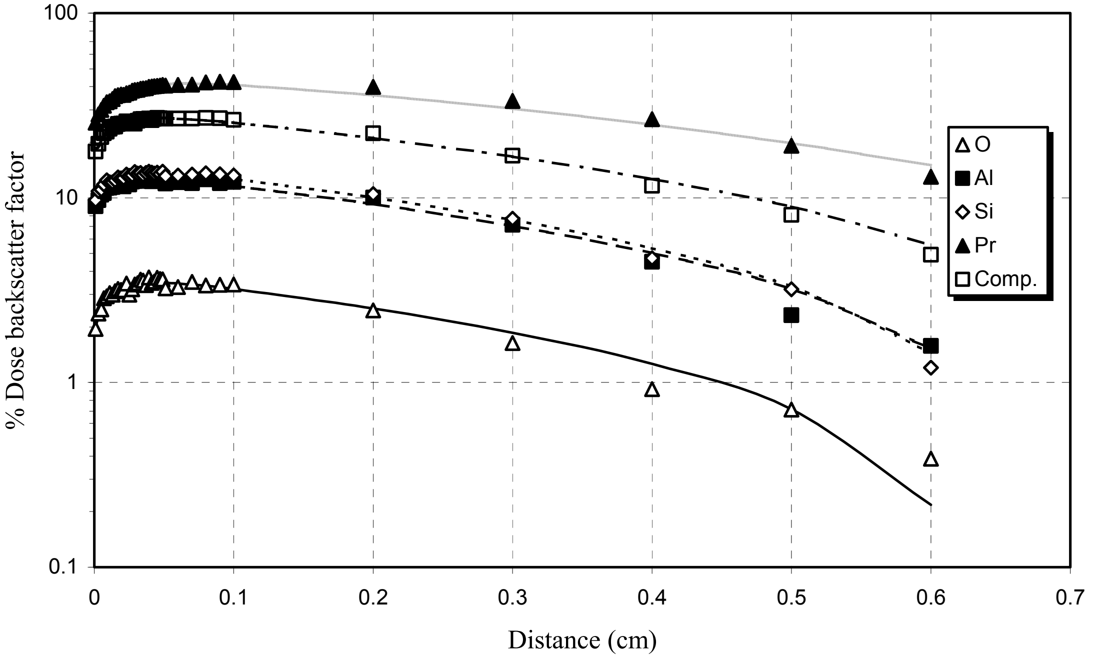

Figure V-9. Dose backscatter profile of ^{142}Pr for different scatterers (Note: Comp. represents composition material of Al, O, Si and Pr) same conditions, and it was verified that the high Z element dominates the backscatter effect even when it comprises a smaller portion of the compound than the low Z element. Backscatter factors for Hypaque and Omnipaque showed almost the same tendency, as illustrated in figure V-10.

The dose backscatter factor was calculated for arterial wall materials, such as calcified plaque, Hypaque and Omnipaque, against ^{142}Pr source compound material. In this case, the detector was located in the arterial wall material. As shown in figure V-11, dose backscatter factors were negative except for the calcified plaque, which showed a dose backscattering factor of 12-15%, most likely due to large differences between the Z numbers. These results are not surprising if we take into account the effective atomic numbers of these materials. It can be concluded, therefore, that if the source material has an effective atomic number similar to that of the contrast agent, the backscattering effect can be neglected.

As shown in figures V-12 and V-13, dose backscatter factor have been well characterized graphically, like backscattering profile of other beta emitters. Even though ^{185}W has low average energy (127 keV), it did not show any of the large fluctuations at greater distances typical of low Z material such as ^{45}Ca.

V-3-2. Analytical fit

The result presented in previous section can be adapted through analytical fit for each backscattering material and the equations given by (Cho and Reece 1999, Cross *et al.* 1992),

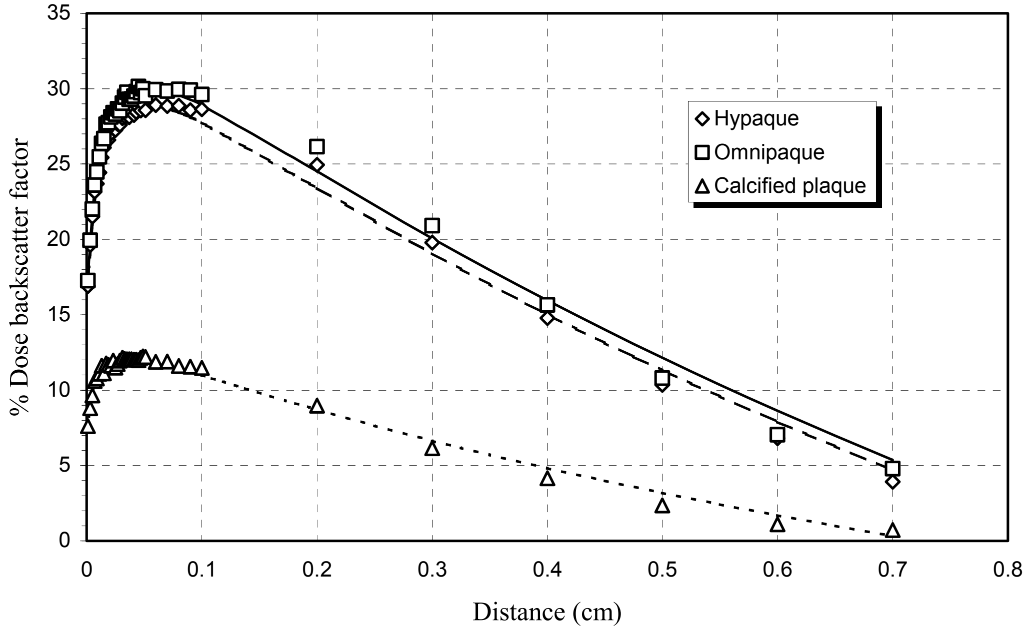

Figure V-10. Dose backscatter profile of ^{142}Pr for calcified plaque and contrast agents

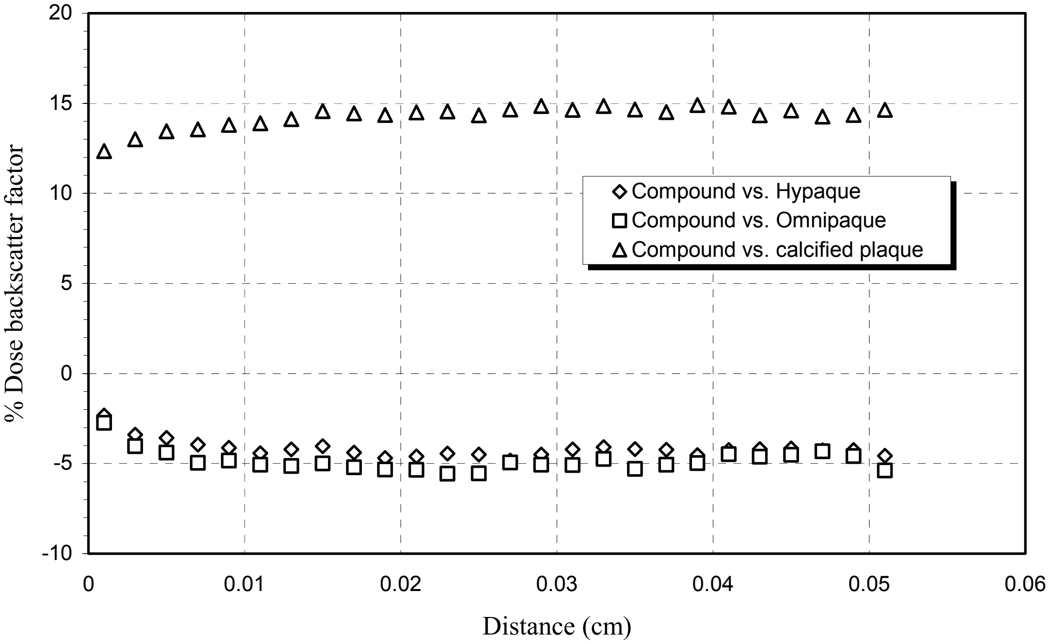

Figure V-11. Dose backscatter profiles of ^{142}Pr for compound material vs. calcified plaque and contrast agents

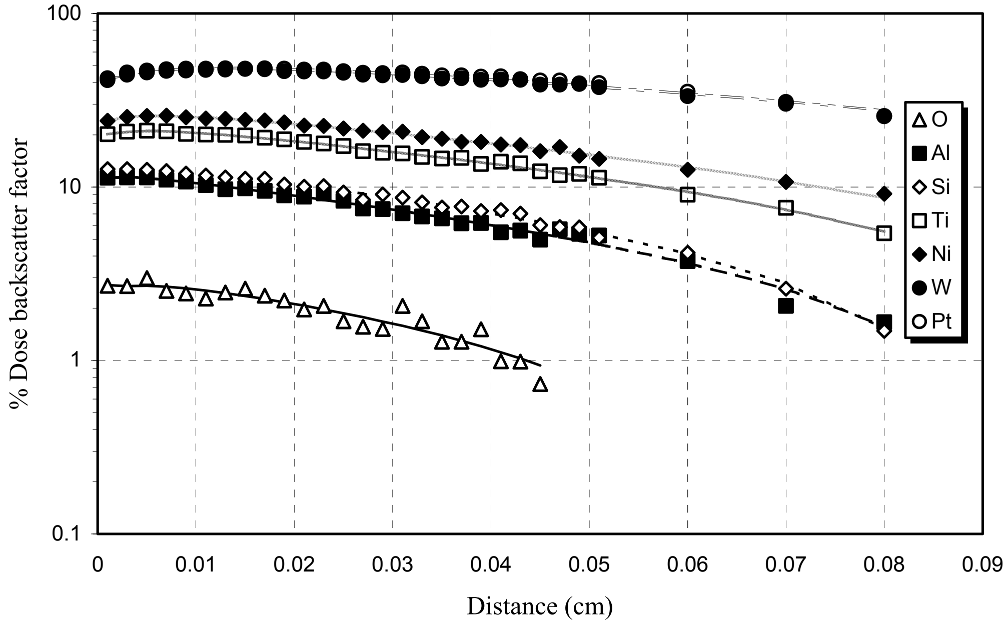

Figure V-12. Dose backscatter profile of ^{185}W for different scatterers

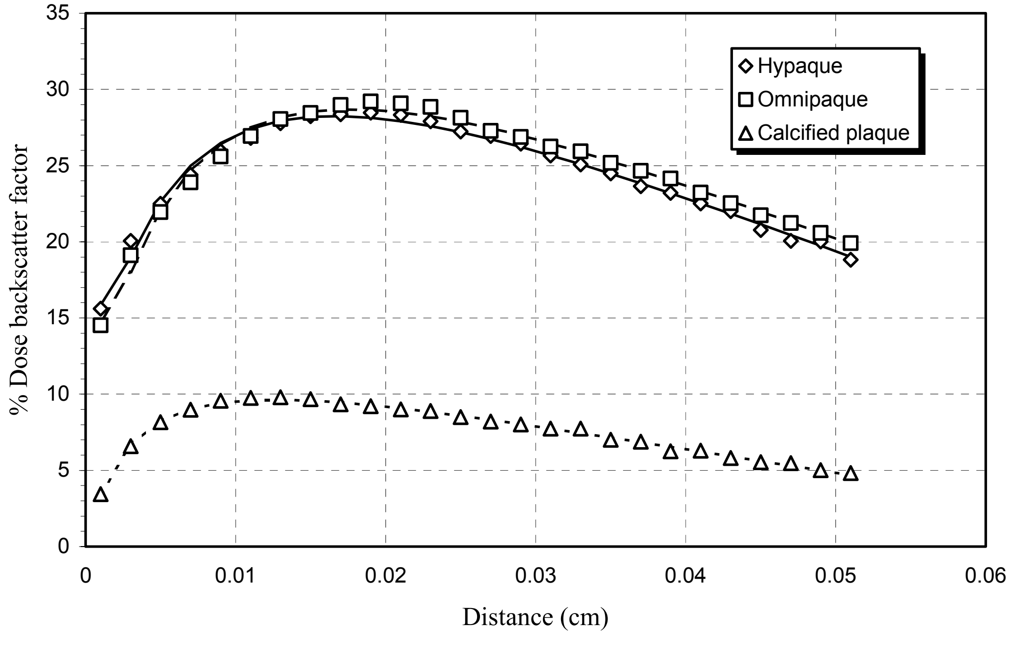

Figure V-13. Dose backscatter profile of ^{185}W for calcified plaque and contrast agents

$$B = m_0 + \sum_{i=1}^{3} m_i (\log_{10} r)^i \tag{5-2}$$

where B is the percentage dose backscatter factor and r is the distance from the interface in cm. The results are presented in tables V-3 to V-7.

As shown in table V-3, the fit for ^{32}P was excellent, with a generally high correlation coefficient R^2 (> 0.96), except for the oxygen medium ($R^2 = 0.93$) for distances up to 0.5 cm, for which it was slightly lower. However, a correlation coefficient of more than 0.95 was obtained when it was fitted to a distance of 0.019 cm for the oxygen scatterer.

The calculations for ^{90}Sr/^{90}Y, as listed in table V-4, showed excellent fit ($R^2 >$ 0.95) except for the oxygen medium ($R^2 \sim 0.93$). Also note that the data for the aluminum medium is only valid up to 0.7 cm, while others are valid though 0.9 cm.

In the case of ^{45}Ca (table V-5), calcium, tungsten and platinum showed high correlation coefficients. For low Z materials, such as aluminum and silicon, the correlation coefficients hardly exceeded 0.9 for any of the distances investigated in this study. For calcified plaque and contrast agents, acceptable correlation coefficients (> 0.90) were obtained for distances through 0.025 cm for normal geometry (contrast agents and calcified plaque 2 cm in depth). When the scatterers were only 1 mm thick, the correlation was improved (> 0.94). The use of more realistic geometries in this study generated more reliable data; however, dose backscatter factors for low energy (less than 100 keV) electrons using low Z scatterers should be investigated further to improve the correlation factor.

As shown in table V-6, all the correlation coefficients exceeded 0.96 for

Table V-3. Dose backscatter factor for ^{32}P with seed composing materials, calcified plaque and contrast agents[a]

Elements (Atomic No.)	m_0	m_1	m_2	m_3	R^2
O (8)	- 2.1159	- 7.9958	- 3.9196	-0.5643	0.93
Si (14)	- 7.8617	- 32.675	- 16.397	-2.4676	0.9918
P (15)	- 7.5161	- 33.844	- 17.138	-2.5978	0.9933
Ti (22)	- 11.305	- 53.216	- 27.784	-4.2976	0.9935
Ni (28)	- 11.403	- 63.89	- 34.618	-5.4903	0.9892
Pt (78)	- 4.2276	- 100.03	- 59.621	-10.055	0.962
Calcified plaque	- 7.302	- 30.615	- 15.35	-2.2886	0.9931
Hypaque	- 14.215	- 81.081	- 44.778	-7.1826	0.9884
Omnipaque	- 13.743	- 82.396	- 45.831	-7.3786	0.989
Calcified plaque*	- 9.543	- 32.734	- 15.97	-2.3018	0.9774
Hypaque*	- 10.279	- 69.22	- 36.964	-5.6589	0.9905
Omnipaque*	- 10.927	- 72.29	- 38.922	-6.0126	0.9916

[a] Valid distance: 0 - 0.5 cm

*Thickness of Hypaque, Omnipaque and calcified plaque is 1 mm, valid distance is up to 0.6 cm for Hypaque and Omnipaque, 0.4 cm for calcified plaque

Table V-4. Dose backscatter factor for ^{90}Sr/^{90}Y with seed composing materials, calcified plaque and contrast agents[a]

Elements (Atomic No.)	m_0	m_1	m_2	m_3	R^2
O (8)	- 0.2437	- 5.27	- 2.4011	-0.3132	0.9275
Al (13)[b]	- 3.8143	- 28.106	- 15.219	-2.4805	0.9766
Ti (22)	- 3.2766	- 43.964	- 24.256	-3.9594	0.9867
Ni (28)	- 2.7812	- 52.952	- 30.114	-5.0122	0.9808
Pt (78)	+ 4.6575	- 90.115	- 55.9	-9.8036	0.9555
Calcified plaque	- 2.2409	- 24.677	- 12.662	-1.8352	0.9824
Hypaque	- 3.0572	- 62.237	- 34.531	-5.4465	0.9894
Omnipaque	- 2.4976	- 63.612	- 35.737	-5.6722	0.9917
Calcified plaque*	- 3.2042	- 24.892	- 12.736	-1.8593	0.9842
Hypaque*	- 2.8861	- 55.24	- 29.62	-4.5127	0.9871
Omnipaque*	- 2.7714	- 57.575	- 31.289	-4.805	0.9861

[a] Valid distance: 0 - 0.9 cm, [b] Valid distance: 0 –0.7 cm

*Thickness of Hypaque, Omnipaque and calcified plaque is 1 mm, Valid distance is up to 0.7 cm

Table V-5. Dose backscatter factor for ^{45}Ca with seed composing materials, calcified plaque and contrast agents[a]

Elements (*Atomic No.*)	m_0	m_1	m_2	m_3	R^2
O (8)	- 31.648	- 40.003	- 15.725	-2.0811	0.9228
Al (13)	- 2.5642	+ 8.5211	+ 12.028	+2.5357	0.7973
Si (14)[b]	- 70.615	- 86.3	- 30.233	-3.5971	0.8723
Ca (20)	- 102.03	- 129.41	- 46.452	-5.576	0.9975
Ni (28)	- 124.84	- 158.88	- 55.388	-6.3947	0.9379
W (74)	- 284.93	- 407.47	- 164.46	-21.769	0.9604
Pt (78)	- 262.79	- 375.81	- 149.13	-19.386	0.9523
Calcified plaque[c]	- 159.61	- 215.18	- 89.675	-11.951	0.944
Hypaque[c]	- 169.75	- 260.17	- 114.17	-15.942	0.9058
Omnipaque[c]	- 134.87	- 221.84	- 100.97	-14.45	0.9321
Calcified plaque*	- 95.098	- 129.07	- 52.022	-6.5446	0.982
Hypaque*	- 278.64	- 408.66	- 180.3	-25.441	0.958
Omnipaque*	- 298.73	- 442.09	- 197.63	-28.192	0.9433

[a] Valid distance: 0 - 0.045 cm, [b] Valid distance: 0 - 0.035 cm

[c] Valid distance: 0 - 0.025 cm

*Thickness of Hypaque, Omnipaque and calcified plaque is 1 mm, valid distance is up to 0.041 cm for calcified plaque and Omnipaque, 0.039 cm for Hypaque distances up to 0.7 cm, and can readily be applied to analytical calculation of ^{142}Pr. For ^{185}W, correlation coefficients were well above 0.96 except for the oxygen scatterer (see table V-7) even though its average energy was only 127 keV.

V-3-3. Comparison with other results

In order to check the validity of the spectrum generated by SADDE MOD2, the results were compared with previous studies (Nunes *et al.* 1993a, 1993b, Cho and Reece 1999) and which dealt with ^{32}P point source. Although Nunes *et al.*'s (1995) fit was obtained from aluminum/Mylar interface, the results agreed for areas in the vicinity of the interface (figure V-14). Cho and Reece's (1999) results much more closely matched those of the MCNP using the ITS 3.0 algorithm rather than the MCNP inherent algorithm (figure V-15). However, large discrepancies were observed at the 500 cm/mg^2 depth. This disagreement may have been caused by different physics models between MCNP and EGS4, or by different spectrum generating codes. Furthermore, when using Monte Carlo code (i.e. MCNP), choosing a different energy grouping method alone may make a significant difference (up to 14%, figure V-15). Usually, the MCNP inherent algorithm shows higher values than those of the ITS algorithm. The results from the MCNP calculation were generally higher than those from the EGS4 for any distances, as it was previously demonstrated by other studies (Wang *et al.* 1999).

Table V-6. Dose backscatter factor for ^{142}Pr with seed composing materials, calcified plaque and contrast agents.[a] Compound is composed of O, Al, Si and Pr

Elements (Atomic No.)	m_0	m_1	m_2	m_3	R^2
O (8)	-1.4600	-8.5427	-4.5698	-0.7013	0.9752
Al (13)	-4.1208	-28.8120	-15.5880	-2.4912	0.9882
Si (14)	-4.8365	-32.0370	-17.3180	-2.7664	0.9914
Pr (59)	-1.7400	-86.7840	-53.3330	-9.2250	0.9683
Compound	-6.029	-59.23	-32.954	-5.3099	0.9909
Calcified plaque[b]	-0.496	-22.466	-11.671	-1.7031	0.9764
Hypaque[b]	15.866	-32.501	-20.008	-3.1457	0.9960
Omnipaque[b]	10.069	-43.089	-25.423	-4.0062	0.9970
Calcified plaque*	- 3.261	- 25.021	- 12.592	-1.8171	0.9906
Hypaque*	- 3.7837	- 59.804	- 33.621	-5.3487	0.9937
Omnipaque*	- 3.3196	- 61.294	- 34.556	-5.4859	0.9924

[a.] Valid distance: 0 - 0.7 cm [b.] Valid distance: 0 - 0.051 cm
*Thickness of Hypaque, Omnipaque and calcified plaque is 1 mm,
Valid distance is up to 0.8 cm

Table V-7. Dose backscatter factor for ^{185}W with seed composing materials, calcified plaque and contrast agents[a]

Elements (Atomic No.)	m_0	m_1	m_2	m_3	R^2
O (8) [b]	- 14.98	- 20.998	- 8.2689	-1.0787	0.9036
Al (13)	- 33.344	- 48.39	- 17.349	-2.06	0.9878
Si (14)	- 46.432	- 68.982	- 26.84	-3.4722	0.9933
Ti (22)	- 65.941	- 103.05	- 40.174	-5.13	0.9945
Ni (28)	- 73.388	- 118.66	- 46.507	-5.9293	0.9943
W (74)	- 124.92	- 234.08	- 102.66	-14.387	0.9823
Pt (78)	- 136.24	- 254.32	- 113.01	-16.052	0.9696
Calcified plaque[c]	- 46.944	- 70.356	- 27.4	-3.2045	0.9652
Hypaque[c]	- 127.69	- 219.21	- 98.288	-13.781	0.985
Omnipaque[c]	- 144.21	- 247.98	- 113.23	-16.135	0.9732
Calcified plaque*	- 62.143	- 93.448	- 38.683	- 4.9385	0.9948
Hypaque*	- 167.3	- 275.97	- 124.95	-17.77	0.9897
Omnipaque*	- 175.05	- 291.11	- 133.24	-19.098	0.9878

[a] Valid distance: 0 - 0.08 cm, [b] Valid distance: 0 - 0.045 cm
*Thickness of Hypaque, Omnipaque and calcified plaque is 1 mm,
Valid distance is up to 0.051 cm

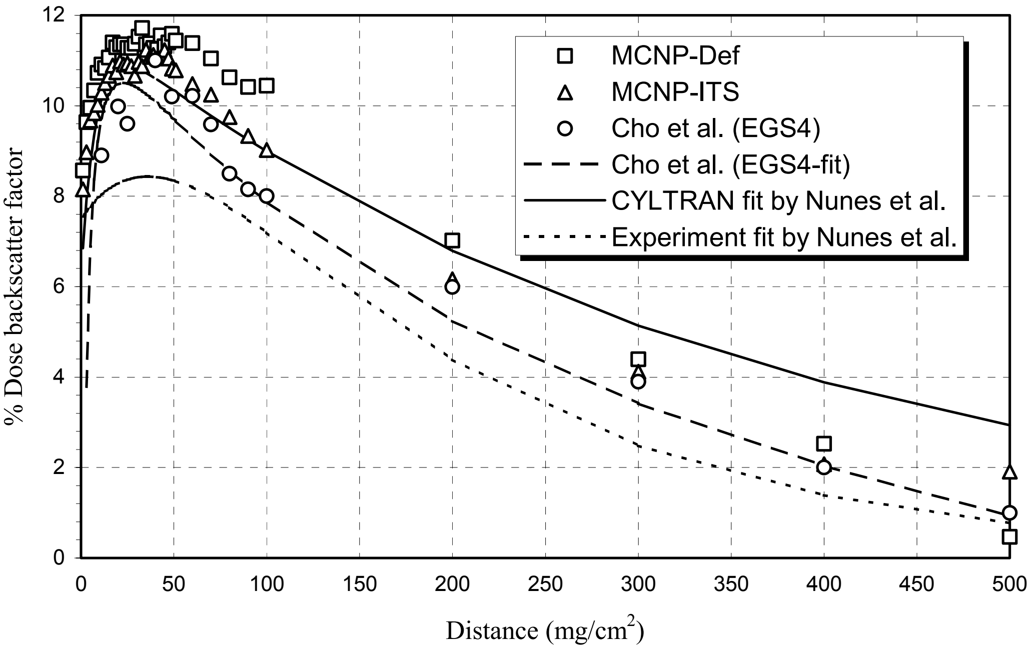

Figure V-14. Comparison of ^{32}P spectrum backscattering of water vs. aluminum with previous studies (Note: Nunes *et al.*'s experimental and CYLTRAN fits are for the Al/Mylar interface)

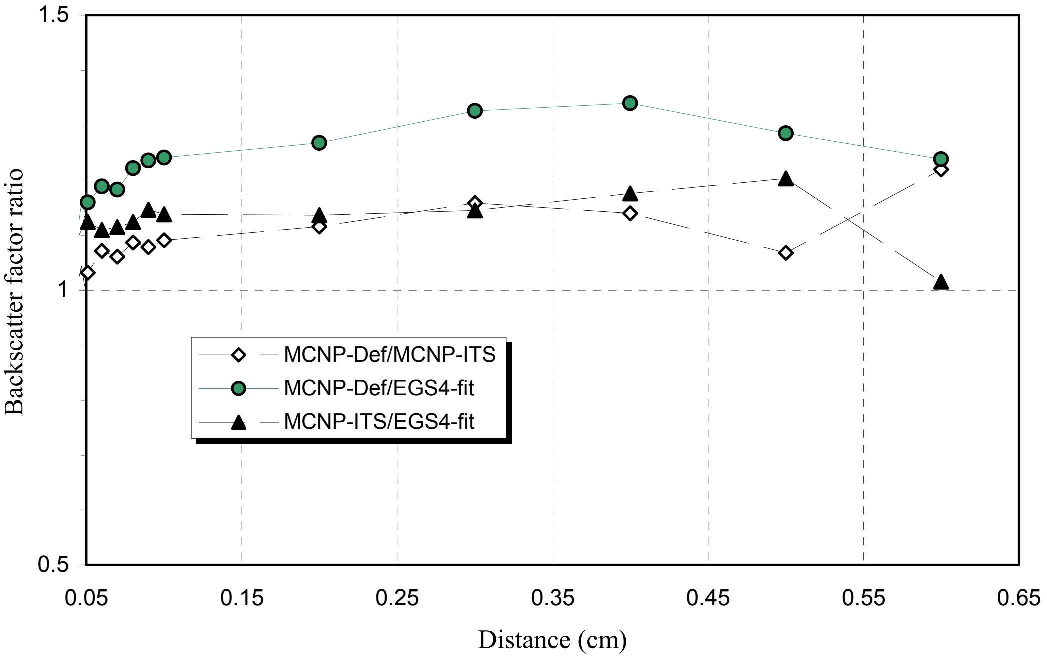

Figure V-15. Backscatter factor ratio for different Monte Carlo systems for ^{32}P in Al/Water interface

V-3-4. Thinner contrast agents and calcified plaque: a more realistic approach

In real physiological situations, contrast agents and calcified plaque cannot achieve the 2 cm thickness. In order to create realistic Monte Carlo simulation geometry based on the assumption that the contrast agents spread through the arterial wall, layers of contrast agents and calcified plaque with only 1 mm thick were used as scattering material. Significant differences were observed near the interface area when it was compared with 2 cm thickness. As shown in figure V-16 (a) through (e), in most of the cases, except ^{90}Sr/^{90}Y (see figure V-16 (b)), discrepancies were prominent near the interface, but decreased during the mid-range distances and increased again in the tail of the graph. The discrepancy was less than 10% in the mid-distance range. The values for these comparisons were all taken from analytical fit values. From these results, it is evident that the thickness of the materials composing the arterial wall was less effect on dose than expected, even when considering large differences in thickness. However, uncertainties regarding the dose backscattering effect of very small distances still exist, and should be taken into account in clinical work or further experimentation.

V-3-5. Log(Z+1) dependence

As Baily (1980) proposed, beta emissions were dependent on log (Z+1) even though this study was performed for energy spectra rather than mono-energetic sources. As shown in figure V-17, all the beta emitters corresponded well with high correlation factors ($R^2 > 0.99$) except for the ^{45}Ca spectrum (0.959) at a distance 0.011 cm from the interface. Although other formula have been suggested for broad energy

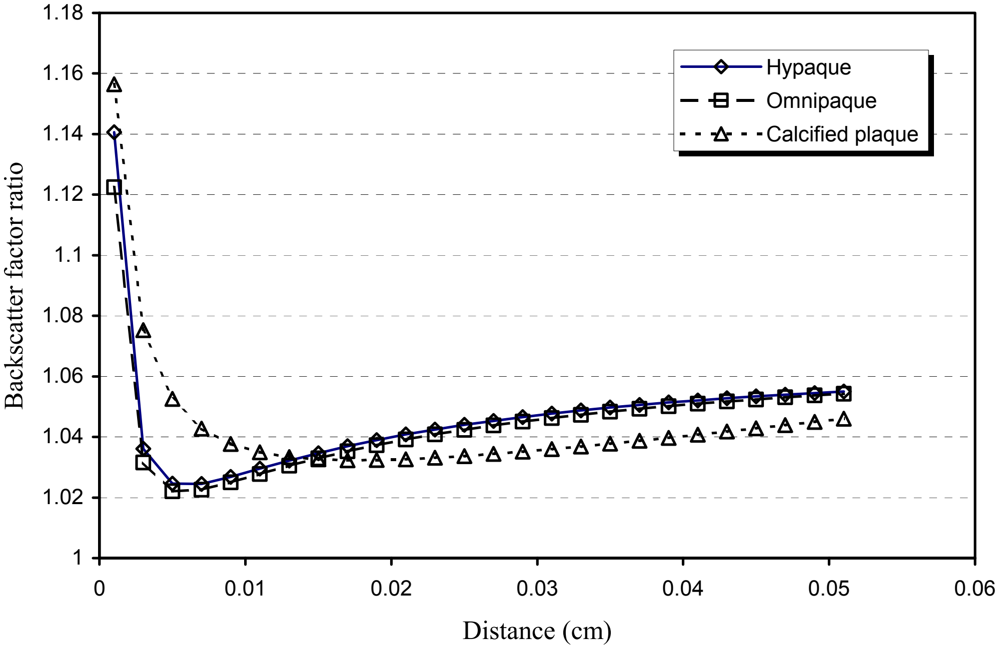

(a) ^{32}P

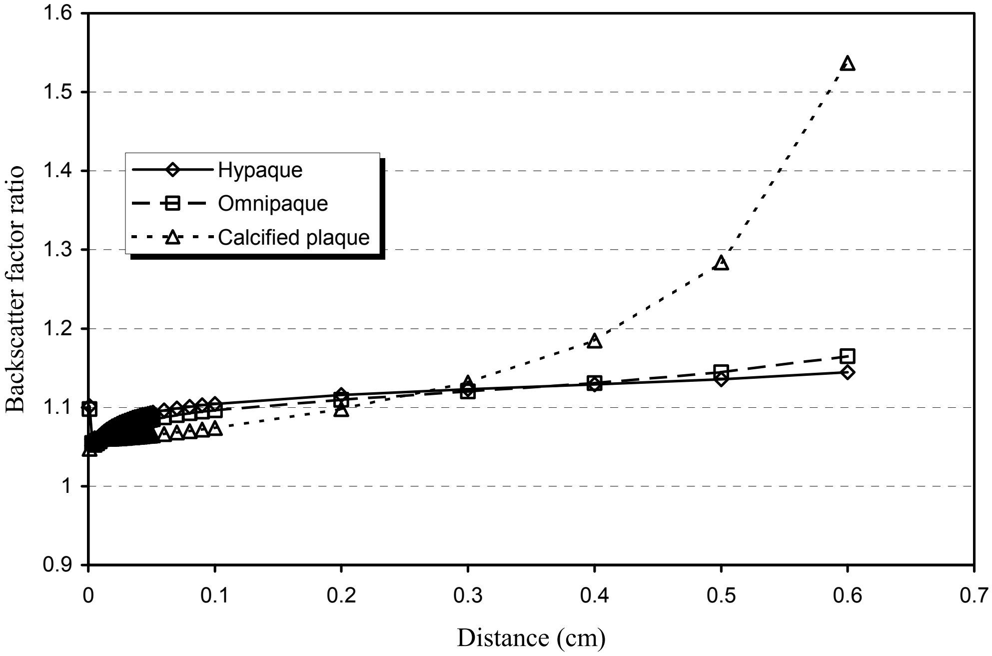

(b) ^{90}Sr/^{90}Y

Figure V-16. Backscatter factor ratio of 3 cm to 1 mm thick (3 cm/0.1 cm) contrast agents and calcified plaque

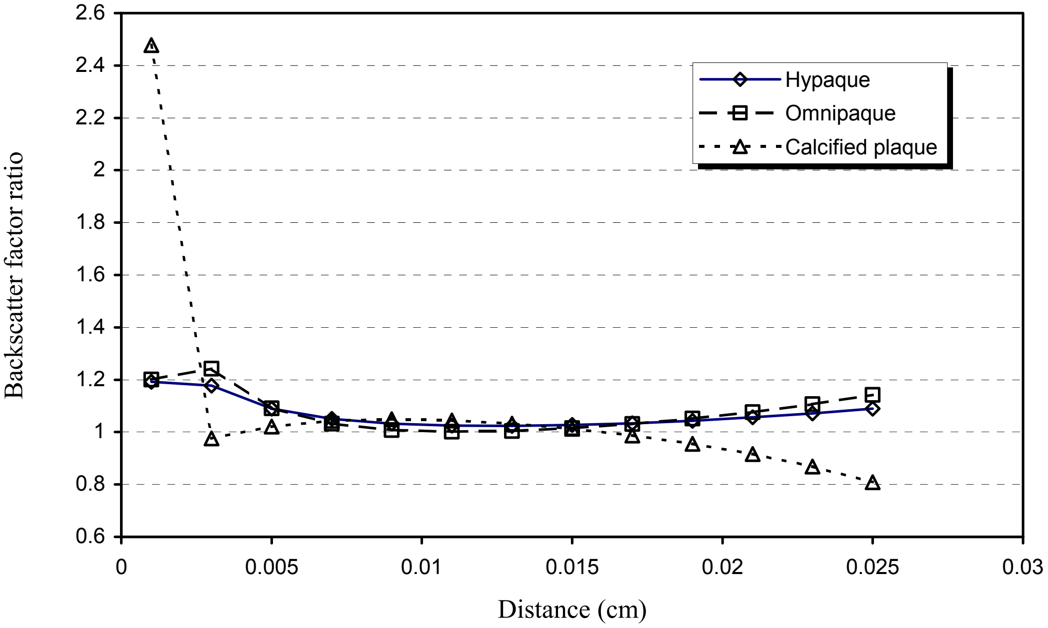

(c) ^{45}Ca

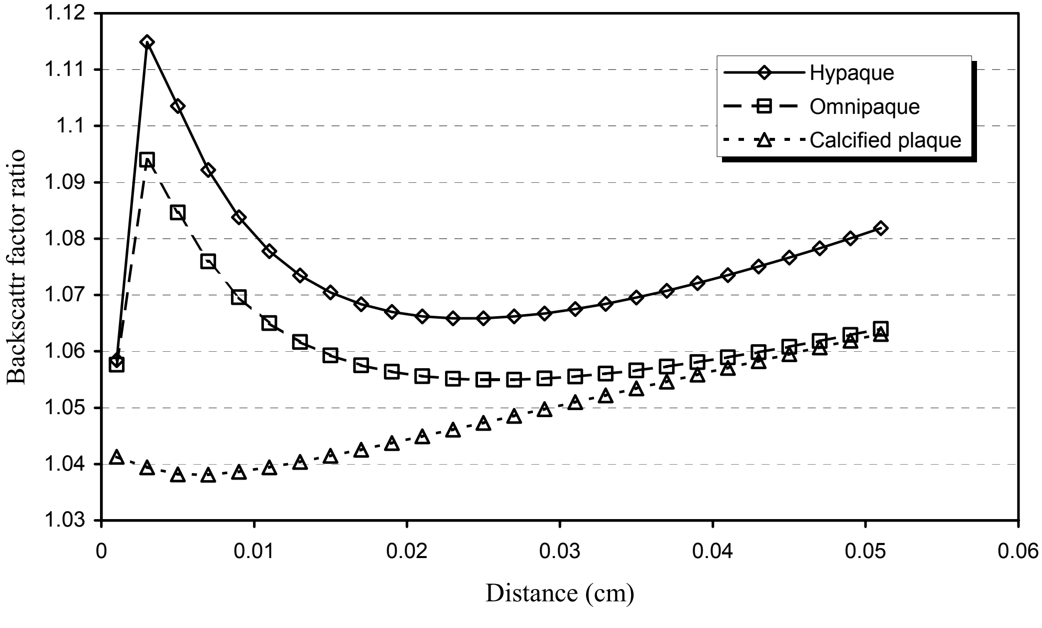

(d) ^{142}Pr

Figure V-16. Continued

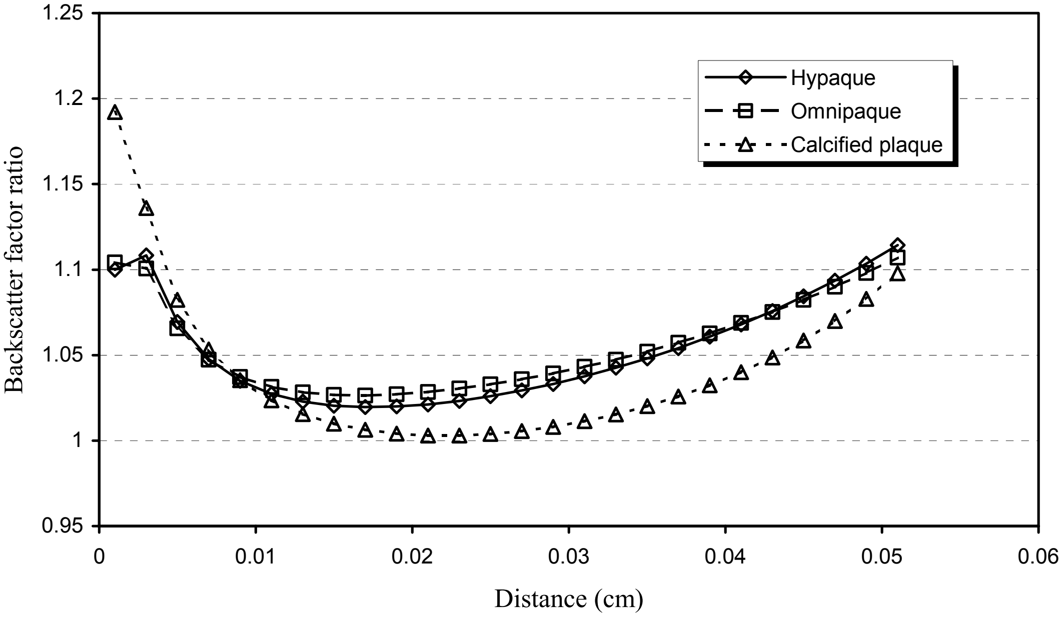

(e) ^{185}W

Figure V-16. Continued

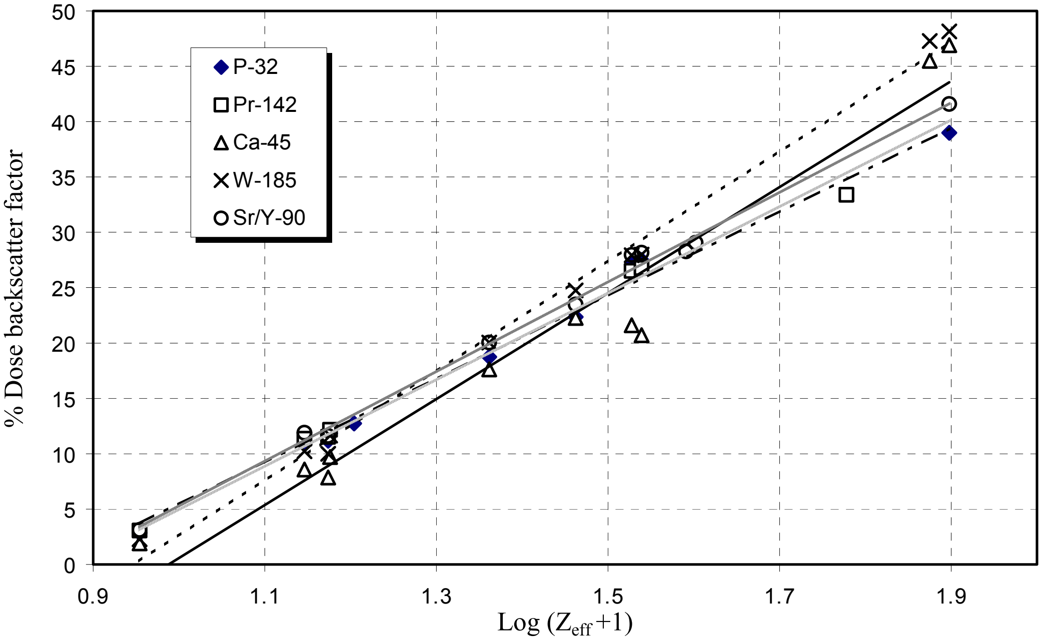

Figure V-17. Log (Z+1) dependence of dose backscatter factor at 0.011 cm distance application, such as {Electron Backscatter Factor = A - B·exp(-kZ)} (Klevenhagen 1991), log (Z+1) dependence was excellent expression for this study, which dealt with relatively low energy (less than 2.5 MeV end point energy) brachytherapy applications. For compound materials composed of calcified plaque, contrast agents and ^{142}Pr seeds, the effective atomic number (Z_{eff}) was needed. In order to obtain this, the following equation following was used.

$$Z_{eff} = \sqrt[m]{a_1 Z_1^m + a_2 Z_2^m + \ldots + a_n Z_n^m}\ , \tag{5-3}$$

where a_1 to a_n are the fractional numbers of electrons per gram contained in a compound of atomic number Z_1 to Z_n. The values of *m* that give the best fit range from 3.4 to 3.8, but the best fit was obtained by 3.5 (Johns *et al.* 1983). The value *m* varies with Z, with 3 for high Z and 3.8 for low Z material. However, the value of 3.5 for m used in this calculation was an excellent log(Z+1) dependence for the compound material. In order to calculate Z_{eff}, parameters from Attix (1986) were used. Z_{eff} obtained by eq. (5-3), and is tabulated in table V-8.

Table V-8. Effective atomic numbers of compound materials used in this study

	Calcified Plaque	*Hypaque*	*Omnipaque*	*^{142}Pr source matrix material*
Z_{eff}	13.93	32.69	33.62	29.84

V-4. Conclusions and discussions

The backscatter effects of selected radioisotopes were simulated through use of MCNP code. The backscatters were simulated using various materials that could be candidates for source composing or supporting materials as scattering agents. In addition to those materials, calcified plaque and contrast agents that could be present on the arterial wall during the procedure were used as scatterers. For intravascular brachytherapy, calcified plaque not only absorbs a fraction of the radiation dose to the endothelial cell of blood vessel but scatters the radiation back as well. This backscattering effect is diminished because source supporting material and calcified plaque also attenuate the dose to the target wall. However, since the diameter of a coronary vessel is usually smaller than 0.5 cm, impact of contrast agents may only be important for the target tissue in the few mm or even μm range. Also, contrast agents would spread widely into the arteries and could give different results because their compositions and densities are higher than tissue (estimated to be that of water in this study). As Nath *et al.* (1999b, 2001) already mentioned, the arteries will not be fully filled with these materials, so the backscatter factor calculated in this study will be somewhat higher than in a real situation. On the other hand, backscattering from contrast agents in beta source brachytherapy would affect the dose to the target cell significantly and is therefore important, even though the contrast agents are administered in a with saline solution and dispersed through the arterial wall.

In order to verify the validity of this study, results from previous studies that used ^{32}P emitters with aluminum scatterers (experimental) and water (EGS4 calculation based) were compared with these results. They correlated reasonably well;

specifically, the ITS 3.0 based MCNP showed a stronger correlation with the EGS4 calculation than the MCNP inherent algorithm.

This comprehensive data on backscatter factor can readily brought bear on future applications of the DPK method, or as an aid to future applications of new low-energy beta emitter sources, such as ^{45}Ca, ^{185}W and relatively high-energy ^{142}Pr, which up to this point have been relatively unexplored. For ^{45}Ca, analytical fits for low Z material shows less correlation in the form of third order polynomial fit, meaning that exact dose backscatter estimation could be difficult in clinical situations. Also, source matrix materials must be chosen carefully for ^{45}Ca because of its high solubility (in blood) and low energy, and significant self-absorption and perturbation in the source matrix material are to be expected. However, as long as high enrichment is an available option for ^{185}W, it can be used alone and the dose backscatter factor is very predictable, so this isotope may be a good candidate for future application to brachytherapy source.

The use of Z_{eff} for compound material was also validated the log(Z+1) correlation. For lower end point energies (^{45}Ca), however, the correlation was lower than other emitters, yet still acceptable ($R^2 > 0.95$).

CHAPTER VI

CONCLUSIONS, DISCUSSIONS AND FURTHER STUDY

The main purpose of this dissertation is to explore the dose profiles of ^{142}Pr in various seed types, dose variation as a formation of microspheres in artery, and dose backscatter factor calculation for some beta sources that can be considered for brachytherapy purposes as well as currently used sources.

Due to the rapid dose decrease around the beta source, it is extremely hard to obtain accurate data from experiments. Therefore, Monte Carlo calculation is widely used as an alternative method to analyze dose trends of radioactive seeds for therapeutic purposes. In this research, dose rate as a function of distance around the source was calculated using the MCNP code (Briesmeister 2000).

Beta dosimetry of microspheres in brain arteries was explored. The treatment methods of AVM can be determined by several factors such as size, location and radio-sensitivity of the nidus. Using these factors, AVM can be treated with surgery or radiosurgery. Sometimes, to enhance clinical result, both treatment methods are used together. However, if the location of nidus is hard to reach, stereotactic radiosurgery is solely used. Although during the stereotactic radiosurgery, some healthy tissues can be saved by exact dose planning with most up-to-date equipment and software, sacrifice of healthy tissues is inevitable. To protect the healthy tissues from unwanted side-effect from high-dose radiation, injection of microspheres into AVM feeding arteries was devised by Reece and Mawad (2001). ^{142}Pr was especially chosen as the material for this treatment because of high beta energy with a large thermal neutron cross section as well as low chemical toxicity.

Until now, beta dosimetry of microspheres was only performed in macroscopically (Campbell *et al.* 2000, 2001, Zavgorodni 1996). In their study, they assumed the microsphere source as a point source and ignores all the secondary effects such as inter-shielding between microspheres and bremsstrahlung effects by using DPK method.

In this study, beta dose calculation for ^{142}Pr microsphere was performed various source geometries filled with microspheres. The calculation was performed for cylinders packed with microspheres using random packing methods. Dose rate around the arterial wall was varied as a function of both size of arteries and microspheres. Combination of these two factors significantly affected the result. These results will aid in dose planning by selection of size of microspheres for a specific arterial size. However, questions still remain for the random close packing ratio (roughly around 50%) used in this calculation. Although it is believed that the packing ratio in arteries may not show this percentage because of blood flow and arterial movement, this assumption may not affect dose values much where packing is optimized for effective arterial shunt.

Therefore, more specific dose calculations are left for further study for various packing formations. This will include more comprehensive physiological data, or even voxelized phantom can be used if it guarantees that the resolution of the image is good enough to distinguish the packing of microspheres.

Dose characteristics of ^{142}Pr radioisotope for radiotherapeutic application were analyzed with both Monte Carlo and dose point kernel (DPK) methods. Since ^{142}Pr has never been used for brachytherapy purposes, calculation of dose rate as a function of distance within a centimeter range with various source geometries is needed for clinical application. The source geometries studied in this work are point, wire (solid cylinder), stent (cylindrical shell), disk, and sphere. For a point source, spectrum data obtained from LOGft showed higher dose rates than data from SADDE MOD2. ^{142}Pr stents had lower dose rates than ^{32}P calculated by Prestwich (1996) for short distances around the source surface. This result contradicts that ^{142}Pr has higher maximum beta energy than that of ^{32}P. This may due to different dose calculation algorithms between DPK and MCNP. As an ophthalmic applicator, ^{142}Pr is very similar to that of ^{90}Sr/^{90}Y source currently being used. Spherical geometry was carefully studied as a function of the diameter of the source because this isotope may be useful for future treatment of hepatic tumors and arteriovenous malformation (AVM) by injecting ^{142}Pr microspheres through a catheter. For simple geometries, such as point and sphere dose profiles, were calculated and compared with DPK calculations. Specifically, results obtained by MCNP calculations for microspheres that can be used for AVM treatment was fit to nonlinear analytic function for a distance around the source and compared with the result from DPK calculations. The results agreed well at interested distances from the source of clinical interest. Variation of fitted and calculated values agreed better for larger diameter microspheres than for smaller ones. From the dose fall-off trend, it is concluded that ^{142}Pr could be a good source of beta rays that could replace current sources for certain cases such as radio-embolic treatment of AVM or radiotherapeutic treatment of hepatic tumor. Results between Monte Carlo and DPK for multiple microspheres also remain for further study.

Up to now, backscatter factors for beta particles have varied depending on the experimental setup and detector resolution for calculation, and were generally performed for monoenergetic electron beams, which make direct application of these factors to beta sources difficult. The calculated values in this research can be readily incorporated into dose point kernel (DPK) methods using analytical fit methods. This model can also aid in choosing a source support or mixing materials for beta brachytherapy sources. Backscatter factor calculations were carried out with MCNP-4C for beta sources currently in use (^{32}P and ^{90}Sr/^{90}Y), as well as other sources (^{45}Ca, ^{142}Pr and ^{185}W) with potentially useful as brachytherapy seed. Specifically, the calculations used beta spectra generated by the SADDE MOD2 code. The factors were calculated for point sources on the interface between the water and the surroundings, or between the material supporting the source and contrast agents commonly used imaging purposes in brachytherapy. Due to high-Z material content (iodine, Z=53) in the contrast agent, significant dose backscatter was observed near the water interface. Different cross-section algorithms in the MCNP code (inherent and ITS 3.0) affect the factor calculations. The results generated by the ITS 3.0 algorithm closely matched the EGS4 calculations for ^{32}P. The dependence of backscatter factors on log (Z+1) dependence (Baily 1980) was observed for all the beta sources with a high correlation coefficient, R (> 0.95).

REFERENCES

Andreo P 1991 Monte Carlo techniques in medical radiation physics *Phys. Med. Biol.* **36** 861-920

Asenjo J, Fernandez-Varrea J M and Sanchez-Reyes A 2002 Characterization of a high-dose-rate ^{90}Sr-^{90}Y source for intravascular brachythrapy by using the Monte Carlo code PENELOPE *Phys. Med. Biol.* **47** 697-711

Attix F H 1996 *Introduction to Radiological Physics and Radiation Dosimetry* (New York: John Wiley & Sons, Inc)

Bafandeh H R 1992 Beta scattering and back-scattering from a thin target Ph.D. Dissertation, University of Massachusetts-Lowell

Baily N A 1980 Electron backscattering *Med. Phys.* **7** 514-519

Baro J, Sampau J, Fernandez-Varrea J M and Salvat F 1995 PENELOPE: an algorithm for Monte Carlo simulation and energy loss of electrons and positrons in matter *Nucl. Instrum. Methods B* **100** 31-46

Berger M J 1971 Distribution of absorbed dose around point sources of electrons and beta particles in water and other media MIRD Pamphlet No.7 *J. Nucl. Med.***12**: Suppl. No.5 5-24

Berger M J and Seltzer S M 1968 Electrons and Photon Transport Programs: I. Introductions and Notes on Program DATAPAC 4; II. Notes on Program ETRAN-15 Rep. NBS 9836 and 9837 (Gathersberg: NBS)

Briesmeister J F 2000 MCNP-A general Monte Carlo n-particle transport code 4C LA-13709-M, Los Alamos National Laboratory

Campbell A M, Bailey I H and Burton M A 2000 Analysis of the distribution of intra-arterial microspheres in human liver following hepatic yttrium-90 microsphere therapy *Phys. Med. Biol.* **45** 1023-1033

Campbell A M, Bailey I H and Burton M A 2001 Tumor dosimetry in human liver following hepatic yttrium-90 microsphere therapy *Phys. Med. Biol.* **46** 478-498

Chibani O 2001 New electron backscatter correction factors for accurate skin depth dose calculation from skin contamination by hot particles *Health Phys.* **81** 419-425

Cho S 1997 Voxel-based three dimensional beta dose calculations in heterogeneous media using superposition Ph.D. Dissertation, Texas A&M University, Texas

Cho S, and Reece W D 1999 Monte Carlo calculations of the dose backscatter factor for monoenergetic electrons *Phys. Med. Biol.* **44** 13-26

Cho S, Reece W D and Poston Sr J P 1997 Calculation of the dose distribution in water from ^{71}Ge K-shell x-rays *Phys. Med. Biol.* **42** 1023-1032

Cross W G, Freedman N O and Wong P Y 1992 Beta ray dose distributions from skin contamination *Radiat. Prot. Dosim.* **40** 149-168

Cross W G, Hokkanen J, Järvinen H, Mourtada F, Sipilä P, Soares C G, and Vynckier S 2001 Calculation of beta-ray dose distributions from ophthalmic applicators and comparison with measurements in a model eye *Med. Phys.* **28** 1385-1396

Das I J, Coia L R and Tabata T 1995 Harvesting backscatter electrons for radiation therapy *Int. J. Radiation Oncology Biol. Phys.* **33** 695-703

Durham J S 1992 VARSKIN MOD2 and SADDE MOD2: Computer code for assessing skin dose from skin contamination NUREG/CR-5873 (Washington, D.C.: U.S. NRC)

Fox R A 2002 Intravascular brachytherapy of the coronary arteries *Phys. Med. Biol.* **47** R1-R30

Halbleib J 1988 Structure and Operation of the ITS Code System Monte Carlo Transport of Electrons and Photons (New York: Plenum) 503-22

Hughes H G 1997 Status of electron transport in MCNP^{TM} LA- UR-97-1368, Los Alamos National Laboratory

Jeraj R, Keall P J and Ostwald P M 1999 Comparisons between MCNP, EGS4 and experiment for clinical electron beams *Phys. Med. Biol.* **44** 705-7

Jodrey W S and Tory E M 1985 Computer simulation of close random packing of equal spheres *Phys. Rev. A* **32** 2347-2351

Johns H E and Cunningham J R 1983 *The Physics of Radiology*, 4th ed. (Thomas, Springfield, IL)

Johnson L S and Yanch J C 1993 Calculation of beta dosimetry in radiation synovectomy using Monte Carlo simulation (EGS4) *Med. Phys.* **20** 747-754

Kawrakow I and Rogers D W O 2000 *The EGSnrc Code System: Monte Carlo simulation of electron and photon transport NRCC Report PIRS-701* (Ottawa: National Research Council of Canada)

Klevenhagen S C 1991 Implication of electron backscattering for electron dosimetry *Phys. Med. Biol.* **36** 1013-1018

Knoll G F 2000 *Radiation Detection and Measurement* (New York: John Wiley & Sons, Inc)

Li X A 2001 Dosimetric effect of contrast media for catheter-based intravascular brachytherapy *Med. Phys.* **28** 757-763

Love P A, Lewis D G, Al-Affan I A M and Smith C W 1998 Comparison of EGS4 and MCNP Monte Carlo codes when calculating radiotherapy depth doses *Phys. Med. Biol.* **43** 1351-1357

Mawad M E 2001 Private communication (College of Medicine, Baylor University)

Nagashima H, Okudera H, Muraoka S, Hongo K and Kobayashi S 2000 Strategic embolisation for successful resection of a large cerebral arteriovenous malformation *J. of Clinic. Neuroscience* **7** 86-87

Nath R, Amols H, Coffey C, Duggan D, Jani S, Li Z, Schell M, Soares C, Whiting J, Cole P E, Crocker I and Schwartz R 1999a Intravascular brachytherapy physics: Report of AAPM Radiation Therapy Committee Task Group No. 60 *Med. Phys.* **26** 119-152

Nath R and Yue N 2001 Shielding effect of metallic encapsulations and radiographic contrast agents for catheter-based intravascular brachytherapy *Cardiovasc. Radiat. Med.* **1** 93-103

Nath R, Yue N and Weinberger J 1999b Dose perturbations by high atomic number materials in intravascular brachytherapy *Cardiovasc. Radiat. Med.* **1** 144-153

Nelson W R, Hirayama H and Rogers D W O 1985 The EGS4 code system SLAC-265

Nolan G T and Kavanagh P E 1992 Computer simulation of random packing of hard spheres *Powder Technol.* 149-155

Nunes J N, Prestwich W V and Kwok C S 1993a Experimental determination of ^{32}P dose backscatter factor at and near soft-tissue boundaries *Med. Phys.* **20** 223-231

Nunes J N, Prestwich W V and Kwok C S 1993b An evaluation of the EGS4 and CYLTRAN Monte Carlo codes with regard to boundary beta-ray dosimetry comparison with experimental beta-ray dose backscatter factors *Med. Phys.* **20** 1243-1250

Pandey L N and Rustgi M L 1989 Monte Carlo study of backscattering of β rays from various monoatomic slabs *J. Appl. Phys.* **66** 5-9

Prestwich W V 1996 Analytic representation of the dose from a ^{32}P-coated stent *Med. Phys.* **23** 9-13

Prestwich W V, Kennett T J and Kus F W 1995 The dose distribution produced by a ^{32}P-coated stent *Med. Phys.* **22** 313-320

Reece W D, Miller S D and Durham J S 1989 SADDE (Scaled Absorbed Dose Distribution Evaluator) – A code to generate input for VARSKIN NUREG/CR-5276 (Nuclear Regulatory Commission)

Sayeg J A and Gregory R C 1991 A new method for characterizing beta-ray ophthalmic applicator sources *Med. Phys.* **18** 453-61

Schaart D R, Jansen J T M, Zoetelief J and de Leege P F A 2002 A comparison of MCNP4C electron transport with ITS 3.0 and experiment at incident energies between 100 keV and 20 MeV: influence of voxel size, substeps and energy indexing algorithm *Phys. Med. Biol.* **47** 1459-1484

Seltzer S 2001 Private communication (National Institute of Standards and Technology)

Serruys P W and Carlier S G 2000 Brachytherapy in the Journal: European cardiologists have their own forum and should use it! *European Heart Journal* **21** 1994-1996

Sharma K K and Singh M 1979 Variation of beta-ray backscattering with target thickness *J. Appl. Phys.* **50** 1529-1532

Sharma K K and Singh M 1980 Z dependence of thick-target β-ray scattering *J. Appl. Phys.* **51** 2239-2241

Siegel J A and Stabin M G 1994 Absorbed fractions for electrons and beta particles in spheres of various sizes *J. Nuc. Medicine* **35** 152-156

Siams Ltd Website for S3D® manual http://siams.com (Accessed on September 2002)

Simpkin D J and Mackie T R 1989 EGS4 Monte Carlo determination of the beta dose kernel in water *Med. Phys.* **17** 179-186

Soares C G, Vynckier S Jarvinen, Cross W G, Sipila P, Fluhs D, Schaeken B, Mourtada F A, Bass G A and Williams T T 2001 Dosimetry of beta-ray ophthalmic applicators: comparison of different measurement methods *Med. Phys.* **28** 1373-1384

Torquato S, Truskett T M, Debenedetti P G 2000 Is random close packing well defined? *Phys. Rev.* **84** 2064-2067

Wang R and Li X A 1999 Monte Carlo dose calculations of beta-emitting sources for intravascular brachytherapy: a comparison between EGS4, EGSnrc and MCNP *Med. Phys.* **28** 134-141

Yeung D, Chen N, Ferguson R D G and Lee L I 1996 Three dimensional reconstruction of arteriovenous malformations from multiple stereotatic angiograms *Med. Phys.* **23** 1797-1804

Zavgorodni S F 1996 A model for dose estimation in therapy of liver with intraarterial micospheres *Phys. Med. Biol.* **41** 2463-2480

VITA

Sung-Woo Lee was born in Seoul, Korea as the second son of Mrs. Kyu Soon Kim and Dr. Chang Koo Lee. He graduated from the Department of Nuclear Engineering at Hanyang University (B.S.), Seoul, Korea in 1993. He earned his M.S. degree in nuclear engineering from the same university in 1995. He worked as a nuclear engineer in Korea Power Engineering Company, Inc. (KOPEC) 1996. Upon his admission to Texas A&M University in 1996, he relocated to the United States to continue his M.S. degree in health physics at Department of Nuclear Engineering, and earned his degree in 1999. He earned his Ph.D. in nuclear engineering from Texas A&M in May 2003.

He can be reached at the Department of Nuclear Engineering, Texas A&M University, College Station, Texas 77843-3133 through Dr. W. Daniel Reece.